



Evolution of Developmental Control Mechanisms

The Retinoblastoma pathway regulates stem cell proliferation in freshwater planarians

Shu Jun Zhu^{a,c}, Bret J. Pearson^{a,b,c,*}^a The Hospital for Sick Children, Program in Developmental and Stem Cell Biology, 101 College St. MaRS East Rm 11-704, Toronto, ON, Canada M5G1L7^b University of Toronto, Department of Molecular Genetics, ON, Canada M5S1A1^c Ontario Institute for Cancer Research, Toronto, ON, Canada M5G1L7

ARTICLE INFO

Article history:

Received 9 August 2012

Received in revised form

16 October 2012

Accepted 22 October 2012

Available online 1 November 2012

Keywords:

Retinoblastoma

Tumor suppressor

Adult stem cells

Lophotrochozoan

Planarians

Schmidtea mediterranea

ABSTRACT

Freshwater planarians are flatworms of the Lophotrochozoan superphylum and are well known for their regenerative abilities, which rely on a large population of pluripotent adult stem cells. However, the mechanisms by which planarians maintain a precise population of adult stem cells while balancing proliferation and cell death, remain to be elucidated. Here we have identified, characterized, and functionally tested the core Retinoblastoma (Rb) pathway components in planarian adult stem cell biology. The Rb pathway is an ancient and conserved mechanism of proliferation control from plants to animals and is composed of three core components: an Rb protein, and a transcription factor heterodimer of E2F and DP proteins. Although the planarian genome contains all components of the Rb pathway, we found that they have undergone gene loss from the ancestral state, similar to other species in their phylum. The single Rb homolog (*Smed-Rb*) was highly expressed in planarian stem cells and was required for stem cell maintenance, similar to the Rb-homologs *p107* and *p130* in vertebrates. We show that planarians and their phylum have undergone the most severe reduction in E2F genes observed thus far, and the single remaining E2F was predicted to be a repressive-type E2F (*Smed-E2F4-1*). Knockdown of either *Smed-E2F4-1* or its dimerization partner *Dp* (*Smed-Dp*) by RNAi resulted in temporary hyper-proliferation. Finally, we showed that known Rb-interacting genes in other systems, *histone deacetylase 1* and *cyclinD* (*Smed-HDAC1*; *Smed-cycD*), were similar to Rb in expression and phenotypes when knocked down by RNAi, suggesting that these established interactions with Rb may also be conserved in planarians. Together, these results showed that planarians use the conserved components of the Rb tumor suppressor pathway to control proliferation and cell survival.

© 2012 Elsevier Inc. All rights reserved.

Introduction

The ability to regulate cell division is a fundamental property of all animals, and the Retinoblastoma pathway (Rb) is an ancient and critical component of this process. Originally discovered in humans, it is now clear that the Rb tumor suppressor pathway existed prior to multicellularity and prior to the split between animals and plants (Messenguy et al., 2000; Van den Heuvel and Dyson, 2008; Wildwater et al., 2005). Mechanistically, there are three proteins at the core of the Rb pathway: an RB protein, which binds the transcription factor heterodimer complex composed of E2F and DP proteins. E2F proteins are generally either transcriptional activators or repressors, which compete for DNA binding at genetic loci required for cell cycle progression (Attwooll et al.,

2004; Crosby and Almasan, 2004). RB proteins typically disrupt activating-E2F complexes and modify repressive E2F function, thus altering the activator/repressor balance to fine-tune cell cycle entry at the G₁/S transition (Burkhart and Sage, 2008; Classon and Harlow, 2002; Soleimani et al., 2012). RB binding to E2Fs, in turn, is negatively regulated through phosphorylation of RB by CDK/cyclin complexes (Dora et al., 1999). Cancer can result in humans, for example, when Rb is mutated and activating-E2F complexes drive ectopic cell cycle entry (Attwooll et al., 2004).

A large body of work has shown that the genes in the Rb pathway have a complex evolutionary history as well as diverse functions. For example, mammals have 3 RB homologs which are partially redundant, can cross regulate, and have specific preferences for which types of E2Fs they bind (van den Heuvel and Dyson, 2008). Furthermore, mammals have 8 E2F loci (E2F1-8): E2Fs 1–3 are primarily activators, E2Fs 4–5 are primarily repressors, and E2Fs 6–8 have lesser-known functions (van den Heuvel and Dyson, 2008). Finally, mammals have 3 DP homologs. In total, the high genetic redundancy in combination with the tissue or

* Corresponding author at: The Hospital for Sick Children, Program in Developmental and Stem Cell Biology, 101 College St., MaRS East Rm 11-704, Toronto, ON, Canada M5G1L7. Fax: +1 416 813 8456.

E-mail address: bret.pearson@sickkids.ca (B.J. Pearson).

developmental stage of the animal, has led to the discoveries that the Rb pathway functions in many diverse processes such as cell cycle control, DNA segregation, apoptosis, cellular senescence, and differentiation (Burkhart and Sage, 2008; Chicas et al., 2010; Classon and Harlow, 2002; Crosby and Almasan, 2004; Moon et al., 2008; Schwartzman et al., 2011; Wildwater et al., 2005). This complexity has made it difficult to ascribe functions to any single gene, and therefore, model organisms that have a simplified genetic context for the Rb pathway can shed light on both its evolution and function.

The Rb pathway has also undergone considerable evolution in different animal phyla. *Drosophila* has 2 RBs, 2 E2Fs (1 activator, 1 repressor), and 1 DP (Betz et al., 1998). *C. elegans* has 1 RB, 3 E2Fs (only one of which has a mutant phenotype), and 1 DP. Low genetic redundancy, typical of invertebrates, has allowed the elegant genetic dissection of Rb pathway functions (van den Heuvel and Dyson, 2008). These model systems have shown that RB can transcriptionally repress target loci through the recruitment of repressive chromatin remodelers such as histone deacetylase 1 (HDAC1) or complexes such as DREAM or NuRD (Cui et al., 2006; Dufourcq et al., 2002; Ferreira et al., 1998; Lu and Horvitz, 1998; Rossi et al., 1998). Interestingly, the *C. elegans* Rb pathway functions primarily to antagonize RAS-signalling in vulval differentiation, and has minimal roles in cell division control (Lu and Horvitz, 1998). In *Drosophila*, the Rb pathway controls cell cycle entry during development by balancing activator and repressor E2F function (Dimova et al., 2003; Frolov et al., 2001; Stevaux et al., 2002). Interestingly, mutating both fly E2Fs leads to relatively normal cell division and development until larval stages (Frolov et al., 2001). In summary, work from flies and *C. elegans* suggests that the Rb pathway does not function in tumor suppression per se, even though it has roles in aspects of cell division, cell death, and differentiation.

Despite the large body of work in vertebrates, flies, and *C. elegans*, it has been difficult to test Rb pathway function in adult animals or adult stem cells (ASCs), and there is virtually no functional data from animals outside of these clades. Adult freshwater planarians (flatworms) are ideal organisms to test the functional evolution of the Rb pathway because they have a large population of adult stem cells (ASCs), the ability to modulate cell division of their ASCs on a global scale, and their phylogenetic position in the Lophotrochozoan superphylum facilitates evolutionary comparisons. The asexual planarian, *Schmidtea mediterranea* (*S. med.*), is a constitutive adult, with no known senescence or aging, and can regenerate from virtually any injury (Elliott and Sánchez Alvarado, 2012; Newmark and Sánchez Alvarado, 2002; Reddien et al., 2005a; Reddien and Sánchez Alvarado, 2004). Both their longevity and regenerative abilities depend on a large population of pluripotent ASCs. Planarians have already been shown to have conserved genetic mechanisms that control ASC proliferation, which can be drastically modulated in a given context (Wenemoser et al., 2012). For example, when planarians undergo injury, stem cells temporarily hyper-proliferate to replace missing structures through use of TOR signalling (Tu et al., 2012). In contrast, when planarians are starved, they decrease cell division and increase apoptosis (Kadosh and Struhl, 1998). Finally, non-injured planarians use the p53, PTEN, and EGFR pathways to limit proliferation in their stem cell lineages (Fraguas et al., 2011; Oviedo, 2008; Pearson and Sanchez Alvarado, 2010). With a completely sequenced genome, low genetic redundancy, and the ability to test gene function in adult animals by RNAi, planarians are a powerful system to understand the mechanisms of proliferation control in ASCs.

In this study, we tested the function of the Rb pathway in proliferation control in planarians. We find that planarians (and their phylum) have undergone the most severe reduction in the Rb pathway described to date for any animal clade. Despite this,

each component of the canonical Rb pathway is involved in regulating proliferation of adult stem cells. We find that Lophotrochozoans as a superphylum have lost an E2F7/8 homolog while the flatworms have additionally lost an activating E2F1/2/3 homolog, and have only retained a single, repressive E2F4/5-like molecule (*Smed-E2F4-1*). When *Smed-E2F4-1* was knocked down by RNAi, animals showed briefly increased cell cycle entry, suggesting that this gene indeed functions as a repressor of cell cycle genes. Similar results were obtained for E2F's binding partner, *Smed-Dp*. Our analysis of RB homologs showed that planarians have a single *Rb* (*Smed-Rb*) that was more similar to vertebrate RB-homologs, p107 and p130. This supported previous data that p107/p130 represent the ancestral protein state of the Rb family and that RB itself arose specifically at the base of the Deuterostomes via gene duplication (Cao et al., 2010; Wirt and Sage, 2010). When *Smed-Rb* was knocked down by RNAi, stem cell self-renewal was abolished. Finally, we investigated the roles of planarian orthologs of upstream (*cyclins D* and *E*) and downstream (*HDAC1*) regulators of RB in other systems. We found that both *HDAC1* and *cyclinD* RNAi animals showed phenotypes consistent with function in the Rb pathway and stem cell self-renewal. Interestingly, planarians and other flatworms appeared to have lost a *cyclinE* ortholog. From these data, we concluded that planarians have retained the ancestral function of the Rb pathway in proliferation control, however, they have done so without retaining *cyclinE* or an activating E2F-like molecule. From this, we hypothesize that planarians have evolved to transcribe cell cycle entry genes through the negative regulation of a repressive E2F complex.

Materials and methods

Phylogenetics and cloning

Rb pathway gene homologs were found in the sequenced and assembled planarian genome as previously described (Pearson and Sanchez Alvarado, 2010; Robb et al., 2008; Sánchez Alvarado et al., 2002, 2003). Primers were designed and full length genes were cloned by 3' RACE. Cloned ORFs were then converted to predicted proteins and subjected to Bayesian phylogenetic analyses. Protein sequences used in phylogenies were obtained from the NCBI Entrez protein database or directly from the genome sequencing projects of included organisms. The program Geneious (www.geneious.com) was used with the MUSCLE alignment plugin, and two tree building plugins for Geneious were used as independent analyses. Both Maximum Likelihood and Bayesian analyses were performed with the following settings: Maximum Likelihood – 10,000 bootstrap replicates, WAG substitution model, estimated distances; Bayesian – 1million replicates, WAG substitution model, 4 heated chains, 25% burnin, subsample frequency of 1000. Consensus tree images were saved through Geneious, which were then manipulated in Adobe Photoshop. Alignments are provided as supplemental files A1–A2. *Smed-Rb*, *Smed-E2F4-1*, *Smed-HDAC1*, *Smed-cyclinD*, and *Smed-Dp* sequences were deposited in GenBank as accession numbers: JX967264–JX967268, respectively. Transcripts listed in Tables S2–S3 can be found in the transcriptome database associated with the NCBI GEO project: GSE37910.

Animal husbandry and RNAi

Asexual *S. mediterranea* CIW4 strain were reared as previously described (Sánchez Alvarado et al., 2002). RNAi experiments were performed using previously described expression constructs and HT115 bacteria (Newmark et al., 2003). Briefly, bacteria were grown to an O.D.600 of 0.8 and induced with

1 mM IPTG for 2 h. Bacteria were pelleted and mixed with liver paste at a ratio of 500 μ l of liver per 100 ml of original culture volume. Bacterial pellets were thoroughly mixed into the liver paste and frozen as aliquots. The negative control, “control(RNAi)”, was the *unc22* sequence from *C. elegans* as previously described (Reddien et al., 2005a). All RNAi food was fed to 7-day starved experimental worms every 3rd day for 3 total feedings for *Rb*, *HDAC1*, and *cyclinD*, and 4 feedings for *Dp* and *E2F4-1*. All time points are given post-RNAi where day 0 was the day of the third feed for all conditions, and day 3 is the 4th feed for *Dp* and *E2F4-1* and their respective controls. Amputations were performed 7 days after the final feeding unless noted otherwise. All animals used for immunostaining were 2–3 mm in length and size-matched between experimental and control worms.

Deep sequencing

RNA deep sequencing of the planarian stem cell, stem cell progeny, and differentiated tissue compartments was recently performed (Labbe et al., 2012). Briefly, we used flow cytometry to obtain a cell population highly enriched in stem cells as previously described (Hayashi et al., 2006). Approximately 1.3 million stem cells were isolated on a Becton–Dickinson FACSaria over 7 independent sorts. Two samples of RNA were subjected to next generation sequencing for comparison of differential expression enrichment in the stem cell compartment: (1) sorted stem cells; and (2) irradiated worms 7 days post-irradiation which have no stem cells or stem cell progeny. Here, we specifically used the expression data to the full-length transcripts for: *Rb*, *E2F4-1*, *Dp*, *cyclinD*, and *HDAC1* (Table S1); all planarian cyclins (Table S2); and all planarian CDKs (Table S3).

Immunolabeling, TUNEL, and in situ hybridization (ISH)

ISH, double-fluorescent ISH (dFISH), and immunostaining were performed as previously described (Pearson et al., 2009). Colorimetric ISH and fluorescent phospho-histone H3 (H3P) stains were imaged on a Leica M165 fluorescent dissecting microscope. The rabbit monoclonal antibody to H3ser10p from Millipore (04–817) was used for all cell division assays. TUNEL was performed as previously described (Pellettieri and Alvarado, 2007). Rabbit anti-PIWI-1 (gift of Dr. Peter Reddien (Wagner et al., 2011)) was used at 1:1500. TUNEL/PIWI-1 double stains were imaged on a Leica DMIRE2 inverted fluorescence microscope with a Hamamatsu Back-Thinned EM-CCD camera and spinning disc confocal scan head. H3ser10p and TUNEL were quantified using freely available ImageJ software (<http://rsb.info.nih.gov/ij/>). Significance was determined by a Student's *t*-test. All experiments were, at minimum, triplicated and at least 10 worms were used per stain and per time point. All time points are given as post-RNAi where day 0 is the day of the final RNAi feeding.

Results

Platyhelminthes have single *Rb* and *Dp* homologs, and have undergone an evolutionary reduction in E2F genes

Based on previous studies, it is clear that the ancestral state of RB was closer in sequence and function to vertebrate p107/p130 proteins (Cao et al., 2010; Wirt and Sage, 2010). However, no study has examined sequences from the Lophotrochozoa, where several genome sequencing projects have been recently performed. Examining sequences in the Lophotrochozoa is critical because it is formally possible that RB and p107/p130 orthologs

exist in this superphylum and were lost in the Ecdysozoa. Thus, the *S. mediterranea* genome and transcriptome were extensively searched (Labbe et al., 2012; Robb et al., 2008; Sánchez Alvarado et al., 2003), and similar to other non-chordates, a single homolog of *Rb* was found (*Smed-Rb*; *Rb* for the rest of this article). The full-length *Rb* was cloned and phylogenetic analyses were performed, which gave several interesting results (Fig. 1A). First, by using genomic sequences of four Lophotrochozoans, it was clear that the ancestral state of *Rb* homologs was a single p107/p130-like molecule. In addition, the two fly homologs of RB are a *Drosophila*-specific duplication as three other insects and a crustacean do not have more than a single *Rb* homolog. Finally, in the Deuterostome lineage, RB and p107/p130 split from each other very early because two other non-vertebrate chordates have clear RB and p107/p130 orthologs. Together, phylogenetic analysis supported previous hypotheses that invertebrate RB homologs are structurally more similar to p107/p130 and also represent the ancestral sequence of the molecule (Cao et al., 2010; Wirt and Sage, 2010). However, despite the fact the SMED-RB had approximately 10% more amino acid identity to p107/p130, we were unable to identify domains that are present in vertebrate p107 and p130 and absent in vertebrate RB. These include an N-terminal CDK-inhibitory domain, and a cyclin-binding domain inside a split *Rb*-B pocket domain (Cao et al., 2010; Wirt and Sage, 2010). These domain rearrangements are thus likely to be vertebrate-specific alterations because fly and *C. elegans* *Rb* homologs also lack these features.

A search for a DP-like protein in the planarian genome uncovered the presence of a single *Dp* gene, which has been the case for all non-vertebrate organisms examined (*Smed-Dp*; *Dp* for the rest of this manuscript). The planarian E2F gene complement was more complex and interesting. A search of the planarian transcriptome returned a single E2F. However, a search of the planarian genome detected 4 other regions of E2F homology. Three of these other E2Fs appeared to be recent duplicates based on high nucleotide identity (i.e., 87–91% nucleotide identity) with the intact E2F transcript, which explained why transcript assembly could not assemble multiple E2F genes (Labbe et al., 2012). In addition, two of the four genes had stop codons in key domains in their predicted amino acid sequences, which suggested that these may represent pseudogenes (we have named these sequences *Smed-pE2Fa-d*). We were unsuccessful in cloning any of these paralogous or pseudo-E2Fs, suggesting that they are either not transcribed in asexual planarians or are degraded quickly. Finally, it is noteworthy that even if the pseudo-E2Fs were transcribed, RNAi is predicted to knock them down due to the near identical nucleotide sequences.

The evolution of the E2F family has never been completely understood, primarily because Lophotrochozoan genomes have not been accessible until recently. To understand the evolution of this gene family as a whole and in the flatworms, phylogenetic analysis was performed using 6 Lophotrochozoans, which included 4 flatworm species (Fig. 1B). This complement of species yielded several interesting results. First, the ancestral E2F gene complement for all animals was a single member of each: E2F1/2/3/6, E2F4/5, and E2F7/8. This conclusion was reached because we observed that *C. elegans*, the insect *Nasonia vitripennis*, and the cnidarian *Nematostella vectensis*, have representative molecules of all three E2F types (as do vertebrates). Second, it is clear that E2Fs 1, 2, 3, and 6 arose specifically in the vertebrates through duplication of a single gene. Third, Lophotrochozoans appear to have lost an E2F7/8 homolog, which could not be found in members of molluscs, annelids, or platyhelminthes. In terms of the evolution of E2F genes in the Platyhelminthes, we observed that an activating E2F1/2/3-like molecule was additionally lost in this phylum. Finally, the observed *S. mediterranea* pseudo-E2F

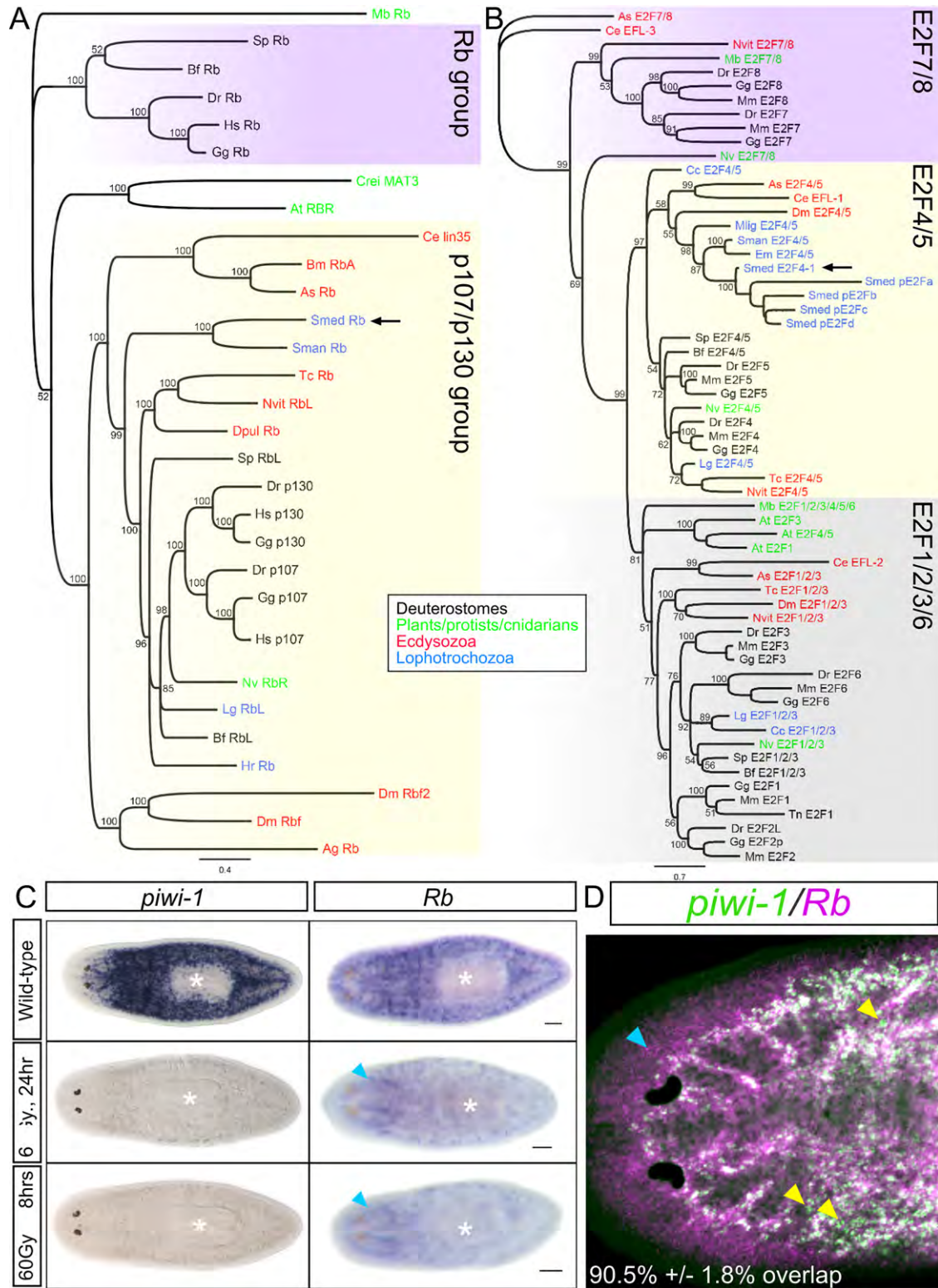


Fig. 1. Evolution of the Rb pathway and analysis of *Smed-Rb* expression. (A) A Bayesian phylogeny of RB homologs. The *S. mediterranea* homolog used in this study clearly groups with p107/p130. Non-vertebrate chordates have clear RB orthologs, and thus the split of RB from p107/p130 occurred at the base of the Deuterostomes. Only *Drosophila melanogaster* was found to have more than a single RB homolog in the Protostomes used. (B) A Bayesian phylogeny of the E2F family. Nematodes, insects, and vertebrates have representative members of each E2F sub-type. No E2F7/8 homolog could be found in the Lophotrochozoans, and no activating E2F1/2/3/6 could be found in the flatworms. The *S. mediterranea* homolog used in this study clearly groups with E2F4/5. (C) WISH for the stem cell marker *piwi-1*, and *Rb*. *Rb* showed a stem cell specific pattern, which was ablated by 24 h post-irradiation, similar to *piwi-1*. *Rb* expression in the brain remains following irradiation (blue arrowheads). White asterisks mark the pharynx. (D) Double FISH for *piwi-1* and *Rb*. White cells indicate double-positive cells which make up 90.5% ± 1.8% of the *piwi-1*⁺ cell population. Examples of the remaining 9.5% of *piwi-1* single-positive cells are marked by yellow arrowheads. The blue arrowheads mark the *Rb* brain-specific expression. For phylogenies: only bootstrap values over 50 or key nodes are shown; arrows indicate the *S. mediterranea* homolog used in this study. Species used: *Mb*=*Monosiga brevicollis*; *Nv*=*Nematostella vectensis*; *Crei*=*Chlamydomonas reinhardtii*; *At*=*Arabidopsis thaliana*; *Ce*=*C. elegans*; *As*=*Ascaris suum*; *Bm*=*Brugia malayi*; *Dm*=*Drosophila melanogaster*; *Tc*=*Tribolium castaneum*; *Ag*=*Anopheles gambiae*; *Nvit*=*Nasonia vitripennis*; *Dpul*=*Daphnia pulex*; *Lg*=*Lottia gigantea*; *Hr*=*Helobdella robusta*; *Cc*=*Capitella capitata*; *Mlig*=*Macrostomum ligano*; *Sman*=*Schistosoma mansoni*; *Em*=*Echinococcus multilocularis*; *Smed*=*Schmidtea mediterranea*; *Sp*=*Strongylocentrotus purpuratus*; *Bf*=*Branchiostoma floridae*; *Dr*=*Danio rerio*; *Tn*=*Tetraodon nigroviridis*; *Gg*=*Gallus gallus*; *Mm*=*Mus musculus*; *Hs*=*Homo sapiens*.

duplications do not exist in other sequenced flatworms, nor do these molecules represent other E2F types (i.e., all are predicted to be E2F4/5 homologs). Whether these duplicates are specific to *S. mediterranea* or are representative of other free-living flatworms of the triclads or polyclads remains to be determined upon further genome sequencing. In conclusion, while *Rb* and *Dp* genes are represented by the ancestral single homolog in planarians, the E2F family had an interesting evolutionary history and has been reduced from 3 ancestral genes to 1 of the repressive-type E2F4/5 in flatworms. Thus, we have named this gene *Smed-E2F4-1* (*E2F4-1* for the rest of this study).

Planarian Rb, E2F4-1, and Dp are primarily expressed in planarian stem cells

To first determine where *Rb*, *Dp*, and *E2F4-1* were expressed, we performed whole mount in situ hybridization (WISH). While we could not obtain specific expression patterns for *Dp* and *E2F4-1* (Fig. S1), the resulting pattern for *Rb* was similar to that observed for the known pan-stem cell marker *Smed-piwi-1* (Reddien et al., 2005b), with the additional pattern of expression in the brain (Fig. 1C, blue arrow heads). If *Smed-Rb* is expressed in planarian stem cells, its stem cell-like expression pattern should disappear within 24 h following a lethal dose of irradiation, similar to *Smed-piwi-1* (Eisenhoffer et al., 2008). As expected, when planarians were gamma-irradiated with 60 Gy., *Rb* stem cell expression was abolished by 24 h while the brain pattern remained due to planarian neurons being radiation-insensitive (Fig. 1C). Further reduction in *Rb* expression was not seen over the subsequent 24 h. Together, this suggested that *Rb* is expressed primarily in the stem cell compartment.

We further examined whether *Rb*, *E2F4-1*, or *Dp* were expressed in stem cells by two other methods: RNA deep sequencing of stem cells (Labbe et al., 2012), and double fluorescent WISH (dFISH; *Rb* only). Comparing stem cell expression to the rest of the tissues in the worm, we found 9.9-fold differential expression in the stem cell compartment for *Rb* and 3.1 and 3.8 fold differential expression for *E2F4-1* and *Dp*, respectively (Table S1). Finally, dFISH was performed with *Rb* and *Smed-piwi-1*. We found that 90.5% ($\pm 1.8\%$; 333/368 total cells, $n=5$) of *piwi-1*⁺ cells also express *Rb*

(Fig. 1D). Taken together, our data showed that the core components of the *Rb* pathway were highly expressed in the stem cell compartment.

Planarian Rb, E2F4-1, and Dp are all required for stem cell function during normal tissue homeostasis and during regeneration

To investigate the effects of *Rb*, *E2F4-1*, or *Dp* on stem cell function, we knocked down expression of these genes using RNAi, then observed animals for defects in tissue homeostasis in uninjured animals. Stem cell loss in planarians by irradiation or RNAi against stem cell-specific genes results in characteristic stem cell deficient phenotypes including head regression, dorsal lesions, and ventral curling (Pearson and Sanchez Alvarado, 2010; Reddien et al., 2005a). Administration of RNAi against either *Rb*, *E2F4-1*, or *Dp* led to the development of these stem cell deficient phenotypes in 100% of the worms by 14–16 days post-RNAi (Fig. 2A). It should be noted that a single lesion, directly dorsal to the pharynx, was observed in *E2F4-1* and *Dp* RNAi animals, while multiple dorsal lesions were observed in *Rb*(RNAi) animals. Although dorsal lesioning is commonly observed in the course of stem cell deficient phenotypes, it is not a required step in the progression, and it is largely unknown why it is observed. Together, however, these phenotypes indicated that stem cell output during tissue homeostasis requires the activity of the *Rb* pathway.

The ability of planarians to regenerate is another assay to examine proper stem cell functions in response to injury, which involves temporary hyper-proliferation to make the missing tissue, and production of the correct differentiated progeny. RNAi-treated worms were assayed using the same feeding schedule as the homeostasis experiments combined with amputation of the worms into 3 fragments 7 days after the final feedings (the very beginning of any observable phenotypes). In all 3 RNAi treatments, regeneration ability was markedly reduced at 3 days of regeneration and severely compromised by 7 days of regeneration (Fig. 2B). This suggested that perturbation of the *Rb* pathway impairs stem cell function, concordant with observations during tissue homeostasis. Despite clear stem cell defective phenotypes for both intact homeostasis and regeneration, these

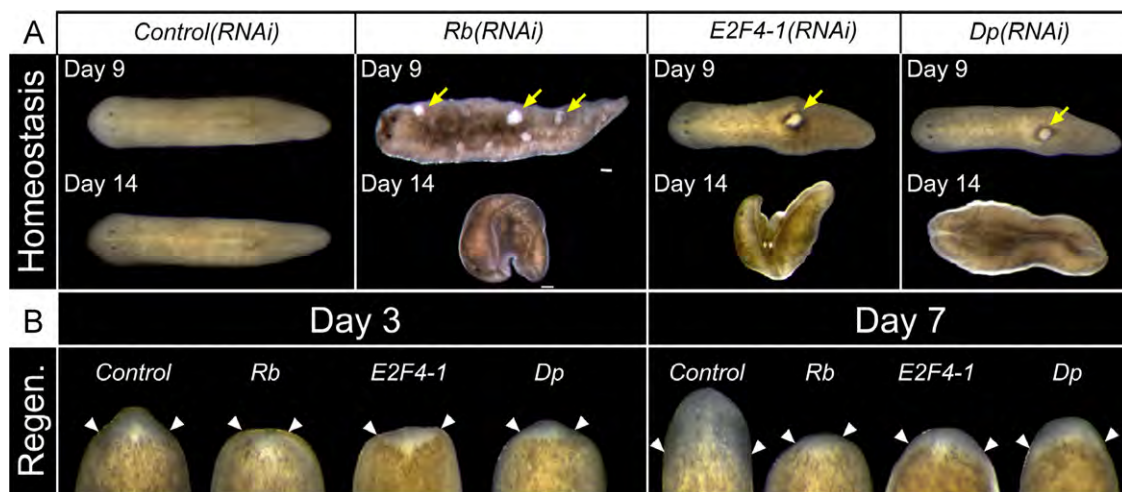


Fig. 2. Live images representing the RNAi phenotypes from knockdown of *Rb*, *E2F4-1* and *Dp* genes. (A) Intact phenotypes. *Rb* typically presented multiple dorsal lesions approximately 9 days following RNAi feeding (yellow arrows). *E2F4-1* and *Dp* showed a single dorsal lesion directly over the pharynx. Despite this, all RNAi treatments ultimately resulted in a stereotypical stem cell defective phenotype of ventral curling by 14 days post RNAi. (B) Time course of head regeneration. Each image shows a tail regenerating a new head at either day 3 or 7 post amputation. White arrowheads mark the edges of the amputation, and any newly regenerated tissue is unpigmented. *Rb*(RNAi) animals showed virtually no regeneration by day 7. *E2F4-1* and *Dp* RNAi animals showed slightly more regeneration than *Rb*, yet were deficient for regenerative ability. These results demonstrated a requirement for the *Rb* pathway in both tissue homeostasis and regeneration.

gross phenotypes do not predict a specific molecular mechanism. Therefore, we next measured proliferation, survival, and differentiation following Rb pathway knockdown.

The Rb pathway regulates stem cell division in planarians

Because the core Rb pathway is well established in other model systems to have key roles in cell division, we first examined how numbers of dividing cells may be changing during the time course of the Rb, *E2F4-1*, or *Dp* RNAi phenotypes. To achieve this, we measured the number of cells undergoing the G2/M transition of the cell cycle using the antibody to Histone-H3 phosphorylated on serine 10 (H3P). We quantified the staining every 3 days for 15 days following RNAi, where day 0 in our time course is the day of the third RNAi feeding. When knocked down, *Rb(RNAi)* animals showed a slight, yet significant increase in cell proliferation at day 0 compared to controls, while days 3 and 6 showed no difference with controls. After day 6, however, *Rb(RNAi)* animals showed significant hypo-proliferation, which suggested that Rb is either required for mitotic progression, stem cell self-renewal, or for stem cell survival.

Due to the sequence similarity of *E2F4-1* to the repressive E2Fs 4 and 5, we predicted that SMED-E2F4-1 may function as a repressor. If the function of E2F in controlling cell cycle genes has been conserved in planarians, then knockdown of a repressive E2F may show de-repression of cell cycle genes and increased cell cycle entry. In addition, because planarians only have a single *Dp* gene, we predicted that all E2F function requires DP, and both should have closely matched RNAi phenotypes. When we knocked down either *E2F4-1* or *Dp* by RNAi, significant increases in cell division were observed for both conditions during the first 3–6 days following RNAi (Fig. 3). However, similar to *Rb(RNAi)* animals, *E2F4-1* and *Dp* RNAi animals ultimately resulted in loss of proliferation. In total, our data showed that Rb pathway components are required for proper proliferation control and stem cell function in planarians. We next tested the effects of losing *Rb*, *E2F4-1* or *Dp* on the maintenance of the stem cell population and the differentiation of stem cell progeny.

Rb, *E2F4-1*, and *Dp* are ultimately required for stem cell maintenance

The gross disruption of homeostasis and regeneration suggested that the Rb pathway is necessary for stem cell output in

planarians (Fig. 2), however, the specific defects in lineage production can happen at multiple levels in the lineage hierarchy while yielding the same morphological phenotypes (Reddien et al., 2005b). Planarians offer significant advantages to visualize the entire stem cell population and stem cell progeny in whole animals during the time course of phenotypic progression. It has been shown that a large number of “early progeny” from planarian stem cells become post-mitotic and express the marker *Smed-prog-1* within 24 h of their birth (formerly *Smed-NB21.11e*) and then transition to a “late progeny” fate within the next 24–48 h (Eisenhoffer et al., 2008). Combined with the stem cell marker *piwi-1*, we can examine the population dynamics of these three cell types, which can then provide mechanistic insight as to how lineage development is affected. For example, if we observe a decrease in stem cells and a concurrent increase in stem cell progeny, then we would interpret this as premature differentiation of the stem cell population. On the other hand, if all three cell populations decrease with similar kinetics, this would be indicative of a stem cell defect in the processes of cell division, self-renewal, or cell survival. Analyses of the stem cells and their progeny were performed for 15 days following RNAi for each gene, and a steady decrease in both stem cells and their early progeny was observed (Fig. 4). Furthermore, the late progeny marker, *AGAT1*, followed a similar timecourse of loss (Figs. S2–S3) (Eisenhoffer et al., 2008). These data suggested that the Rb pathway is not necessary for the differentiation process, and instead, the stem cell population is specifically affected, consistent with our results for proliferation. Thus, the Rb pathway is either necessary for stem cell division/self-renewal or cell survival, which was tested next.

Planarian Rb is required for stem cell self-renewal and somatic cell survival

Roles of vertebrate p107 and p130 in promoting cell survival and differentiation are well known (Crosby and Almasan, 2004; Jiang et al., 2010; Manning and Dyson, 2011; van den Heuvel and Dyson, 2008). While we observed temporary stem cell hyperproliferation in both *E2F4-1* and *Dp* RNAi-treated worms, these knockdowns as well as *Rb(RNAi)* ultimately resulted in a loss of stem cells. Because SMED-RB is more closely related in sequence to p107/p130, we hypothesized that the loss of stem cells in

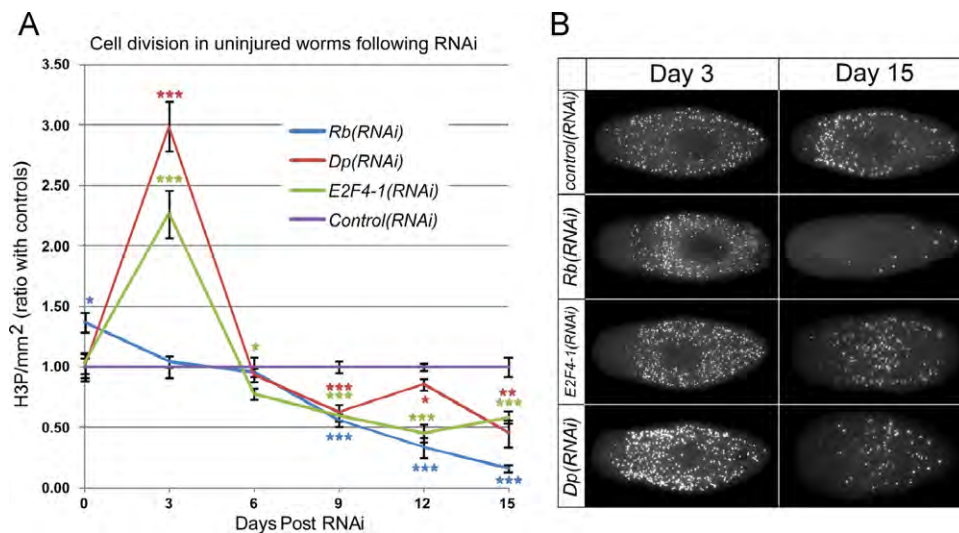


Fig. 3. Cell division (anti-H3P) during the course of *Rb*, *Dp*, or *E2F4-1* RNAi phenotypes. (A) Each RNAi treatment was normalized to control worms and plotted above. At day 3 post-RNAi, *E2F4-1* and *Dp* RNAi animals showed significant increases in cell division, while *Rb(RNAi)* animals showed mostly hypo-proliferation (Student's *t*-test, error bars are standard error). (B) Representative stains for both the hyper- (day 3) and hypo- (day 15) proliferation phases are shown to the right. Images were taken from the dorsal side with anterior to the left. Significance indicators: * = $p < 0.05$; ** = $p < 0.01$; *** = $p < 0.001$.

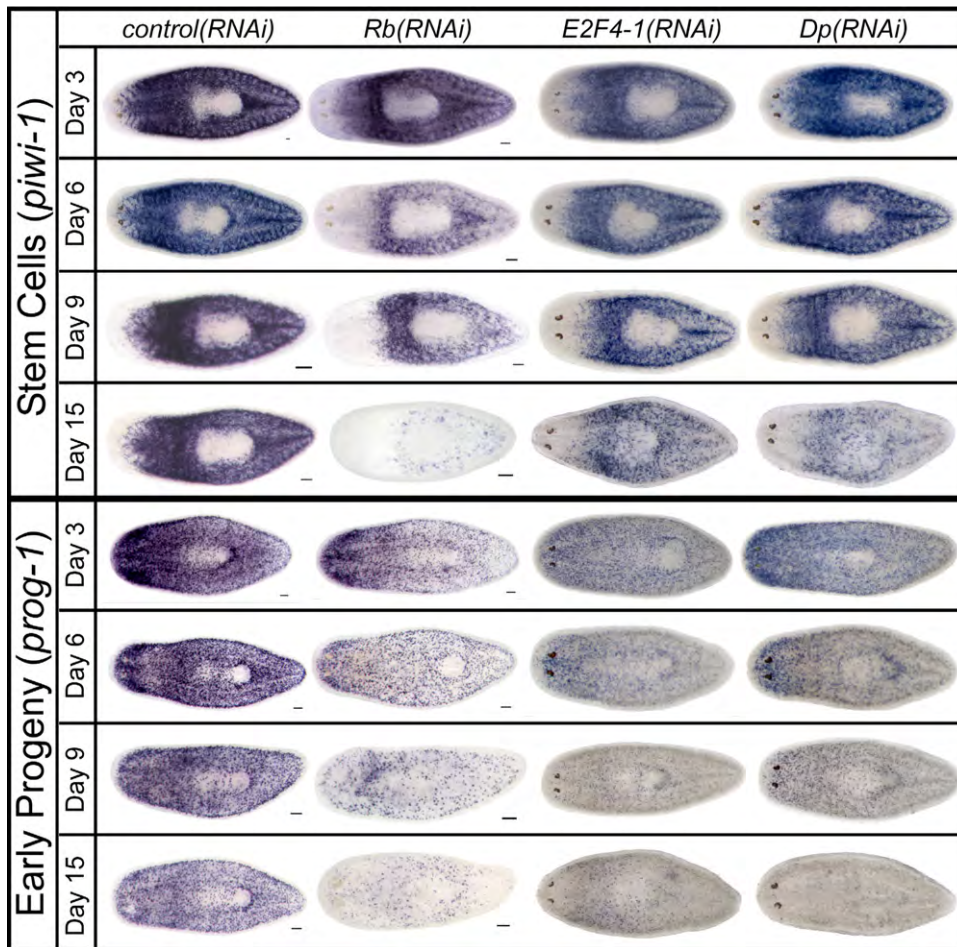


Fig. 4. Stem cell lineage development requires the Rb pathway. All panels show WISH for either stem cell or stem cell progeny markers during the time course of RNAi phenotypes. All worms used were 2–3 mm in length. Even at the hyper-proliferation stage for *E2F4-1* and *Dp* RNAi animals (day 3), increases in either stem cells or stem cell progeny are not seen. By day 15 post-RNAi we observed severe reduction of the stem cells and stem cell progeny, suggesting that the Rb pathway is ultimately required for cell proliferation, self-renewal, or cell survival.

Rb(RNAi) animals may be due to increased apoptosis of stem cells, as opposed to loss of self-renewal or increased exit from the cell cycle. To test this, we first measured global cell death by TUNEL labelling in *Rb(RNAi)* treated worms and then quantified cell corpses. Following *Rb(RNAi)*, we observed significant increases in cell death during the time course of phenotypic progression (Fig. 5A).

We hypothesized that the stem cell loss we observed was specifically due to increases in stem cell death. To test this, we performed a double labeling for PIWI-1 protein and TUNEL, and then quantified levels of co-localization in RNAi-treated worms. It should be noted that while the PIWI-1 antibody labels all *piwi-1*⁺ stem cells, the PIWI-1 protein also perdures into and labels early stem cell progeny to some extent (Guo et al., 2006; Scimone et al., 2011). We focused our analysis on day 6 after RNAi feedings as *Rb(RNAi)* animals still possess a substantial stem cell population at this time point yet also exhibit increased TUNEL staining (Figs. 4 and 5A). Following quantification of PIWI-1⁺TUNEL⁺ cells, we made several interesting observations. First, we unexpectedly detected TUNEL⁺PIWI-1⁺ cells in our *control(RNAi)* animals (Fig. 5C, E), which suggested that there is a basal level of cell death experienced by unperturbed PIWI⁺ cells in planarians. Second, we could not detect significant increases in cell death in the PIWI-1⁺ population of cells upon knockdown of *Rb* (Fig. 5E), which suggested that the stem cells may not require *Rb* for survival. Finally, in several more phenotypically-severe

Rb(RNAi) animals at this time point, we observed high levels of TUNEL labeling in anterior regions of animals where the stem cells had already been lost (Fig. 5D). Thus, while we could not conclude that *Rb* is required for stem cell survival, the contribution to increased global cell death is due to apoptosis of non-stem cell types. Similar to the role of p107 in the survival of mouse cortical neurons (Vanderluit et al., 2007), these dying cells may be the neural cell types in the planarian brain that also express planarian *Rb*, which was supported using TUNEL, the neural marker anti-SYNAPSIN, and DAPI (Fig. 5F). From these data, we concluded that *Rb* was not required for stem cell survival, and thus the loss of cell division and stem cell population in *Rb(RNAi)* animals was likely due to defects in self-renewal.

Smed-HDAC1 and *Smed-cyclinD* are also required for stem cell self-renewal

Our results on the core Rb pathway components in planarians showed a requirement for the pathway in stem cell self-renewal. However, we sought to extend our analyses to include an upstream and downstream regulator of RB function in other systems. It is known that interaction with chromatin modifiers is another major branch of RB functional activity (Chae et al., 2012; Cui et al., 2006; Dufourcq et al., 2002; Ferreira et al., 1998; Lu and Horvitz, 1998). For example, RB is known in other systems to bind several chromatin remodelers, including *histone deacetylase*

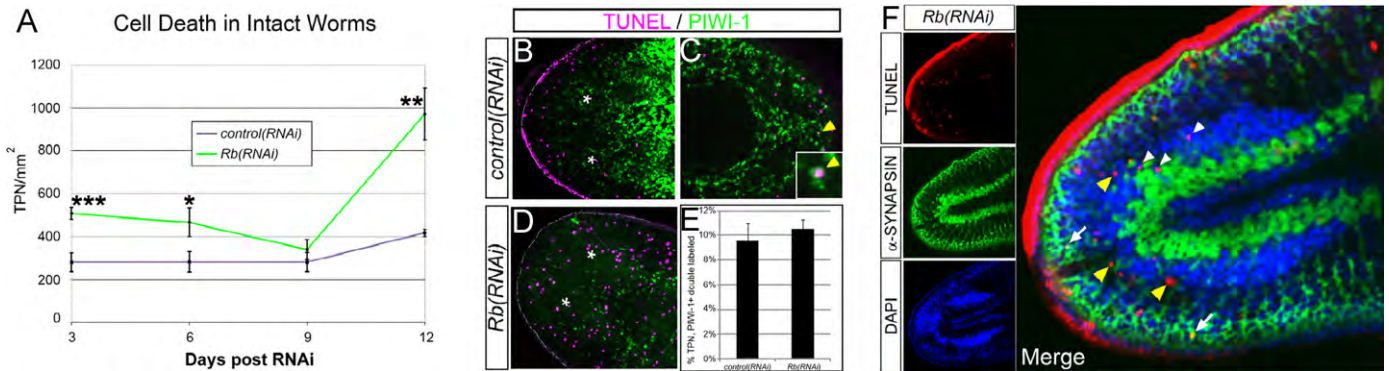


Fig. 5. Cell death quantification during the time course of the *Rb(RNAi)* phenotype. (A) We detected significant increases in TUNEL positive nuclei (TPN) at most time points of phenotypic progression (Student's *t*-test, error bars are standard error). (B)–(D) Anterior is to the left. Confocal images of PIWI-1 (green) and TUNEL (magenta) double stains at day 6 post-RNAi. Asterisks denote position of the eyes, dashed line denotes body-edge. Any strong staining at the body-edge is considered background. (B) *control(RNAi)*, head region; (C) *control(RNAi)*, tail region, inset shows a double-positive cell; (D) *Rb(RNAi)*, head region with minimal stem cells yet high TUNEL labeling in the brain region; (E) Quantification of TUNEL staining in PIWI-1⁺ cells between *control* and *Rb RNAi* animals; (F) A whole-mount stain on an *Rb(RNAi)* animal 9 days post RNAi, anterior is to the left. Using the pan-neural synaptic marker anti-SYNAPSIN (green) and nuclei label DAPI (blue), the brain is easily visualized. TUNEL⁺ cells (red) were detected within the boundaries of the brain (white arrowheads), as well as peripheral neurons of the head (white arrows). Many other cells labeled near the margin of the brain, and could not be distinctly counted as being neural in position (yellow arrowheads). From these data, some of the increased cell death observed when *Rb* is knocked down, occurs in the brain. Significance indicators: * = $p < 0.05$; ** = $p < 0.01$; *** = $p < 0.001$.

1 (*HDAC1*), which can mediate the transcriptional repression of RB target genes and also has roles in regulating embryonic stem cell self-renewal and differentiation (Dovey et al., 2010; Ferreira et al., 1998; van den Heuvel and Dyson, 2008). In addition, CyclinD-CDK4/6 and CyclinE-CDK2 complexes are well known to phosphorylate and modify RB activity (Malumbres and Barbacid, 2005). Similar to our analysis for the other components of the *Rb* pathway, we searched the planarian genome and transcriptome for *HDAC1*, *cyclinD*, *cyclinE*, and *CDKs* 2, 4, and 6. Interestingly, planarians were found to have 20 homologs to cyclin genes, though no homologs to *cyclinE* could be detected (their expression analysis is summarized in Table S2). To ensure that this sequence was not simply missing in planarians, 3 other flatworm genomes were examined and no *cyclinE* genes could be found, while 2 non-flatworm Lophotrochozoans had clear *cyclinE* genes. Thus, it appeared that the loss of an activating E2F in flatworms coincided with loss of *cyclinE* (see Discussion). For the CDK gene family, 30 CDK homologs were detected and a best reciprocal BLAST hit to CDK 2, 4, and 6 were all found (their expression analysis is summarized in Table S3). Importantly, we observed that the CyclinD-binding CDKs (4 and 6) were highly enriched in stem cells, whereas the predicted CyclinE-binding CDK (2) had virtually no expression in any cell compartment.

When the *S. mediterranea* genome was searched for the presence of an *HDAC1* homolog, a single ortholog with 75% amino acid identity to mouse *HDAC1* was found, which we have named *Smed-HDAC1* (*HDAC1* for the rest of this manuscript; originally found in the RNAi screen by Reddien et al. (2005a)). In addition, we found a single *cyclinD* ortholog (*Smed-cycD*). Although expression patterns for *cycD* could not be detected, in situ hybridization revealed that *HDAC1* was expressed in a stem cell specific pattern, which was ablated within 24 h following gamma irradiation (Fig. 6A). Importantly, following irradiation we observed remaining brain expression, similar to *Rb* (Fig. 1). Aligning the stem cell-specific RNAseq data to the *cycD* and *HDAC1* transcripts showed a 26.4- and 9.4-fold differential expression in the stem cell compartment over the rest of the worm, respectively (Table S1).

We next analyzed RNAi phenotypes during intact homeostasis and regeneration following injury, and observed stem cell-defective phenotypes in both contexts (Fig. 6C). Similar to the observed phenotypes on cell division and lineage production in *Rb(RNAi)* worms, *HDAC1* and *cycD* RNAi animals displayed a loss

of stem cells, progeny, and H3P staining at early time points following RNAi (Fig. 6B, D). Interestingly, the kinetics of the loss of these markers was substantially more rapid than observed for *Rb*, *E2F4-1*, or *Dp*. Whether this is due to real mechanistic differences or simply different RNAi kinetics, could not be determined. These data, however, were consistent with the notion that *cycD* and *HDAC1* may modulate the functions of RB in stem cell division and self-renewal in planarians. In future studies, it will be important to determine the genomic targets of RB and *HDAC1* as well as the phosphorylation status of RB during the cell cycle to further understand the biology of stem cell self-renewal in planarians.

Discussion

Evolution of the *Rb* pathway and cell division

It is widely thought that the more ancient the conservation in genetic pathways, the more difficult it is for natural selection to alter them. Here we demonstrated that despite conservation from plants to animals, the *Rb* pathway can be substantially modified. In the first study to examine *Rb* pathway function and gene complement in Lophotrochozoans, we showed that freshwater planarians have conserved the ancestral roles for RB in cell division and cell death. However, flatworms as a phylum have undergone loss of an activating E2F homolog. Further analysis showed that flatworms have also lost a *cyclinE* homolog, which is a critical regulator of RB activity in other systems. It is interesting to hypothesize that the loss of either *cyclinE* or the activating E2F was an initial trigger that selected for the rapid loss of the other gene to balance pathway activity (Fig. 7). On the other hand, perhaps another cyclin has taken up the role of *cyclinE* in planarians, or another molecule has substituted for the loss of an activating E2F. Interestingly, the canonical binding partner of CyclinE, CDK2, still exists in planarians, but has extraordinarily low expression based on RNAseq, suggesting that it may no longer function in the cell cycle (Fig. 7).

Our analysis of planarian RB has shown that it has more sequence similarity to p107/p130 in vertebrates, and our functional analyses support this conclusion. Similar to p107 in mice, we show that *Smed-Rb* does not behave like a classical tumor

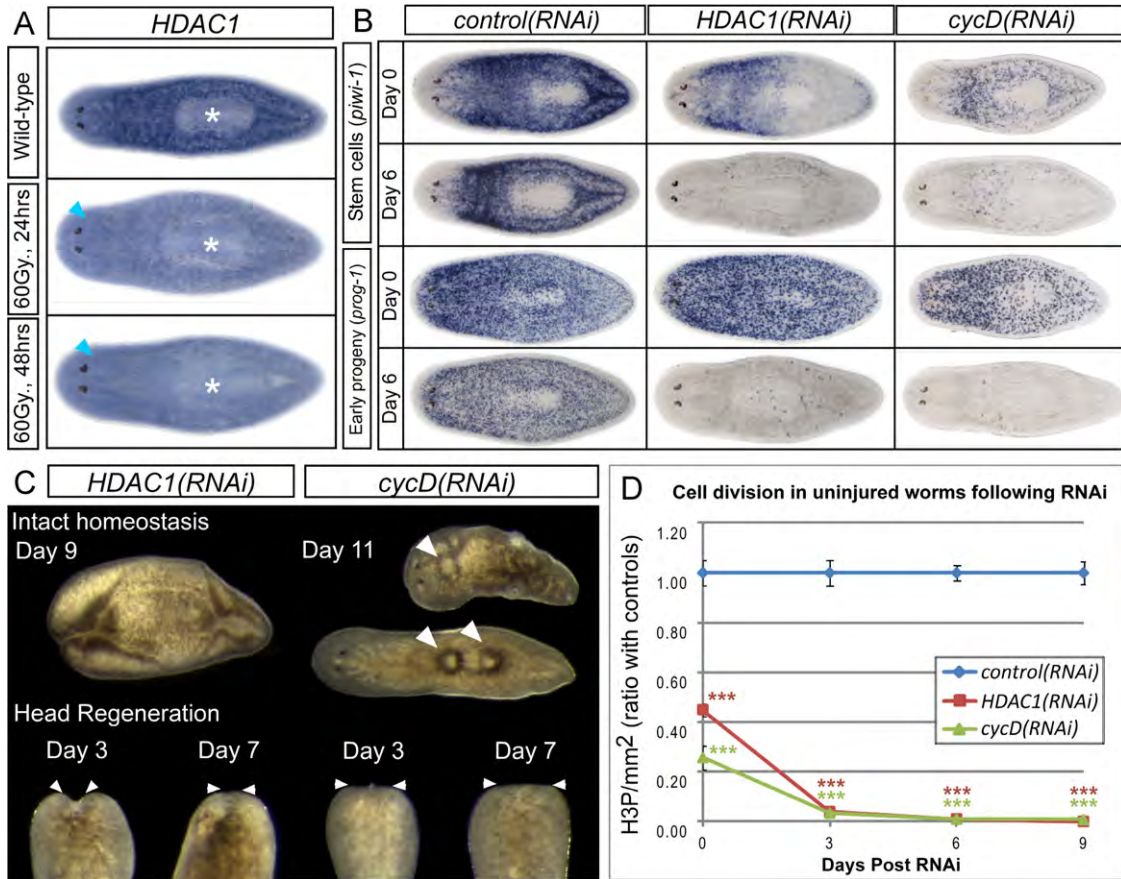


Fig. 6. Functions of *HDAC1* and *cycD* in planarians. (A) Similar to *Rb*, *HDAC1* showed a stem cell specific expression pattern, which was ablated by 24 h following 60 Gy. of irradiation. Also observed was brain-specific staining once the stem cell pattern was ablated (blue arrowheads). Asterisks mark the pharynx. (B) Effects of *HDAC1* and *cycD* RNAi on stem cell lineage development showed dramatic reduction of both the stem cell population and stem cell progeny by day 6 post-RNAi. (C) When knocked down by RNAi, *HDAC1* and *cycD* animals showed stem cell defective phenotypes during both intact homeostasis and during head regeneration (white arrowheads mark dorsal lesions or amputation plane). (D) As stem cells are lost, cell division goes down as expected, as measured by anti-H3P (Student's *t*-test, error bars are standard error). ***=*p* < 0.001.

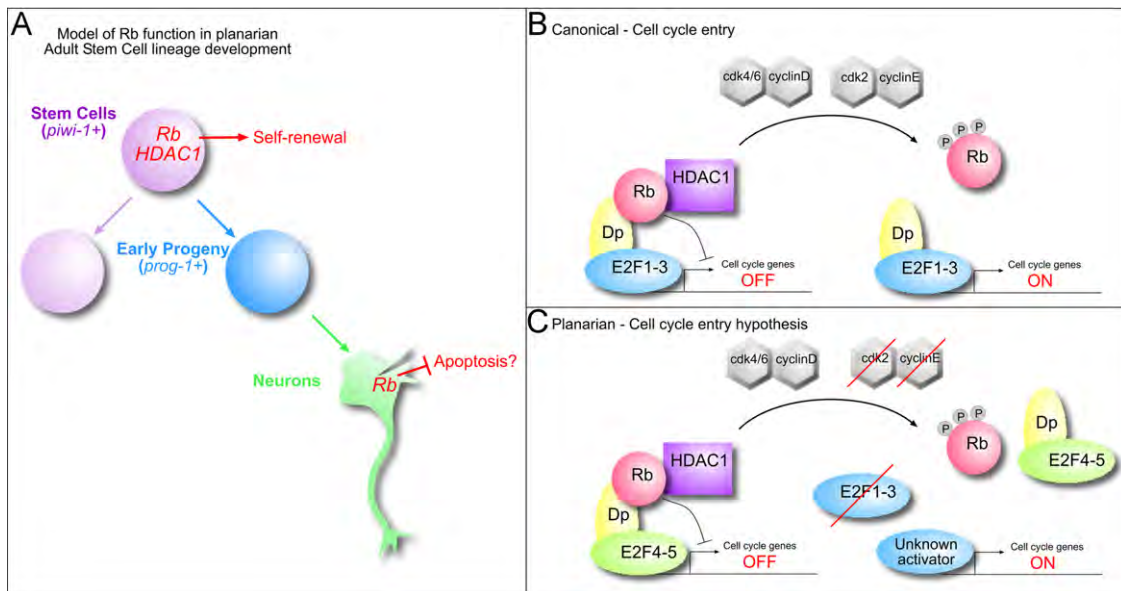


Fig. 7. Model of Rb pathway function in planarians. (A) Planarian Rb functions at multiple levels in stem cell lineage development. Our data suggested that *Rb* and *HDAC1* are specifically expressed in both stem cells and post-mitotic neurons in the brain. When knocked down by RNAi *Rb* and *HDAC1* were required for stem cell self-renewal. Some of the increase in cell death in *Rb*(RNAi) animals occurs in the brain, and *Rb* may have a pro-survival role in neurons. (B) Shown is the canonical regulation of Rb activity by phosphorylation by cyclin/CDK complexes. When *Rb* is inactivated, activating *E2F1-3*/*Dp* complexes activate transcription of genes that drive entry into the cell cycle. (C) Based on the data, shown is a graphical hypothesis how planarian Rb functions in adult stem cell proliferation control. Despite not activating *E2F*, and no *cyclinE*, the core Rb pathway in planarians still controls cell division. We hypothesize that *HDAC1* and *CyclinD* are still involved in this process, but may function slightly differently to compensate for *cyclinE* and *E2F1-3* loss. Red line through *cyclinE* denotes gene loss, while red line through *CDK2* denotes no expression. We hypothesize that with no activating *E2F1-3*, planarians may use an unknown activating transcription factor to transcribe cell cycle genes and enter the cell cycle.

suppressor: it is highly transcribed in cycling cells, is required for cell-cycle progression, and promotes cell survival. Unlike p107, it does not appear that *Smed-Rb* is required for differentiation because stem cell progeny were produced during the entire time course of the *Rb(RNAi)* phenotypic progression (Fig. 4). Overall, our results support the previous hypothesis that the ancestral function of RB-like molecules was in cell division and cell survival, similar to p107 and p130 in vertebrates, and when combined with the plant and vertebrate data, also suggests that RB evolved for specific roles in stem cell biology. It will be interesting to further test whether the *Drosophila Rb* genes have any unappreciated role in adult stem cell compartments such as intestinal stem cells or neural stem cells.

E2F/Dp-independent roles of planarian Rb?

In other systems, RB proteins have been reported to have approximately 100 binding partners in addition to E2F and DP proteins (van den Heuvel and Dyson, 2008). Thus, similar to other systems (Chi and Reinke, 2006), it is likely that planarian RB may have roles independent of E2F4-1/DP and cell cycle regulation, which is supported by the differences in phenotypic progression between *Rb(RNAi)* and *E2F4-1* or *Dp RNAi* worms. For example, the very different kinetics of cell division suggests that RB may have a different role in the stem cell from E2F4-1 and DP. Perhaps this role is in chromatin remodeling to repress a different set of target genes than the E2F4-1 targets. A recent report of another RB-binding chromatin remodeler, *RbAp48*, also showed a stem cell defective phenotype in the planarian *Dugesia japonica*, although lineage markers were not used to analyze the phenotype (Bonucelli et al., 2010). Another well-known binding partner of RB proteins, which is also involved in chromatin remodeling, is histone deacetylase 1 (*HDAC1*) (Ferreira et al., 1998). We find both *RbAp48* and *HDAC1* to be very highly expressed specifically in planarian stem cells (Table S1), and our results upon knockdown of *HDAC1* are consistent with the self-renewal and proliferation defects observed for *Rb(RNAi)*. In future studies, it will be interesting to determine biochemically what other proteins bind RB in planarians to elucidate complexes that function independent of cell cycle regulation. Given the expression of *Rb* and *HDAC1* in the planarian brain and cell death observed in the brain of *Rb(RNAi)* animals, one possibility is that RB functions in a specific, pro-survival protein complex in planarian neurons (Fig. 7). However, it remains formally possible that the increases in cell death observed in *Rb(RNAi)* planarians, or *Rb*-mutants in other model systems, could be due to cell non-autonomous effects on differentiated tissues of losing the stem cell population. We do not believe this to be the case because early time points in the *Rb(RNAi)* time course have not lost appreciable numbers of stem cells or stem cell progeny, yet show significantly increased cell death (Figs. 4 and 5A).

p53 and Rb tumor suppressor pathways in stem cell lineage development

In mammals, *Rb* and *p53* pathways are known to converge and synergize in many tumor types, such that double mutants of both genes are more severe than either single mutants (Beck et al., 2000; Berman et al., 2008; Chow et al., 2011; Meuwissen et al., 2003; Miyamoto et al., 1996; Moon et al., 2008; Schwartzman et al., 2011; Zhou et al., 2006). We have previously shown that planarian *p53* primarily functions in newly-born stem cell progeny (*prog-1*⁺ population) to promote differentiation and cell cycle exit. Therefore, a simple model for loss of stem cells in *Rb(RNAi)* animals would be the de-repression of *p53* in stem cells, which would cause cell cycle exit and premature differentiation. When we tested *Rb(RNAi)*

animals for de-repression of *p53*, we did not observe increases in *p53* expression, and therefore we believe that crosstalk between these pathways may not be occurring in planarians (Fig. S4). In addition, *p53* is expressed in a different spatial domain than *Rb*, and *p53(RNAi)* results in dramatically different effects on lineage production than knockdown of the *Rb* pathway (Pearson and Sanchez Alvarado, 2010). Finally, we did not observe increases in differentiating cells in *Rb(RNAi)* animals (Fig. 4). Together this suggests that both pathways serve fundamentally different roles in stem cell lineage determination and cell cycle control (Fig. 7A). This is not entirely unexpected because while the *Rb* and *p53* pathways converge in mammalian neural stem cell lineage development and tumorigenesis, they appear to have differing roles in the hematopoietic stem cell compartment (Liu et al., 2009; Walkley and Orkin, 2006). In future experiments, it will be critical to understand what the genomic targets of each pathway are in order to further understand their roles in stem cell lineage development and proliferation control.

Acknowledgements

We would like to thank Alejandro Sánchez Alvarado (Stowers Institute, HHMI) for advice and reagents, and Eric Ross for aligning RNAseq data to specific transcripts. Thanks to S. Hutchinson and K. Gurley for comments on the manuscript. This work was supported by the Ontario Institute for Cancer Research (OICR) New Investigator award (#IA-026).

Appendix A. Supporting information

Supplementary data associated with this article can be found in the online version at <http://dx.doi.org/10.1016/j.ydbio.2012.10.025>.

References

- Attwooll, C., Lazzarini Denchi, E., Helin, K., 2004. The E2F family: specific functions and overlapping interests. *EMBO J.* 23, 4709–4716.
- Beck, Z., Kiss, A., Toth, F.D., Szabo, J., Bacsí, A., Balogh, E., Borbely, A., Telek, B., Kovacs, E., Olah, E., Rak, K., 2000. Alterations of P53 and RB genes and the evolution of the accelerated phase of chronic myeloid leukemia. *Leuk. Lymphoma.* 38, 587–597.
- Berman, S.D., Calo, E., Landman, A.S., Danielian, P.S., Miller, E.S., West, J.C., Fonhoue, B.D., Caron, A., Bronson, R., Bouxsein, M.L., Mukherjee, S., Lees, J.A., 2008. Metastatic osteosarcoma induced by inactivation of Rb and p53 in the osteoblast lineage. *Proc. Nat. Acad. Sci. U.S.A.* 105, 11851–11856.
- Betz, R., Gray, S.G., Ekstrom, C., Larsson, C., Ekstrom, T.J., 1998. Human histone deacetylase 2, HDAC2 (Human RPD3), is localized to 6q21 by radiation hybrid mapping. *Genomics* 52, 245–246.
- Bonucelli, L., Rossi, L., Lena, A., Scarcelli, V., Rainaldi, G., Evangelista, M., Iacopetti, P., Gremigni, V., Salvetti, A., 2010. An RbAp48-like gene regulates adult stem cells in planarians. *J. Cell Sci.* 123, 690–698.
- Burkhardt, D.L., Sage, J., 2008. Cellular mechanisms of tumour suppression by the retinoblastoma gene. *Nat. Rev. Cancer* 8, 671–682.
- Cao, L., Peng, B., Yao, L., Zhang, X., Sun, K., Yang, X., Yu, L., 2010. The ancient function of RB-E2F pathway: insights from its evolutionary history. *Biol. Direct.* 5, 55.
- Chae, H.D., Lee, M.R., Broxmeyer, H.E., 2012. 5-Aminoimidazole-4-carboxamide ribonucleoside induces G(1)/S arrest and Nanog downregulation via p53 and enhances erythroid differentiation. *Stem Cells* 30, 140–149.
- Chi, W., Reinke, V., 2006. Promotion of oogenesis and embryogenesis in the *C. elegans* gonad by EFL-1/DPL-1 (E2F) does not require LIN-35 (pRB). *Development* 133, 3147–3157.
- Chicas, A., Wang, X., Zhang, C., McCurrach, M., Zhao, Z., Mert, O., Dickins, R.A., Narita, M., Zhang, M., Lowe, S.W., 2010. Dissecting the unique role of the retinoblastoma tumor suppressor during cellular senescence. *Cancer Cell* 17, 376–387.
- Chow, L.M., Endersby, R., Zhu, X., Rankin, S., Qu, C., Zhang, J., Bronsner, A., Ellison, D.W., Baker, S.J., 2011. Cooperativity within and among Pten, p53, and Rb pathways induces high-grade astrocytoma in adult brain. *Cancer Cell* 19, 305–316.
- Classon, M., Harlow, E., 2002. The retinoblastoma tumour suppressor in development and cancer. *Nat. Rev. Cancer* 2, 910–917.

- Crosby, M.E., Almasan, A., 2004. Opposing roles of E2Fs in cell proliferation and death. *Cancer Biol. Ther.* 3, 1208–1211.
- Cui, M., Kim, E.B., Han, M., 2006. Diverse chromatin remodeling genes antagonize the Rb-involved SynMuv pathways in *C. elegans*. *PLoS Genet.* 2, e74.
- Dimova, D.K., Stevaux, O., Frolov, M.V., Dyson, N.J., 2003. Cell cycle-dependent and cell cycle-independent control of transcription by the *Drosophila* E2F/RB pathway. *Genes Dev.* 17, 2308–2320.
- Dora, E.G., Rudin, N., Martell, J.R., Esposito, M.S., Ramirez, R.M., 1999. RPD3 (REC3) mutations affect mitotic recombination in *Saccharomyces cerevisiae*. *Curr. Genet.* 35, 68–76.
- Dovey, O.M., Foster, C.T., Cowley, S.M., 2010. *Histone deacetylase 1* (HDAC1), but not HDAC2, controls embryonic stem cell differentiation. *Proc. Nat. Acad. Sci. U.S.A.* 107, 8242–8247.
- Dufourcq, P., Victor, M., Gay, F., Calvo, D., Hodgkin, J., Shi, Y., 2002. Functional requirement for *histone deacetylase 1* in *Caenorhabditis elegans* gonadogenesis. *Mol. Cell. Biol.* 22, 3024–3034.
- Eisenhoffer, G.T., Kang, H., Sanchez Alvarado, A., 2008. Molecular analysis of stem cells and their descendants during cell turnover and regeneration in the planarian *Schmidtea mediterranea*. *Cell Stem. Cell* 3, 327–339.
- Elliott, S.A., Sanchez Alvarado, A., 2012. The history and enduring contributions of planarians to the study of animal regeneration. *Wiley Interdiscip. Rev. Dev. Biol.*, n/a–n/a.
- Ferreira, R., Magnaghi-Jaulin, L., Robin, P., Harel-Bellan, A., Trouche, D., 1998. The three members of the pocket proteins family share the ability to repress E2F activity through recruitment of a *histone deacetylase*. *Proc. Nat. Acad. Sci. U.S.A.* 95, 10493–10498.
- Fraguas, S., Barberan, S., Cebria, F., 2011. EGFR signaling regulates cell proliferation, differentiation and morphogenesis during planarian regeneration and homeostasis. *Dev. Biol.* 354, 87–101.
- Frolov, M.V., Huen, D.S., Stevaux, O., Dimova, D., Balczarek-Strang, K., Elsdon, M., Dyson, N.J., 2001. Functional antagonism between E2F family members. *Genes Dev.* 15, 2146–2160.
- Guo, T., Peters, A.H., Newmark, P.A., 2006. A bruno-like gene is required for stem cell maintenance in planarians. *Dev. Cell* 11, 159–169.
- Hayashi, T., Asami, M., Higuchi, S., Shibata, N., Agata, K., 2006. Isolation of planarian X-ray-sensitive stem cells by fluorescence-activated cell sorting. *Dev. Growth Differ.* 48, 371–380.
- Jiang, H., Martin, V., Alonso, M., Gomez-Manzano, C., Fueyo, J., 2010. RB-E2F1: molecular rheostat for autophagy and apoptosis. *Autophagy* 6, 1216–1217.
- Kadosh, D., Struhl, K., 1998. *Histone deacetylase* activity of Rpd3 is important for transcriptional repression in vivo. *Genes Dev.* 12, 797–805.
- Labbe, R.M., Irimia, M., Currie, K.W., Lin, A., Zhu, S.J., Brown, D.D., Ross, E.J., Voisin, V., Bader, G.D., Blencowe, B.J., Pearson, B.J., 2012. A comparative transcriptomic analysis reveals conserved features of stem cell pluripotency in planarians and mammals. *Stem Cells*.
- Liu, Y., Elf, S.E., Miyata, Y., Sashida, G., Huang, G., Di Giandomenico, S., Lee, J.M., Deblasio, A., Menendez, S., Antipin, J., Reva, B., Koff, A., Nimer, S.D., 2009. p53 regulates hematopoietic stem cell quiescence. *Cell Stem. Cell* 4, 37–48.
- Lu, X., Horvitz, H.R., 1998. lin-35 and lin-53, two genes that antagonize a *C. elegans* Ras pathway, encode proteins similar to Rb and its binding protein RbAp48. *Cell* 95, 981–991.
- Malumbres, M., Barbacid, M., 2005. Mammalian cyclin-dependent kinases. *Trends Biochem. Sci.* 30, 630–641.
- Manning, A.L., Dyson, N.J., 2011. pRB, a tumor suppressor with a stabilizing presence. *Trends Cell Biol.* 21, 433–441.
- Messenguy, F., Vierendeels, F., Scherens, B., Dubois, E., 2000. In *Saccharomyces cerevisiae*, expression of arginine catabolic genes CAR1 and CAR2 in response to exogenous nitrogen availability is mediated by the Ume6 (CargRI)-Sin3 (CargRII)-Rpd3 (CargRIII) complex. *J. Bacteriol.* 182, 3158–3164.
- Meuwissen, R., Linn, S.C., Linnoila, R.I., Zevenhoven, J., Mooi, W.J., Berns, A., 2003. Induction of small cell lung cancer by somatic inactivation of both Trp53 and Rb1 in a conditional mouse model. *Cancer Cell* 4, 181–189.
- Miyamoto, H., Shuin, T., Ikeda, I., Hosaka, M., Kubota, Y., 1996. Loss of heterozygosity at the p53, RB, DCC and APC tumor suppressor gene loci in human bladder cancer. *J. Urol.* 155, 1444–1447.
- Moon, N.S., Di Stefano, L., Morris, E.J., Patel, R., White, K., Dyson, N.J., 2008. E2F and p53 induce apoptosis independently during *Drosophila* development but intersect in the context of DNA damage. *PLoS Genet.* 4, e1000153.
- Newmark, P.A., Reddien, P.W., Cebria, F., Sanchez Alvarado, A., 2003. Ingestion of bacterially expressed double-stranded RNA inhibits gene expression in planarians. *Proc. Nat. Acad. Sci. U.S.A.* 100 (Suppl 1), 11861–11865.
- Newmark, P.A., Sanchez Alvarado, A., 2002. Not your father's planarian: a classic model enters the era of functional genomics. *Nat. Rev. Genet.* 3, 210–219.
- Oviedo, N.J., Pearson, B.J., Levin, M., Sanchez Alvarado, A., 2008. Planarian PTEN homologs regulate stem cells and regeneration through TOR signalling. *Dis. Models Mech.* 1, 131–143.
- Pearson, B.J., Eisenhoffer, G.T., Gurley, K.A., Rink, J.C., Miller, D.E., Sanchez Alvarado, A., 2009. Formaldehyde-based whole-mount in situ hybridization method for planarians. *Dev. Dyn.* 238, 443–450.
- Pearson, B.J., Sanchez Alvarado, A., 2010. A planarian p53 homolog regulates proliferation and self-renewal in adult stem cell lineages. *Development* 137, 213–221.
- Pellettieri, J., Alvarado, A.S., 2007. Cell turnover and adult tissue homeostasis: from humans to planarians. *Annu. Rev. Genet.* 41, 83–105.
- Reddien, P.W., Bermange, A.L., Murfitt, K.J., Jennings, J.R., Sanchez Alvarado, A., 2005a. Identification of genes needed for regeneration, stem cell function, and tissue homeostasis by systematic gene perturbation in planaria. *Dev. Cell* 8, 635–649.
- Reddien, P.W., Oviedo, N.J., Jennings, J.R., Jenkin, J.C., Sanchez Alvarado, A., 2005b. SMEDWI-2 is a PIWI-like protein that regulates planarian stem cells. *Science* 310, 1327–1330.
- Reddien, P.W., Sanchez Alvarado, A., 2004. Fundamentals of planarian regeneration. *Annu. Rev. Cell Dev. Biol.* 20, 725–757.
- Robb, S.M., Ross, E., Sanchez Alvarado, A., 2008. SmedGD: the *Schmidtea mediterranea* genome database. *Nucleic Acids Res.* 36, D599–D606.
- Rossi, V., Hartings, H., Motto, M., 1998. Identification and characterization of an RPD3 homologue from maize (*Zea mays* L.) that is able to complement an rpd3 null mutant of *Saccharomyces cerevisiae*. *Mol. Gen. Genet.* 258, 288–296.
- Sánchez Alvarado, A., Newmark, P.A., Robb, S.M., Juste, R., 2002. The *Schmidtea mediterranea* database as a molecular resource for studying platyhelminthes, stem cells and regeneration. *Development* 129, 5659–5665.
- Sánchez Alvarado, A., Reddien, P. W., Newmark, P., Nusbaum, C., 2003. Proposal for the Sequencing of a New Target Genome: White Paper for a Planarian Genome Project.
- Schvartzman, J.M., Duijf, P.H., Sotillo, R., Coker, C., Benezra, R., 2011. Mad2 is a critical mediator of the chromosome instability observed upon Rb and p53 pathway inhibition. *Cancer Cell* 19, 701–714.
- Scimone, M.L., Srivastava, M., Bell, G.W., Reddien, P.W., 2011. A regulatory program for excretory system regeneration in planarians. *Development* 138, 4387–4398.
- Soleimani, V.D., Yin, H., Jahani-Asl, A., Ming, H., Kockx, C.E., van Ijcken, W.F., Grosveld, F., Rudnicki, M.A., 2012. Snail regulates MyoD binding-site occupancy to direct enhancer switching and differentiation-specific transcription in myogenesis. *Mol. Cell* 47, 457–468.
- Stevaux, O., Dimova, D., Frolov, M.V., Taylor-Harding, B., Morris, E., Dyson, N., 2002. Distinct mechanisms of E2F regulation by *Drosophila* RBF1 and RBF2. *EMBO J.* 21, 4927–4937.
- Tu, K.C., Pearson, B.J., Sanchez Alvarado, A., 2012. TORC1 is required to balance cell proliferation and cell death in planarians. *Dev. Biol.* 365, 458–469.
- Van den Heuvel, S., Dyson, N.J., 2008. Conserved functions of the pRB and E2F families. *Nat. Rev. Mol. Cell Biol.* 9, 713–724.
- Vanderluit, J.L., Wylie, C.A., McClellan, K.A., Ghanem, N., Fortin, A., Callaghan, S., MacLaurin, J.G., Park, D.S., Slack, R.S., 2007. The Retinoblastoma family member p107 regulates the rate of progenitor commitment to a neuronal fate. *J. Cell Biol.* 178, 129–139.
- Wagner, D.E., Wang, I.E., Reddien, P.W., 2011. Clonogenic neoblasts are pluripotent adult stem cells that underlie planarian regeneration. *Science* 332, 811–816.
- Walkley, C.R., Orkin, S.H., 2006. Rb is dispensable for self-renewal and multilineage differentiation of adult hematopoietic stem cells. *Proc. Nat. Acad. Sci. U.S.A.* 103, 9057–9062.
- Wenemoser, D., Lapan, S.W., Wilkinson, A.W., Bell, G.W., Reddien, P.W., 2012. A molecular wound response program associated with regeneration initiation in planarians. *Genes Dev.* 26, 988–1002.
- Wildwater, M., Campilho, A., Perez-Perez, J.M., Heidstra, R., Bliou, I., Korthout, H., Chatterjee, J., Mariconti, L., Gruissem, W., Scheres, B., 2005. The RETINOBLASTOMA-RELATED gene regulates stem cell maintenance in Arabidopsis roots. *Cell* 123, 1337–1349.
- Wirt, S.E., Sage, J., 2010. p107 in the public eye: an Rb understudy and more. *Cell Div.* 5, 9.
- Zhou, Z., Flesken-Nikitin, A., Corney, D.C., Wang, W., Goodrich, D.W., Roy-Burman, P., Nikitin, A.Y., 2006. Synergy of p53 and Rb deficiency in a conditional mouse model for metastatic prostate cancer. *Cancer Res.* 66, 7889–7898.

Wnt/ β -catenin signaling promotes differentiation, not self-renewal, of human embryonic stem cells and is repressed by Oct4

Kathryn C. Davidson, Allison M. Adams, Jamie M. Goodson, Circe E. McDonald, Jennifer C. Potter, Jason D. Berndt, Travis L. Biechele, Russell J. Taylor, and Randall T. Moon¹

Department of Pharmacology, Howard Hughes Medical Institute, and the Institute for Stem Cell and Regenerative Medicine, University of Washington School of Medicine, Seattle, WA 98109

Edited* by Philip A. Beachy, Stanford University, Stanford, CA, and approved February 1, 2012 (received for review November 14, 2011)

Signal transduction pathways play diverse, context-dependent roles in vertebrate development. In studies of human embryonic stem cells (hESCs), conflicting reports claim Wnt/ β -catenin signaling promotes either self-renewal or differentiation. We use a sensitive reporter to establish that Wnt/ β -catenin signaling is not active during hESC self-renewal. Inhibiting this pathway over multiple passages has no detrimental effect on hESC maintenance, whereas activating signaling results in loss of self-renewal and induction of mesoderm lineage genes. Following exposure to pathway agonists, hESCs exhibit a delay in activation of β -catenin signaling, which led us to postulate that Wnt/ β -catenin signaling is actively repressed during self-renewal. In support of this hypothesis, we demonstrate that OCT4 represses β -catenin signaling during self-renewal and that targeted knockdown of OCT4 activates β -catenin signaling in hESCs. Using a fluorescent reporter of β -catenin signaling in live hESCs, we observe that the reporter is activated in a very heterogeneous manner in response to stimulation with Wnt ligand. Sorting cells on the basis of their fluorescence reveals that hESCs with elevated β -catenin signaling express higher levels of differentiation markers. Together these data support a dominant role for Wnt/ β -catenin signaling in the differentiation rather than self-renewal of hESCs.

Embryonic stem cells (ESCs) derived from the inner cell mass of preimplantation-stage mammalian embryos are pluripotent cells capable of proliferating in their undifferentiated state in vitro while maintaining the ability to give rise to all three primary germ layers. Once established in culture, ESC lines can be propagated indefinitely. Whereas human and mouse ESCs share many key characteristics, these species differ in the signal transduction pathways that influence self-renewal. This may be partly due to the fact that human ESCs (hESCs) more closely resemble epiblast stem cells from the mouse, which correspond to a slightly later developmental stage than inner cell mass cells (1, 2).

The Wnt gene family encodes evolutionarily conserved, secreted glycoproteins that act as ligands to stimulate several signal transduction pathways, thereby regulating processes in both embryonic development and in adults (3–5). Signaling through the best understood pathway, the Wnt/ β -catenin pathway, is mediated through posttranslational regulation of the stability of β -catenin. Activation of Wnt signaling leads to the accumulation of β -catenin in nuclei, where it binds to high mobility group (HMG) box transcription factors of the T-cell factor (TCF) and lymphoid enhancing factor (LEF) families and promotes context-dependent changes in transcription (5).

Wnt/ β -catenin signaling has been implicated in the maintenance of both mouse and human ESCs in vitro (6–13). Wnt signaling has also been reported to promote the acquisition of a pluripotent state during reprogramming of somatic cells to induced pluripotent stem cells (14, 15). Many studies have shown that activating Wnt/ β -catenin signaling promotes self-renewal of mouse ESCs (mESCs) (6, 7, 10–13), whereas reciprocal loss-of-function (LOF) studies indicate that β -catenin is required for

multilineage differentiation but is dispensable for self-renewal (13, 16, 17).

The role of Wnt/ β -catenin signaling in hESCs is less clear due to contradictory results among published studies. Sato et al. (7) found that activating the Wnt/ β -catenin pathway with either Wnt3A or a GSK3 inhibitor, BIO, maintained the self-renewal of hESCs under feeder-free conditions. Conversely, others have reported that Wnt3A or GSK3 inhibitors lead to differentiation of hESCs toward primitive streak and definitive endoderm lineages (18, 19). Ullmann et al. (20) found that BIO promoted undifferentiated cellular morphology and maintained expression of pluripotency markers in short-term assays, but was not sufficient to expand undifferentiated hESCs over multiple passages. In other studies, Wnt3A and Wnt1 transiently stimulated proliferation and/or increased clonal survival of hESCs, but failed to maintain other functional measures of pluripotency over several passages (21–23). Whether Wnt/ β -catenin signaling maintains hESCs in an undifferentiated and self-renewing state, or whether it promotes differentiation, remains controversial.

Results

Activation of Wnt/ β -Catenin Signaling Promotes Loss of Self-Renewal of hESCs. To resolve the roles of Wnt/ β -catenin signaling in hESCs, we first investigated the consequences of activating the pathway during multiple passages of the cells. hESCs cultured with Wnt3A conditioned medium (CM) adopt a morphology characteristic of differentiation (Fig. 1A) and down-regulate expression of stem cell surface markers, GCTM2 and CD9 (Fig. 1B). If Wnt/ β -catenin signaling were promoting the maintenance of hESCs, then one would expect the application of exogenous Wnt3A ligand should promote expansion of phenotypically undifferentiated cells via self-renewal. Therefore, we measured the total number of GCTM2⁺/CD9⁺ cells present when hESCs were cultured with Wnt3A CM at 1- and 2-wk time points. We observed that increasing concentrations of Wnt3A CM led to significantly fewer undifferentiated hESCs after 2 wk compared with control CM (Fig. 1C). Remarkably, this change occurred despite cells being cultured on mouse embryonic fibroblasts (MEFs) and in medium otherwise supportive of maintenance. Likewise, treatment of hESCs with Wnt3A CM also led to down-regulation of *POU5F1* (OCT4) and *NANOG* mRNA levels relative to control L cell CM (LCM) (Fig. 1D). Importantly, the loss of maintenance markers occurred in a dose-dependent manner. We also activated Wnt/ β -catenin signaling with recombinant

Author contributions: K.C.D. designed research; K.C.D., A.M.A., J.M.G., C.E.M., J.C.P., J.D.B., and R.J.T. performed research; A.M.A. and T.L.B. contributed new reagents/analytic tools; K.C.D. analyzed data; and K.C.D. and R.T.M. wrote the paper.

The authors declare no conflict of interest.

*This Direct Submission article had a prearranged editor.

Freely available online through the PNAS open access option.

¹To whom correspondence should be addressed. E-mail: rtmooon@u.washington.edu.

This article contains supporting information online at www.pnas.org/lookup/suppl/doi:10.1073/pnas.1118777109/-DCSupplemental.

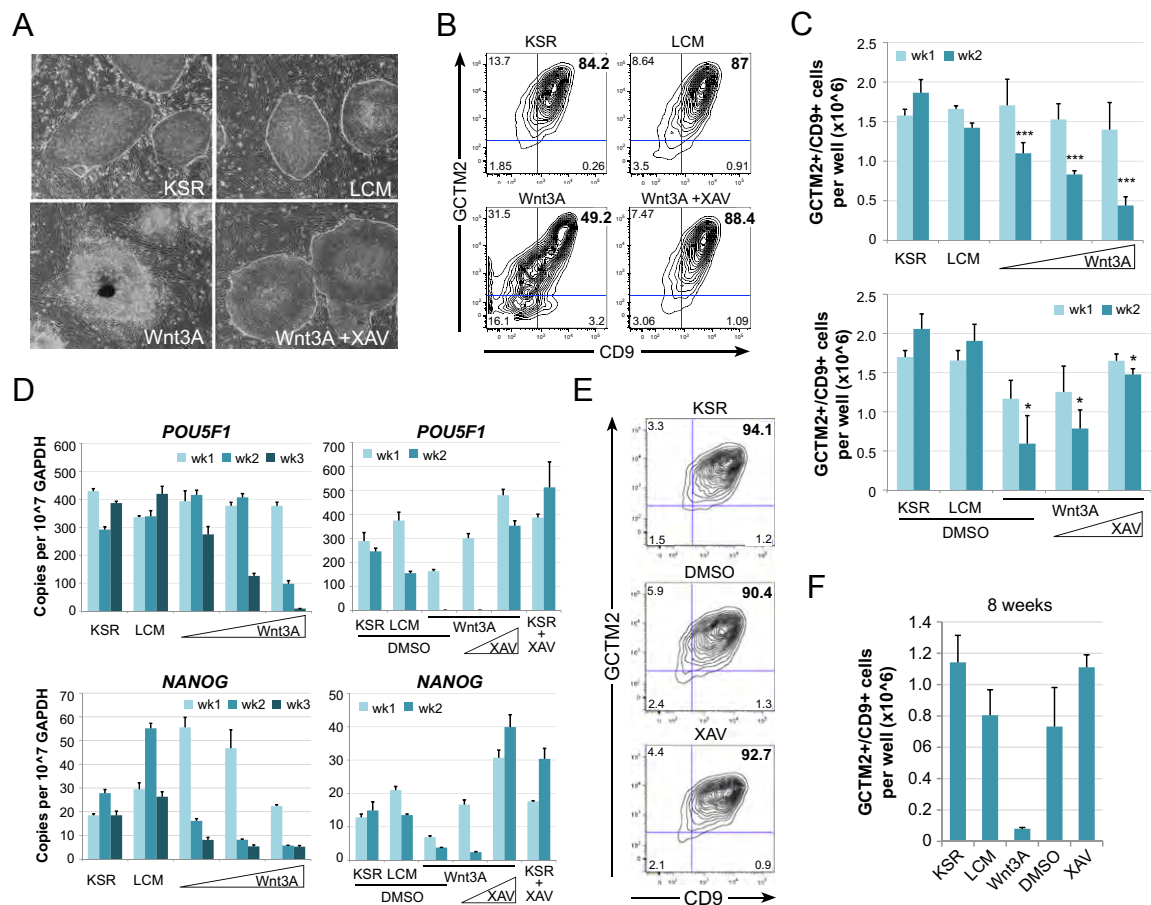


Fig. 1. Wnt3A fails to maintain hESCs. (A) H1 cells cultured for 1 wk on MEFs in KSR media, 50% (vol/vol) control L cell CM (LCM) in KSR, 50% (vol/vol) Wnt3A CM, or 50% Wnt3A CM + 2.5 μ M XAV. DMSO vehicle control was included in all media without XAV. (B) Representative flow cytometric plots showing GCTM2 and CD9 coexpression in hESCs cultured in the same conditions as A for 1 wk. (C) Graph showing the total number of GCTM2⁺/CD9⁺ cells each week per well of a 12-well plate. Graphs of mean + SEM from three independent experiments. Differences at week two (wk2) were significant by ANOVA with a posttest for linear trend ($*P < 0.05$, $***P < 0.001$). (D) Representative qRT-PCR of stem cell pluripotency-associated transcripts. Graphs of mean + SEM of experimental replicates. (E) Representative flow cytometric plots of GCTM2 and CD9 coexpression for hESCs cultured continuously with 2.5 μ M XAV for 6 wk. For C and D: concentrations of Wnt3a CM tested were 12.5, 25, and 50%, with LCM added to yield 50% total CM; XAV concentrations tested were 0.2 μ M and 2.5 μ M in 50% Wnt3A CM. (F) Graph showing the total number of GCTM2⁺/CD9⁺ cells per well of a 12-well plate after 8 wk of continual exposure to 50% L or Wnt3A CM, DMSO (vehicle control), or 2.5 μ M XAV. Graphs of mean + SEM from two independent experiments.

Wnt3A or with the GSK3- β inhibitor, BIO, and found that these treatments led to similar results as Wnt3A CM (Fig. S14).

We hypothesized that if Wnt3A CM promotes loss of hESC maintenance through Wnt/ β -catenin signaling, then we should be able to block this effect using downstream inhibitors of the pathway. XAV939 (XAV) is a Tankyrase inhibitor that effectively antagonizes Wnt/ β -catenin signaling downstream of receptor activation by stabilizing levels of Axin, a negative regulator of β -catenin (Fig. S2) (24). We found that the ability of Wnt3A CM to promote loss of maintenance of hESCs was blocked by coincubating cells with XAV in a dose-dependent manner (Fig. 1A–C). This observation suggests that the effects of Wnt3A CM are due specifically to Wnt/ β -catenin signaling and not to other components of the CM. Down-regulation of *POU5F1* and *NANOG* transcripts was also inhibited by XAV (Fig. 1D). Collectively, these experiments demonstrate that activating Wnt/ β -catenin signaling leads to loss of hESC maintenance under conditions that are permissive for self-renewal.

Endogenous Wnt/ β -Catenin Signaling Is Not Required for Self-Renewal of hESCs. We next investigated the effects of long-term inhibition of Wnt/ β -catenin signaling in hESCs. We cultured hESCs with 2.5 μ M XAV for 8 wk and found no significant difference from hESCs cultured in standard hESC medium (KSR)

on MEFs (Fig. 1E and F). The weekly split ratio for XAV-cultured hESCs was stable and the hESCs remain phenotypically undifferentiated (>90% GCTM2⁺/CD9⁺, indistinguishable from controls; Fig. 1E). Transcripts for *POU5F1* and *NANOG* are equal or higher in XAV- versus vehicle-treated hESCs (Fig. 1D). These observations show that endogenous Wnt/ β -catenin signaling is dispensable for hESC self-renewal.

Wnt/ β -Catenin Signaling Drives Mesoderm Lineage Differentiation of hESCs. Our observation that cell morphologies change in the presence of exogenous Wnt3A (Fig. 1A) suggested that Wnt/ β -catenin signaling promotes differentiation of hESCs. To investigate this directly we asked whether Wnt/ β -catenin signaling promotes changes in expression of a panel of lineage-specific markers assessed by qRT-PCR. We found that Wnt3A leads to elevation of transcripts associated with early mesoderm, endoderm, and primitive streak cell fates (Fig. 2A). Comparable results are observed following treatment of hESCs with either recombinant Wnt3A protein or with Wnt3A CM (Fig. S3). As a control we showed that XAV blocks induction of mesoderm and primitive streak transcripts in hESCs treated with Wnt3A CM and reduces levels of endoderm transcripts (Fig. 2A). Interestingly, serum alone, without adding exogenous Wnt, also induces transcripts associated with multilineage differentiation.

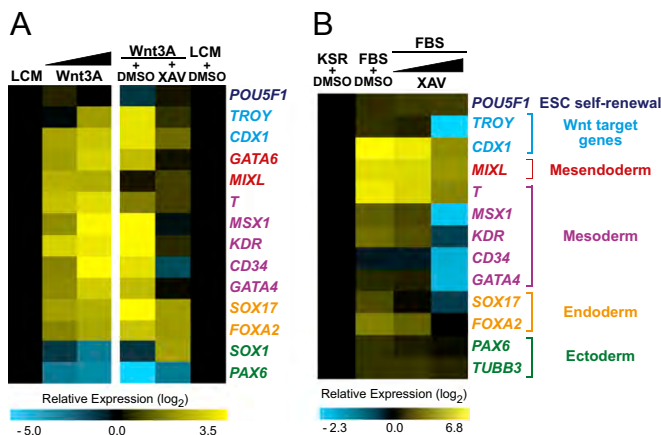


Fig. 2. Wnt3A induces lineage-specific transcripts of differentiation. (A) Heat maps of qRT-PCR results from H1 cells cultured for 6 d on MEFs in KSR media plus the conditions listed: LCM (50%), Wnt3A CM (Left, 12.5 and 50%; Right, 50%), and XAV (2.5 μ M). Wnt3A leads to increased transcripts associated with mesoderm and endoderm lineages in a dose-dependent manner (Left). Transcriptional changes resulting from Wnt3A treatment are blocked by coadministration of XAV (Right). (B) Medium containing 20% FBS also induces transcripts associated with multilineage differentiation. Inhibition of β -catenin signaling in serum leads to a dose-dependent reduction in mesoderm and endoderm transcripts. XAV concentrations, 0.2 μ M and 2.5 μ M. Representative data are shown from one experiment.

We found that inhibition of β -catenin signaling via XAV is also sufficient to block serum-induced mesoderm transcripts in a dose-dependent manner (Fig. 2B). Taken together, these results suggest that Wnt/ β -catenin signaling drives transcriptional changes indicative of mesoderm lineage differentiation of hESCs. This finding is in agreement with previous publications suggesting a role for Wnt in differentiation rather than self-renewal of hESCs (18, 19, 22).

Endogenous Wnt/ β -Catenin Signaling Is Inactive in Undifferentiated hESCs and Active in Differentiating hESCs. To monitor β -catenin/TCF signaling in live cells, we generated multiple hESC lines stably transduced with a fluorescence-based β -catenin activated reporter (BAR-VENUS; Fig. 3A). Remarkably, hESCs stably transduced with the BAR reporter have low/undetectable levels of β -catenin signaling in mostly undifferentiated colonies, whereas endogenous BAR activity is observed primarily in cases of morphological differentiation (Fig. 3B). The levels of VENUS in undifferentiated hESCs were similar to those produced by a control reporter that contained mutant TCF-binding sites, denoted as found unresponsive BAR (FUBAR) (25). Moreover, we found that *CTNNT1* (β -catenin) siRNA transfection did not significantly reduce basal levels of VENUS expression in undifferentiated hESCs (Fig. 3C). This result suggests that endogenous Wnt/ β -catenin signaling is less active in undifferentiated hESCs during self-renewal.

Heterogeneous Activation of Wnt/ β -Catenin Signaling in Response to Pathway Agonists Reflects Intrinsic Differences in hESCs. To confirm that BAR could be activated, we stimulated hESCs with exogenous Wnt3A or the GSK3 inhibitor, CHIR99021 (CHIR). We also confirmed that β -catenin protein levels were stabilized, as expected, with pathway agonists (Fig. S4). We observed a heterogeneous pattern of VENUS expression both within and between colonies of H1-BARV hESCs exposed to pathway agonists, even though expression of the Ubiquitin-DsRED portion of the integrated construct was strongly maintained in all colonies (Fig. 3D and E). We then tested whether heterogeneity observed with Wnt-induced VENUS expression was due to differences in the intrinsic ability of the cells to respond to Wnt signaling or due to transient silencing of the BAR-VENUS portion of the integrated

reporter. Specifically, H1-BAR-VENUS cells were stimulated with Wnt3A CM for 72 h to induce VENUS expression, then FACS-sorted cells into VENUS-negative, -low, and -high subpopulations for transcriptional analysis. In this context, the VENUS-negative cells had been exposed to the same Wnt3A signal as the VENUS-positive cells. If VENUS-negative cells have silenced the VENUS reporter but actively signal through β -catenin, then we would expect their transcriptional response to be equivalent to VENUS-positive cells. Instead, we found that VENUS-negative cells have a much lower Wnt transcriptional signature versus VENUS-positive cells (Fig. 3F), suggesting that these cells in fact have low levels of β -catenin signaling. Compared with control LCM-treated hESCs, Wnt-treated VENUS-negative hESCs express similar or lower levels of transcripts for Wnt/ β -catenin target genes, as well as mesoderm and endoderm lineages (Fig. 3F). Furthermore, VENUS-high cells express higher levels of Wnt3A-induced transcripts compared with VENUS-low cells, indicating that the fluorescent intensity of our BAR-VENUS reporter correlates with quantitative transcriptional measures of Wnt/ β -catenin signaling. These results confirm that the heterogeneous reporter response observed in BAR-VENUS cells reflects genuine transcriptional differences in levels of Wnt/ β -catenin signaling in cultures of hESCs.

Interestingly, we observe that Wnt-induced reporter expression is reversible if VENUS-positive hESCs are replated back into self-renewal conditions without Wnt (Fig. S5). hESCs treated with Wnt3A CM for 1 wk, then replated in KSR media without Wnt for another week also express an undifferentiated phenotype, comparable to controls (Fig. S5).

hESCs Exhibit a Delay in Activating Wnt/ β -Catenin Signaling Compared with Nonpluripotent Cells. When we examined the time frame of VENUS expression in hESCs following stimulation with Wnt3A, we found that it takes at least 3 d to detect robust and statistically significant increases in the percentage of VENUS-positive cells above control LCM-treated cells (Fig. 3G). We also observed consistent results regarding the kinetics of Wnt3A-induced reporter activation using H1-BAR-Luciferase (H1-BAR-Luc) cells. In comparison with nonpluripotent cells, hESCs require longer to activate the BAR-Luciferase reporter following stimulation with Wnt3A (72 h for hESCs versus 18 h for nonpluripotent HEK293T, RKO, and A375 cells; Fig. 3H). These observations are consistent with the hypothesis that undifferentiated hESCs are refractory to Wnt/ β -catenin signaling due to active repression of the pathway and that the delay in reporter response reflects the gradual alleviation of this repression.

OCT4 Functionally Represses Wnt/ β -Catenin Signaling in Undifferentiated hESCs. A key stem cell pluripotency factor, OCT4, has been previously reported to regulate levels of β -catenin (26). Thus, we examined whether OCT4 functionally regulates Wnt/ β -catenin signaling in hESCs by carrying out LOF experiments with siRNAs. Interestingly, transient knockdown of *POU5F1* (OCT4) results in activation of the BAR reporter (Fig. 4A) and stabilization of β -catenin protein levels (Fig. S4) in hESCs independent of exogenous Wnt. Two of our *POU5F1* siRNAs (*POU5F1-A* and *-B*) achieved complete OCT4 knockdown in $\geq 90\%$ of hESCs (Fig. 4B and C), whereas one *POU5F1* siRNA sequence (*POU5F1-C*) was less efficient at knocking down OCT4 protein (Fig. 4B and D). Levels of reporter activation resulting from OCT4 knockdown with *POU5F1-A* and *-B* were statistically significant compared with control siRNA and similar to, or higher than, that achieved by knockdown of *AXIN1* and *AXIN2*, known negative regulators of β -catenin. BAR-VENUS expression could be blocked by cotransfection of *CTNNT1* siRNA with *POU5F1* siRNA, indicating that β -catenin is required for reporter activation in cells depleted of OCT4.

Although reduced OCT4 expression will eventually lead to differentiation of hESCs (27), at 72 h post-siRNA transfection OCT4-negative hESCs are still positive for other stem cell markers, GCTM2 and CD9 (Fig. 4C). This combination of cell

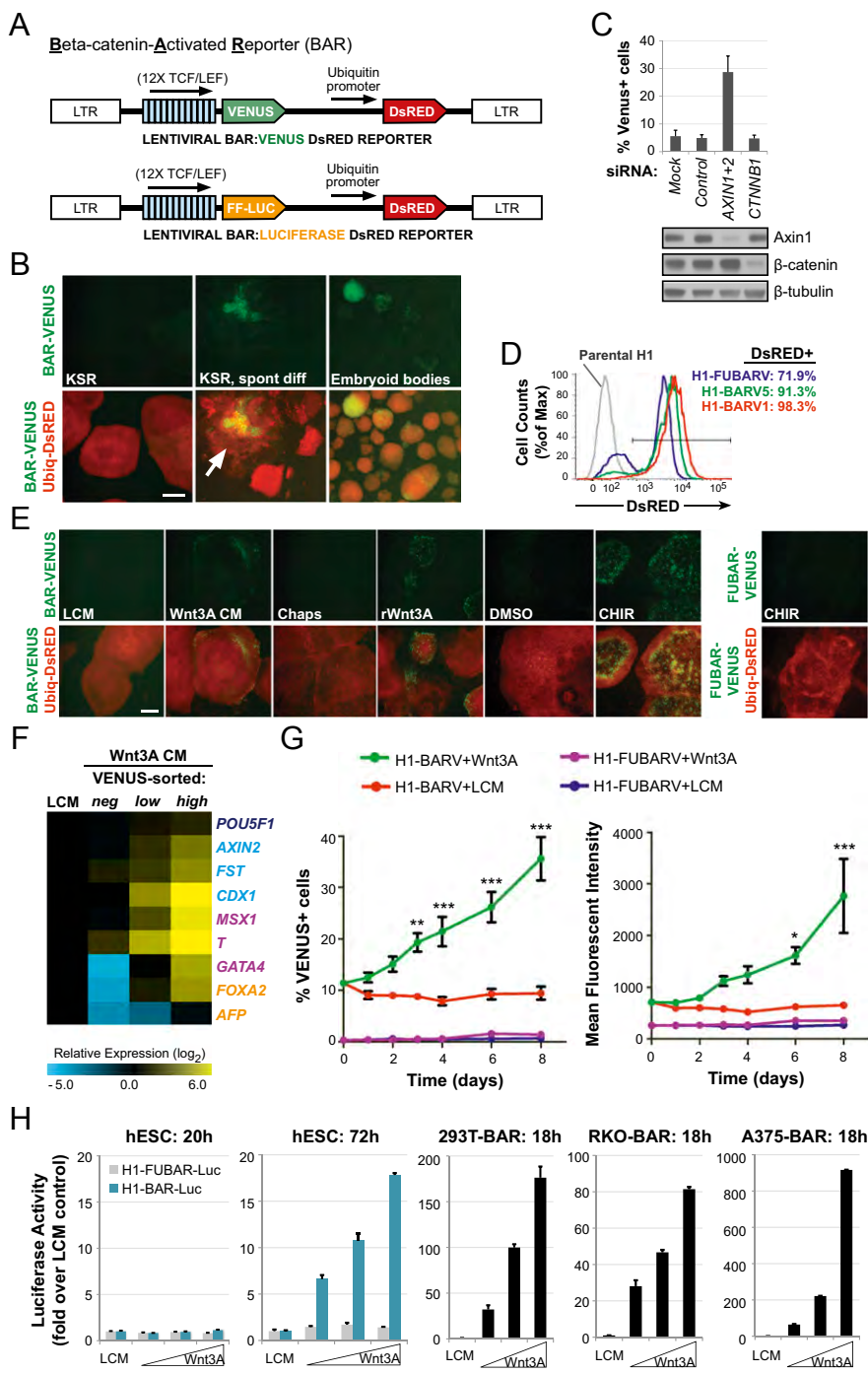


Fig. 3. β -catenin reporter hESCs. (A) Schematic of the BAR lentiviral vector used to generate stable H1-BAR-Venus (BARV) and H1-BAR-Luciferase (BAR-Luc) cell lines. The construct contains 12x TCF binding sites upstream of a minimal promoter driving VENUS fluorescent protein or Firefly Luciferase, followed by a Ubiquitin promoter driving DsRED fluorescent protein. (B) Undifferentiated H1-BARV cells exhibit low/absent endogenous reporter activity when cultured on MEFs in KSR medium. Endogenous VENUS expression is observed under various contexts of differentiation (spont diff, spontaneous differentiated colony, marked with an arrow). (Scale bar, 400 μ m.) (C) H1-BARV cells show no significant reduction in VENUS expression versus control at 72 h posttransfection with *CTNNB1* siRNA. *AXIN1+2* siRNAs serve as a positive control. Graph of mean \pm SEM of three independent experiments. (D) After mechanical selection of DsRED-positive cells, H1-BARV lines are $\geq 90\%$ DsRED⁺. (E) hESCs respond to Wnt pathway stimuli heterogeneously, both within and between colonies. H1-FUBARV cells containing mutated TCF-binding sites are unresponsive to CHIR. (L or Wnt3A CM, 50%; 1% Chaps is the vehicle control for rWnt3A; rWnt3A, 500 ng/mL recombinant Wnt3A; DMSO is the vehicle control for CHIR; CHIR, 6 μ M). (Scale bar, 400 μ m.) (F) 72 h Wnt3A-treated hESCs were sorted on the basis of VENUS expression into negative-, low-, and high-expressing subpopulations, then analyzed by qRT-PCR. Results from a representative experiment are shown. Data show that reporter heterogeneity in response to Wnt reflects transcriptional differences indicative of true variations in levels of β -catenin signaling. (G) Reporter activity, as measured by percent of VENUS-positive cells (Left) and mean fluorescent intensity of these cells (Right), over time of Wnt3A treatment (50% CM). Graph of mean \pm SEM from three independent experiments. Reporter response following Wnt3A treatment was significantly different from the control treatment by two-way ANOVA with Bonferroni posttest ($*P < 0.05$, $**P < 0.01$, $***P < 0.001$). H1-FUBARV cells containing mutated TCF-binding sites are unresponsive to Wnt3A. (H) Luciferase reporter assay results from stable BAR-Luciferase transduced hESCs and nonpluripotent cell lines stimulated with control LCM or increasing concentrations of Wnt3A CM for the period (hours) noted for each graph.

surface markers was chosen because coexpression of GCM2 and CD9 is reported to correlate with OCT4 protein coexpression, increased levels of pluripotency transcripts, and decreased levels of lineage-specific transcripts in hESCs (28). Therefore, activation of the BAR reporter by *POU5F1* knock-down at this time point is unlikely to be due to overt differentiation. Interestingly, when we treat hESCs with the inefficient *POU5F1* siRNA (*POU5F1-C*), which results in a mixed population of OCT4-positive and OCT4-negative cells, we observe that all of the VENUS expression lies within the OCT4-negative subpopulation (Fig. 4D). These experiments further support the hypothesis that OCT4 functionally represses Wnt/ β -catenin signaling in hESCs.

We next investigated whether OCT4 gain-of-function can repress Wnt/ β -catenin signaling in nonpluripotent cells. Indeed, transient expression of OCT4 in HEK293T cells inhibits BAR reporter activity induced by Wnt3A CM (Fig. 4E), consistent with other reports (26, 29). OCT4 and NANOG are known to regulate each others' promoters (30–32). Not surprisingly, we found that knockdown of *POU5F1* in hESCs results in concurrent decrease of NANOG protein and vice versa (Fig. S6). Thus, we also examined whether NANOG contributes to Wnt/ β -catenin repression in HEK293T cells. Our results indicate that expression of NANOG had no significant effect on Wnt-induced BAR reporter activity, alone or in combination with OCT4, implying that OCT4-mediated repression of Wnt/ β -catenin signaling does not require NANOG (Fig. 4F).

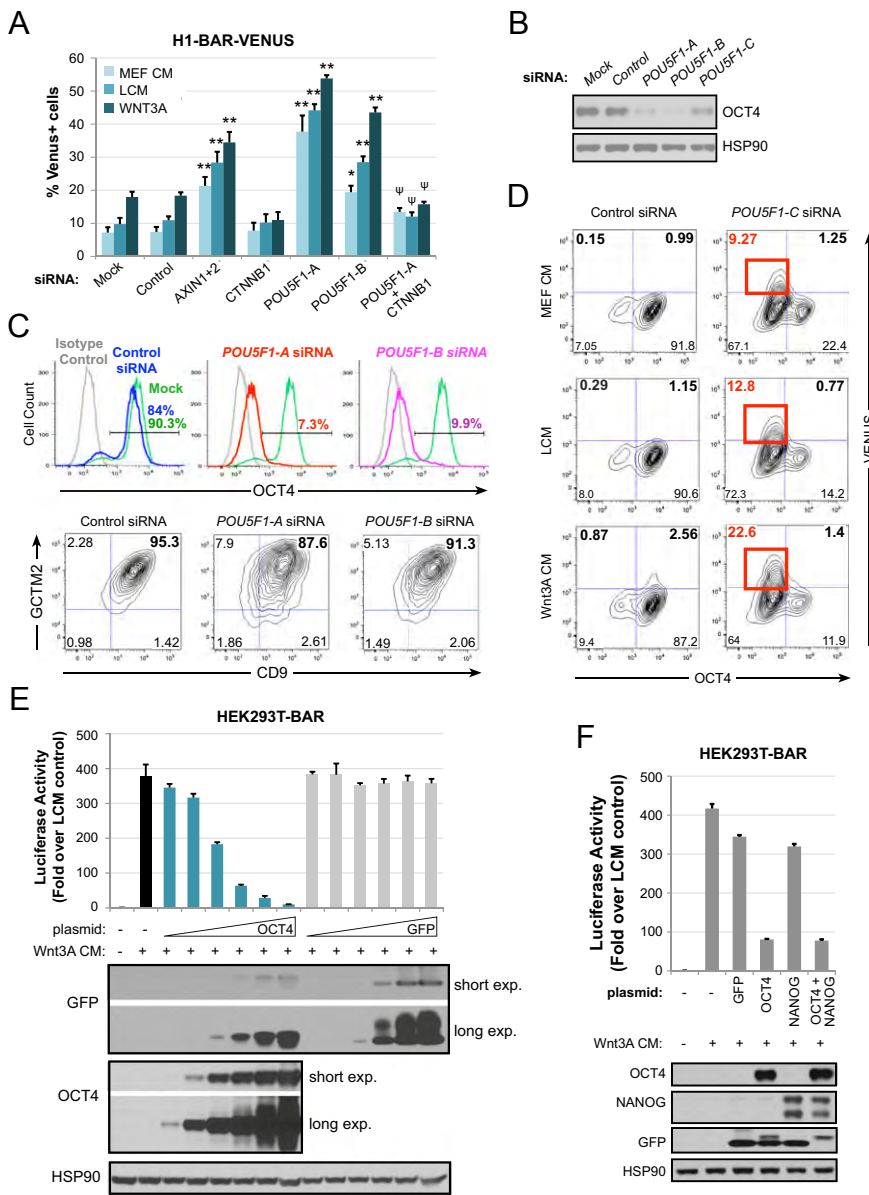


Fig. 4. Oct4 functionally represses β -catenin/TCF signaling in hESCs. (A) H1-BAR-VENUS cells transfected with *POU5F1* siRNA activate the reporter. BAR reporter response for both *POU5F1* siRNAs was significantly different from control siRNA by two-way ANOVA with Bonferroni posttest ($*P < 0.01$, $**P < 0.001$). *CTNNB1* in combination with *POU5F1-A* siRNA significantly blocks reporter activation induced by *POU5F1-A* siRNA alone ($^{\psi}P < 0.001$). Graph of mean \pm SEM from three independent experiments analyzed at 72 h post-siRNA transfection with 24 h stimulation with 50% L or Wnt3A CM in MEF CM. (B) Western blots validating that *POU5F1* siRNAs lead to targeted knockdown of OCT4 protein in hESCs at 72 h posttransfection. (C) Flow plots showing OCT4 (Upper), CGTM2, and CD9 labeling (Lower) of siRNA-transfected H1-BAR-VENUS cells. (D) Flow plots showing expression of VENUS and OCT4 in H1-BAR-VENUS cells. Red boxes indicate OCT4⁻/VENUS⁺ subpopulation. (E) Graph of HEK293T cells transiently transfected with pBAR-Luciferase reporter and increasing concentrations of GFP or OCT4 expression plasmids, then stimulated overnight with Wnt3A CM. Bars denote SEM from experimental replicates. Western blots confirm that the protein of interest was expressed for each sample. The Oct4 plasmid contained GFP and Oct4 connected by a 2A-linker peptide, previously described (38). (F) Graph of HEK293T cells transiently transfected with pBAR-Luciferase reporter and expression plasmids noted, then stimulated overnight with Wnt3A CM. Bars denote SEM from experimental replicates. Western blots confirm that proteins of interest were expressed for each sample.

Discussion

One explanation for variations in the effects of Wnt/ β -catenin activation in hESCs observed in different studies may involve the dose and duration of Wnt stimulus. The fact that Wnt3A required more than 1 wk to significantly diminish self-renewal of hESCs in the present study may explain why other studies that used short-term assays did not observe the same effect. We also tested multiple doses of Wnt3A and XAV to confirm effects were dose dependent versus studies that used a single dose of Wnt3A. Interestingly, similar to Bone et al. (18), we found that the concentration of BIO published to maintain hESCs (2 μ M) (7) was not sufficient to robustly activate the β -catenin reporter in the absence of exogenous Wnt (Fig. S1B). hESC maintenance was diminished to a level similar to that observed with Wnt3A when cells were cultured with a higher, reporter-activating concentration of BIO (4 μ M) for 3 wk (Fig. S14). Similarly, we found that concentrations of recombinant Wnt3A that activated the BAR reporter lead to loss of hESC maintenance, whereas lower concentrations that did not robustly activate the reporter had no effect on maintenance (Fig. S1A and C).

Although other studies have concluded that Wnt/ β -catenin signaling is active in hESCs due to nuclear β -catenin immunostaining, subcellular localization of β -catenin in undifferentiated versus differentiated hESCs is inconsistent between studies (7, 20). Moreover, steady-state levels of nuclear β -catenin do not always correlate with TCF-mediated transcriptional activity (33), and the ability of β -catenin to facilitate transcriptional activation with TCF may also be modulated by other interacting proteins, such as ICAT for example (34). Therefore, our study used detection of β -catenin/TCF transcriptional activity to monitor whether Wnt/ β -catenin signaling was active in live hESCs. Whereas negligible endogenous β -catenin signaling was observed in undifferentiated hESCs, endogenous signaling was subsequently elevated in hESCs undergoing differentiation. Our demonstration that hESCs can be sorted on the basis of a fluorescent β -catenin/TCF transcriptional reporter provides a platform by which cells can be sorted on the basis of live signaling activity, thereby allowing for more precise interrogation of Wnt/ β -catenin signaling in a variety of downstream applications.

Regarding the heterogeneity observed in β -catenin reporter hESCs in response to exogenous Wnt3a, we cannot exclude the possibility that some hESCs may be more primed for differenti-

ation and this may account for differences in their sensitivity to Wnt3a. Indeed, such heterogeneity has been previously reported in hESC cultures (35). However, Wnt-induced reporter expression is reversible if the exogenous Wnt3a is withdrawn, and after withdrawal the hESCs retain an undifferentiated phenotype and self-renew, suggesting that VENUS-positive cells are not irreversibly committed to differentiate under these conditions.

Although Wnt/ β -catenin signaling has been implicated in promoting self-renewal of hESCs (7), several studies have found β -catenin pathway activation transiently enhances hESC proliferation and/or self-renewal, but ultimately fails to maintain hESCs after multiple passages (9, 20–23). Our study calls for a revised interpretation of the role of Wnt/ β -catenin signaling in hESCs and supports a primary role for Wnt/ β -catenin signaling in the differentiation, rather than self-renewal, of hESCs *in vitro*. The long-term expansion achieved with sustained inhibition of the pathway suggests that endogenous Wnt/ β -catenin signaling is in fact not required for the self-renewal of undifferentiated hESCs. Furthermore, activating β -catenin signaling leads to induction of mesoderm lineage transcripts and an eventual loss of self-renewal after several passages. Given that activation of the Wnt pathway leads to loss of hESC self-renewal, we speculate that intrinsic inhibition of β -catenin/TCF signaling may actually be critical for the maintenance of undifferentiated hESCs. In support of this theory, we also find that Oct4, a key pluripotency factor highly expressed in hESCs, functionally represses endogenous Wnt/ β -catenin signaling in self-renewing hESCs. Taken

together, our results support a model whereby Wnt/ β -catenin signaling is repressed by Oct4 in the context of self-renewing hESCs and is derepressed when hESCs differentiate.

Materials and Methods

hESC Culture. H1 hESCs were cultured on irradiated MEF feeders (2.5×10^4 MEF/cm²) in 20% (vol/vol) knockout serum replacement medium + 8 ng/mL basic (b)FGF (36). Colonies were passaged ~1:12 weekly as small clusters using dispase (1.75 units/mL; Invitrogen). This split ratio corresponds to 30,000–50,000 hESCs per centimeter squared. MEF carryover was minimized during passage by gravity settling hESC clusters in a conical tube, and then aspirating the medium above the settled pellet before seeding hESCs. For feeder-free experiments, hESCs were seeded onto matrigel (Invitrogen; coated at 35 μ g/cm²) and cultured in KSR medium + 4 ng/mL bFGF conditioned overnight on irradiated MEFs (6×10^4 MEF/cm²) (hereby referred to as MEF CM). MEF CM was sterile filtered and freshly supplemented with 8 ng/mL bFGF before use. All hESC lines used for this study were confirmed to be karyotypically normal and mycoplasma-free. For manual selection of hESC, see Fig. S7.

Additional experimental procedures are provided in *SI Materials and Methods* and *Table S1*.

ACKNOWLEDGMENTS. We thank Mick Bhatia for the pMIN-Ub-DsRED-WPRE construct (37). This work was supported by the National Institutes of Health (NIH) Grants 1P01-GM081619 and NIH U01 vHL100395 and T.L.B. is funded in part through NIH/National Institute of Arthritis and Musculoskeletal and Skin Diseases Training Grant T32AR056969. R.T.M. is an Investigator of the Howard Hughes Medical Institute.

- Brons IG, et al. (2007) Derivation of pluripotent epiblast stem cells from mammalian embryos. *Nature* 448:191–195.
- Tesar PJ, et al. (2007) New cell lines from mouse epiblast share defining features with human embryonic stem cells. *Nature* 448:196–199.
- Kohn AD, Moon RT (2005) Wnt and calcium signaling: Beta-catenin-independent pathways. *Cell Calcium* 38:439–446.
- Clevers H (2006) Wnt/ β -catenin signaling in development and disease. *Cell* 127:469–480.
- Moon RT (2005) Wnt/ β -catenin pathway. *Sci STKE* 2005:cm1.
- Hao J, Li TG, Qi X, Zhao DF, Zhao GQ (2006) WNT/ β -catenin pathway up-regulates Stat3 and converges on LIF to prevent differentiation of mouse embryonic stem cells. *Dev Biol* 290:81–91.
- Sato N, Meijer L, Skaltsounis L, Greengard P, Brivanlou AH (2004) Maintenance of pluripotency in human and mouse embryonic stem cells through activation of Wnt signaling by a pharmacological GSK-3-specific inhibitor. *Nat Med* 10:55–63.
- Miyabayashi T, et al. (2007) Wnt/ β -catenin/CBP signaling maintains long-term murine embryonic stem cell pluripotency. *Proc Natl Acad Sci USA* 104:5668–5673.
- Singla DK, Schneider DJ, LeWinter MM, Sobel BE (2006) wnt3a but not wnt11 supports self-renewal of embryonic stem cells. *Biochem Biophys Res Commun* 345:789–795.
- Berge DT, et al. (2011) Embryonic stem cells require Wnt proteins to prevent differentiation to epiblast stem cells. *Nat Cell Biol* 13:1070–1075.
- Ogawa K, Nishinakamura R, Iwamoto Y, Shimozato D, Niwa H (2006) Synergistic action of Wnt and LIF in maintaining pluripotency of mouse ES cells. *Biochem Biophys Res Commun* 343:159–166.
- Takao Y, Yokota T, Koide H (2007) Beta-catenin up-regulates Nanog expression through interaction with Oct-3/4 in embryonic stem cells. *Biochem Biophys Res Commun* 353:699–705.
- Wagner RT, Xu X, Yi F, Merrill BJ, Cooney AJ (2010) Canonical Wnt/ β -catenin regulation of liver receptor homolog-1 mediates pluripotency gene expression. *Stem Cells* 28:1794–1804.
- Marson A, et al. (2008) Wnt signaling promotes reprogramming of somatic cells to pluripotency. *Cell Stem Cell* 3:132–135.
- Lluis F, Pedone E, Pepe S, Cosma MP (2008) Periodic activation of Wnt/ β -catenin signaling enhances somatic cell reprogramming mediated by cell fusion. *Cell Stem Cell* 3:493–507.
- Lyashenko N, et al. (2011) Differential requirement for the dual functions of β -catenin in embryonic stem cell self-renewal and germ layer formation. *Nat Cell Biol* 13:753–761.
- Soncin F, et al. (2009) Abrogation of E-cadherin-mediated cell-cell contact in mouse embryonic stem cells results in reversible LIF-independent self-renewal. *Stem Cells* 27:2069–2080.
- Bone HK, Nelson AS, Goldring CE, Tosh D, Welham MJ (2011) A novel chemically directed route for the generation of definitive endoderm from human embryonic stem cells based on inhibition of GSK-3. *J Cell Sci* 124:1992–2000.
- Nakanishi M, et al. (2009) Directed induction of anterior and posterior primitive streak by Wnt from embryonic stem cells cultured in a chemically defined serum-free medium. *FASEB J* 23:114–122.
- Ullmann U, et al. (2008) GSK-3-specific inhibitor-supplemented hESC medium prevents the epithelial-mesenchymal transition process and the up-regulation of matrix metalloproteinases in hESCs cultured in feeder-free conditions. *Mol Hum Reprod* 14:169–179.
- Hasegawa K, Fujioka T, Nakamura Y, Nakatsuji N, Suemori H (2006) A method for the selection of human embryonic stem cell sublines with high replating efficiency after single-cell dissociation. *Stem Cells* 24:2649–2660.
- Dravid G, et al. (2005) Defining the role of Wnt/ β -catenin signaling in the survival, proliferation, and self-renewal of human embryonic stem cells. *Stem Cells* 23:1489–1501.
- Cai L, et al. (2007) Promoting human embryonic stem cell renewal or differentiation by modulating Wnt signal and culture conditions. *Cell Res* 17:62–72.
- Huang SM, et al. (2009) Tankyrase inhibition stabilizes axin and antagonizes Wnt signalling. *Nature* 461:614–620.
- Biechele TL, Moon RT (2008) Assaying beta-catenin/TCF transcription with beta-catenin/TCF transcription-based reporter constructs. *Methods Mol Biol* 468:99–110.
- Abu-Remaileh M, et al. (2010) Oct-3/4 regulates stem cell identity and cell fate decisions by modulating Wnt/ β -catenin signalling. *EMBO J* 29:3236–3248.
- Zafarana G, Avery SR, Moore HD, Andrews PW (2009) Specific knockdown of OCT4 in human embryonic stem cells by inducible short hairpin RNA interference. *Stem Cells* 27:776–782.
- Laslett AL, et al. (2007) Transcriptional analysis of early lineage commitment in human embryonic stem cells. *BMC Dev Biol* 7:12.
- Anton R, Kestler HA, Kühl M (2007) Beta-catenin signaling contributes to stemness and regulates early differentiation in murine embryonic stem cells. *FEBS Lett* 581:5247–5254.
- Loh YH, et al. (2006) The Oct4 and Nanog transcription network regulates pluripotency in mouse embryonic stem cells. *Nat Genet* 38:431–440.
- Pan G, Thomson JA (2007) Nanog and transcriptional networks in embryonic stem cell pluripotency. *Cell Res* 17:42–49.
- Rodda DJ, et al. (2005) Transcriptional regulation of nanog by OCT4 and SOX2. *J Biol Chem* 280:24731–24737.
- Rosin-Arbesfeld R, Cliffe A, Brabletz T, Bienz M (2003) Nuclear export of the APC tumour suppressor controls beta-catenin function in transcription. *EMBO J* 22:1101–1113.
- Daniels DL, Weis WI (2002) ICAT inhibits beta-catenin binding to Tcf/Lef-family transcription factors and the general coactivator p300 using independent structural modules. *Mol Cell* 10:573–584.
- Hough SR, Laslett AL, Grimmond SB, Kolle G, Pera MF (2009) A continuum of cell states spans pluripotency and lineage commitment in human embryonic stem cells. *PLoS ONE* 4:e7708.
- Amit M, et al. (2000) Clonally derived human embryonic stem cell lines maintain pluripotency and proliferative potential for prolonged periods of culture. *Dev Biol* 227:271–278.
- Stewart MH, et al. (2006) Clonal isolation of hESCs reveals heterogeneity within the pluripotent stem cell compartment. *Nat Methods* 3:807–815.
- Papapetrou EP, et al. (2009) Stoichiometric and temporal requirements of Oct4, Sox2, Klf4, and c-Myc expression for efficient human iPSC induction and differentiation. *Proc Natl Acad Sci USA* 106:12759–12764.

DEFINE YOUR FLOW



Own the direction of your research with the trailblazing ZE5™ Cell Analyzer

30-parameter analysis, unmatched sample flexibility, and easy to learn and use Everest™ Software now give both novice and expert users the power to set their own pace for discovery.

Visit us at bio-rad.com/info/DefineYourFlow

BIO-RAD

Single Adult Kidney Stem/Progenitor Cells Reconstitute Three-Dimensional Nephron Structures In Vitro

SHINJI KITAMURA,^a HIROYUKI SAKURAI,^b HIROFUMI MAKINO^a

Key Words. Adult kidney tissue stem cells • Three-dimensional nephron structures in vitro • Organogenesis

^aDepartment of Medicine and Clinical Science, Okayama University Graduate School of Medicine, Dentistry and Pharmaceutical Sciences, Okayama-shi, Okayama, Japan; ^bDepartment of Pharmacology and Toxicology, Kyorin University School of Medicine, Mitaka-shi, Tokyo, Japan

Correspondence: Shinji Kitamura, Ph.D., M.D., Department of Medicine and Clinical Science, Okayama University Graduate School of Medicine, Dentistry, and Pharmaceutical Sciences, 2-5-1 Shikata-cho, Okayama 700-8558, Japan. Telephone: 81-86-235-7235; Fax: 81-86-222-5214; e-mail: s-kita@md.okayama-u.ac.jp

Received August 1, 2014; accepted for publication October 2, 2014; first published online in *STEM CELLS EXPRESS* November 25, 2014.

© AlphaMed Press
1066-5099/2014/\$30.00/0

<http://dx.doi.org/10.1002/stem.1891>

ABSTRACT

The kidneys are formed during development from two distinct primordial tissues, the metanephric mesenchyme and the ureteric bud. The metanephric mesenchyme develops into the kidney nephron, the minimal functional unit of the kidney. A nephron consists of several segments and regulates water, electrolyte, and acid-base homeostasis in addition to secreting certain hormones. It has been predicted that the kidney will be among the last organs successfully regenerated in vitro due to its complex structure and multiple functions. Here, we show that adult kidney stem/progenitor cells (KS cells), derived from the S3 segment of adult rat kidney nephrons, can reconstitute a three-dimensional kidney-like structure in vitro. Kidney-like structures were formed when a cluster of KS cells was suspended in an extracellular matrix gel and cultured in the presence of several growth factors. Morphological analyses revealed that these kidney-like structures contained every substructure of the kidney, including glomeruli, proximal tubules, the loop of Henle, distal tubules, and collecting ducts, but no vasculature. Our results demonstrate that a cluster of tissue stem/progenitor cells has the ability to reconstitute the minimum unit of its organ of origin by differentiating into specialized cells in the correct location. This process differs from embryonic kidney development, which requires the mutual induction of two different populations of progenitors, metanephric mesenchymal cells and ureteric bud cells. *STEM CELLS* 2015;33:774–784

INTRODUCTION

In the embryo, the kidney develops from two primordial cell types, metanephric mesenchymal cells and ureteric bud cells. These cells differentiate into more than a dozen distinct mature cell types in the kidney. The minimum unit of the kidney, the nephron, is composed of well-defined segments: the glomerulus, the proximal tubule (S1, PCT, S2 and S3), the loop of Henle, the distal tubule, and the collecting duct (Fig. 1A) [1]. Because of this complicated structure, it is believed that the kidney will be among the last organs successfully regenerated in vitro.

Despite the challenge, a few attempts have been reported to aim (re)construction of the kidney. For example, glial cell line-derived neurotrophic factor (GDNF)-overexpressing human mesenchymal stem cells differentiate into nephron structure when they are injected near the ureteric bud of rat embryo [2]. This report “borrowed” the in vivo kidney organogenesis machinery. Recently, acellular kidney extracellular matrixes have been shown to serve as scaffolds for the functional new kidney [3], suggesting the importance of the three-

dimensional structure of the kidney. Another group has tried to develop three-dimensional branching tubular structures from the embryonic ureteric bud or its primordial tissue, Wolffian duct, and let the structures induce freshly isolated metanephric mesenchyme cells to form nephron [4]. Their “neo-kidneys” attract host blood vessels toward them when they are transplanted into the kidney capsule.

In addition to these tissue engineering approaches, some groups have attempted to differentiate pluripotent stem cells into the kidney [5, 6]. A major problem of using such pluripotent stem cells is that undifferentiated cells may form ectopic tumors. In this regard, tissue stem cells are thought to be ideal source for kidney regeneration. Recently, Taguchi et al. [7] has succeeded in pinpointing nephron progenitors in mouse embryo and has established an efficient induction method for embryonic stem cells (ESCs) to become nephron progenitors. Since Six2-positive embryonic nephron progenitor cells are reported to be absent in the adult kidney [8], several other candidate cells for adult tissue stem cells have been proposed [9–11].

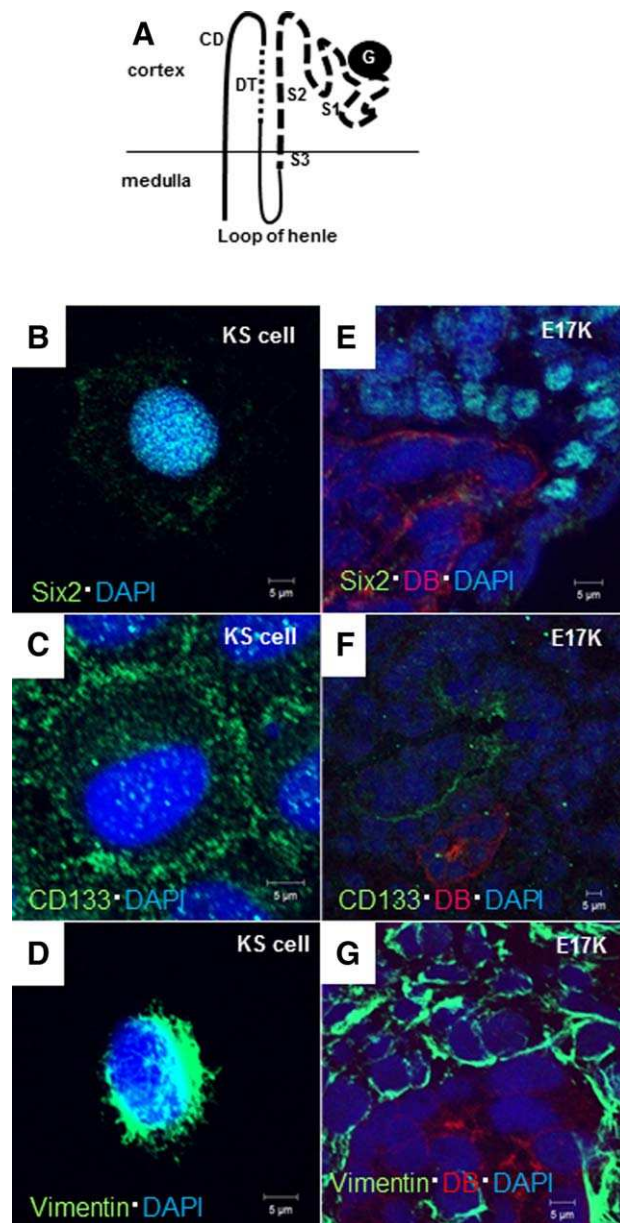


Figure 1. Kidney tissue stem cell-like characteristics of KS cells. **(A):** Nephron structure: G; proximal tubule, S1, PCT, S2, S3 and loop of Henle; DT; CD. **(B–G):** Characteristics of KS cells compared to 17-day-old embryonic rat kidneys (E17K). **(B):** Green, Six2; blue, DAPI. **(C):** Green, CD133; blue, DAPI. **(D):** Green, Vimentin; blue, DAPI. Compared to 17-day-old embryonic rat kidneys. **(E):** Green, Six2; red, *Dolichos biflorus* agglutinin, blue, DAPI. **(F):** Green, CD133; red, *Dolichos biflorus* agglutinin, blue, DAPI. **(G):** Green, Vimentin; red, *Dolichos biflorus* agglutinin, blue, DAPI. Representative cell staining photomicrographs from four to five independent experiments and embryonic kidney staining photomicrographs from two to three independent experiments. Scale bar = 5 μm . Abbreviations: CD, collecting duct; DT, distal tubule; G, glomerulus; KS cell, kidney stem/progenitor cell.

We previously established kidney stem/progenitor cells (KS cells) from adult kidney in an attempt to find a cell that has very high proliferating capacity [12] and demonstrated that these cells enhance the process of recovery from acute renal injury in rats [13]. KS cells in monolayer culture appear epithelial, rapidly proliferate, and are shown to express stem cell

markers such as Sca-1, c-Kit, Nestin, and Mushashi-1 together with renal lineage marker such as Pax-2, WT-1. They seem to spontaneously differentiate into various renal tubular epithelial cells in two-dimensional (2D) culture as they become positive for aquaporin (AQP)1, AQP2, or Tamm-Horsfall glycoprotein (THP) and form numerous tubular structures in vivo after injection into the muscles of immunodeficient mice [12]. Based on the expression pattern of a marker protein, KS cells are similar to metanephric mesenchymal cells, a population in which embryonic kidney tissue stem cells have been reported to exist. Because KS cells resemble embryonic kidney tissue stem cells and form numerous tubular structures in vivo after injection into the muscles of immunodeficient mice [12], we hypothesized that these cells may have the potential to undergo further differentiation into kidney-like structures.

MATERIALS AND METHODS

Establishment of Rat KS Cells

KS cells were obtained by microdissection from adult SD rat kidneys as previously described [12]. To harvest the KS cells, we isolated single nephron from SD rat (Clea Japan, Inc., Tokyo, Japan, <http://www.clea-japan.com/en/index.html>) with microdissection methods. We microdissected each segments from nephron, such as glomeruli, proximal convoluted tubule (S1/PCT), proximal straight tubule (S2, S3), medullary thick ascending limb of Henle's loop and collecting duct. Each of the segments was transferred into wells of 96-well plate that coated with type IV collagen (BD Biosciences, www.bdbiosciences.com). The segments were cultured in a 1:1 mixture of culture supernatant (Dulbecco's modified Eagle's medium [DMEM, www.sigma-aldrich.com] containing 10% fetal calf serum (FCS)) from mouse mesenchymal cells (MCSs) provided by Dr. Sugaya T (CMIC Company, Limited, Tokyo, Japan) and modified K1 medium (1:1 mixture of DMEM and Ham's F-12 medium, [GIBCO, www.lifetechnologies.com/gibco], supplemented with 10% FCS, 5 $\mu\text{g}/\text{ml}$ insulin, 2.75 $\mu\text{g}/\text{ml}$ transferrin, 3.35 ng/ml sodium selenious acid [GIBCO, www.invitrogen.com/GIBCO], 50 nM hydrocortisone [Sigma, www.sigma-aldrich.com], 25 ng/ml hepatocyte growth factor [Sigma], and 2.5 mM nicotinamide [Sigma, www.sigma-aldrich.com]) for 7 days at 37°C and 5% CO_2 /100% humidity. Outgrowing cells were harvested. We examined the morphology, the capacity of cell proliferation, and gene expression described previously [12]. Then we harvested the KS cells. The KS cells were maintained on type IV collagen (BD Biosciences, www.bdbiosciences.com) and in same previous culture condition, as undifferentiated culture condition. KS cells were differentiated in previous culture condition without MCSs, as differentiated culture condition described previously [12]. KS cells could be harvested from an adult rat kidney multiple times. We used the harvested other KS cells with characteristics similar to those of KS 56 cells.

Establishment of Rat Metanephric Mesenchyme Cells and Ureteric Bud Cells

Metanephric mesenchyme (MM) and ureteric bud (UB) tissues were dissected from the embryonic kidneys of timed pregnant SD rats (Clea JAPAN, Japan, <http://www.clea-japan.com/en/index.html>) at day 13 (e13) of gestation with fine forceps. Cells were cultured on type IV collagen (BD Biosciences, www.bdbiosciences.com) and maintained in a 1:1 mixture of culture

supernatant (DMEM containing 10% FCS) from MCS and modified K1 medium (1:1 mixture of DMEM and Ham's F-12 medium, (GIBCO, www.lifetechnologies.com/gibco), supplemented with 10% FCS, 5 $\mu\text{g/ml}$ insulin, 2.75 $\mu\text{g/ml}$ transferrin, 3.35 ng/ml sodium selenious acid [GIBCO, www.invitrogen.com/GIBCO], 50 nM hydrocortisone [Sigma, www.sigma-aldrich.com], 25 ng/ml hepatocyte growth factor [Sigma, www.sigma-aldrich.com], and 2.5 mM nicotinamide [Sigma, www.sigma-aldrich.com]) at 37°C and 5% CO₂/100% humidity. Outgrowing cells were observed after 7 days. We harvested the outgrowing cells and divided them to obtain single cells using the limiting dilution method. Finally, we harvested a monoclonal MM cell line and a UB cell line. We used cells after four to eight passages for this study.

Three-Dimensional Culture

The KS cell sheets were incubated with trypsin and harvested. We generated a cell cluster from a KS cell sheet using the hanging drop method. The cell suspensions were incubated at 50 $\mu\text{l/well}$ using the hanging drop method. One well contained from 6.25×10^3 to 200×10^3 KS cells. We cultured the cell clusters for 6–8 hours using the same condition used for the hanging drop method. After making KS cell clusters, we placed the cell clusters into a half Matrigel (BD Biosciences, DMEM/F-12 = 1:1). The half Matrigel was situated on top of Transwell filters (Costar). Each cluster was cultured in DMEM/F-12 supplemented with 10% FCS, 250 ng/ml GDNF (R&D Systems, <http://www.rndsystems.com/>), 250 ng/ml basic fibroblast growth factor (b-FGF) (Calbiochem, http://www.merckmillipore.com/JP/ja/life-science-research/Eseb.qb.nekAAAE_ID53.L6J,nav?RedirectedFrom=http://www.calbiochem.com/), and 250 ng/ml hepatocyte growth factor (HGF) (Sigma, www.sigma-aldrich.com) for 3–7 days until it displayed budding. After budding, we added 500 ng/ml epidermal growth factor (EGF) (R&D Systems, <http://www.rndsystems.com/>) and 250 ng/ml BMP-7 (R&D Systems, <http://www.rndsystems.com/>) to the samples and incubated them at 37°C and 5% CO₂/100% humidity for 2 weeks. The kidney-like structures were observed reproducibly as described previously.

Electron Microscopy

For electron microscopic analysis, pieces of specimens were cut into small blocks and immersed in 0.1 M cacodylate buffer containing 2.5% glutaraldehyde (pH 7.2) for 2 hours, dehydrated through ascending grades of ethanol, and finally embedded in Epon 812. Thin sections were stained with uranyl acetate and citrate and examined using a transmission electron microscope (Hitachi Electron Microscope Model H-700, Hitachi, Japan).

Immunostaining

Cells were cultured on 16-well chamber slides (Nunc, www.thermosci.jp) coated with type IV collagen (BD Biosciences, www.bdbiosciences.com). And frozen tissue sections of kidney-like structures, 17-day-old embryonic rat kidneys, and adult rat kidneys were subjected to immunofluorescence staining using primary antibodies raised against Nephritin (Progen, www.progen.de), Thy-1 (Santa Cruz, www.scbt.com), vWF (Chemicon, Temecula, CA, www.millipore.com), CD31 (Abcam, www.abcam.co.jp), aquaporin-1 (Chemicon, Temecula, CA, www.millipore.com), Na-K-Cl cotransporter 2 (NKCC2) (Lifespan Biosciences,

www.lsbio.com/), THP (AbD, www.abdserotec.com), aquaporin-2 (Chemicon, Temecula, CA, www.millipore.com), vimentin (Sigma, www.sigma-aldrich.com), Six2 (Proteintech), CD133 (Santa Cruz, www.scbt.com), and pancreatic and duodenal homeobox-1 (PDX-1) (Santa Cruz, www.scbt.com); secondary antibodies conjugated with FITC or rhodamine (Chemicon, www.millipore.com) or Invitrogen, (www.lifetechnologies.com), Molecular Probes, (www.lifetechnologies.com)); and DAPI (Roche, <https://lifescience.roche.com/>) as previously described [12]. For immunohistochemistry, the samples were fixed with acetone for approximately 5 minutes at 4°C. Images were recorded using a confocal fluorescence microscope (ZEISS Confocal Laser Scanning Microscope Model LSM510), FSX-100 (Olympus, Japan), or BIOZERO BZ-8000 fluorescent microscope (Keyence, Japan).

PCR

To release the kidney-like structures from the half Matrigel ECMs, we used a cell recovery solution (BD Biosciences, www.bdbiosciences.com). We washed the kidney-like structures and the half Matrigel twice with Ca²⁺Mg²⁺ phosphate-buffered saline (PBS). We then added cell recovery solution on top of the half Matrigel ECMs, allowed it to sit for 10–20 minutes, removed the kidney-like structures using fine forceps under a microscope, and placed the kidney-like structure in tubes. Total RNA was extracted using the RNase plus Mini Kit (QIAGEN, www.qiagen.co.jp). The total RNA was reverse transcribed into cDNA. As RT-PCR, amplified using the GeneAmp RNA PCR core kit (Roche, <https://lifescience.roche.com/>) with specific primer pairs for each gene. The reactions were subjected to agarose gel electrophoresis and visualized as previously described [12]. The primers are listed in Supporting Information Table S1.

Establishment of Single KS Cell Colony from KS Cells

The KS cells were separated to single KS cell using limiting dilution methods. The single KS cell was cultured on type IV collagen (BD Biosciences, www.bdbiosciences.com) and was maintained in a 1:1 mixture of culture supernatant (DMEM containing 10% FCS) from MCSs and modified K1 medium (1:1 mixture of DMEM and Ham's F-12 medium, supplemented with 10% FCS, 5 $\mu\text{g/ml}$ insulin, 2.75 $\mu\text{g/ml}$ transferrin, 3.35 ng/ml sodium selenious acid [GIBCO, www.invitrogen.com/GIBCO], 50 nM hydrocortisone [Sigma, www.sigma-aldrich.com], 25 ng/ml hepatocyte growth factor [Sigma, www.sigma-aldrich.com], and 2.5 mM nicotinamide [Sigma, www.sigma-aldrich.com]) at 37°C and 5% CO₂/100% humidity as previous described [12].

Statistical Analysis

The number of kidney-like structure formation from single KS cells data was compared between group using Student's *t* tests. Significance was defined as $p < .05$.

RESULTS

Character of KS Cells

KS cells express stem cell markers such as Sca-1, c-Kit, Nestin, and Mushashi-1 together with renal lineage marker such as Pax-2, WT-1. In addition, KS cells expressed Six2 [8] (Fig. 1B), CD133 [10, 14] (Fig. 1C), and Vimentin [10] (Fig. 1D), which

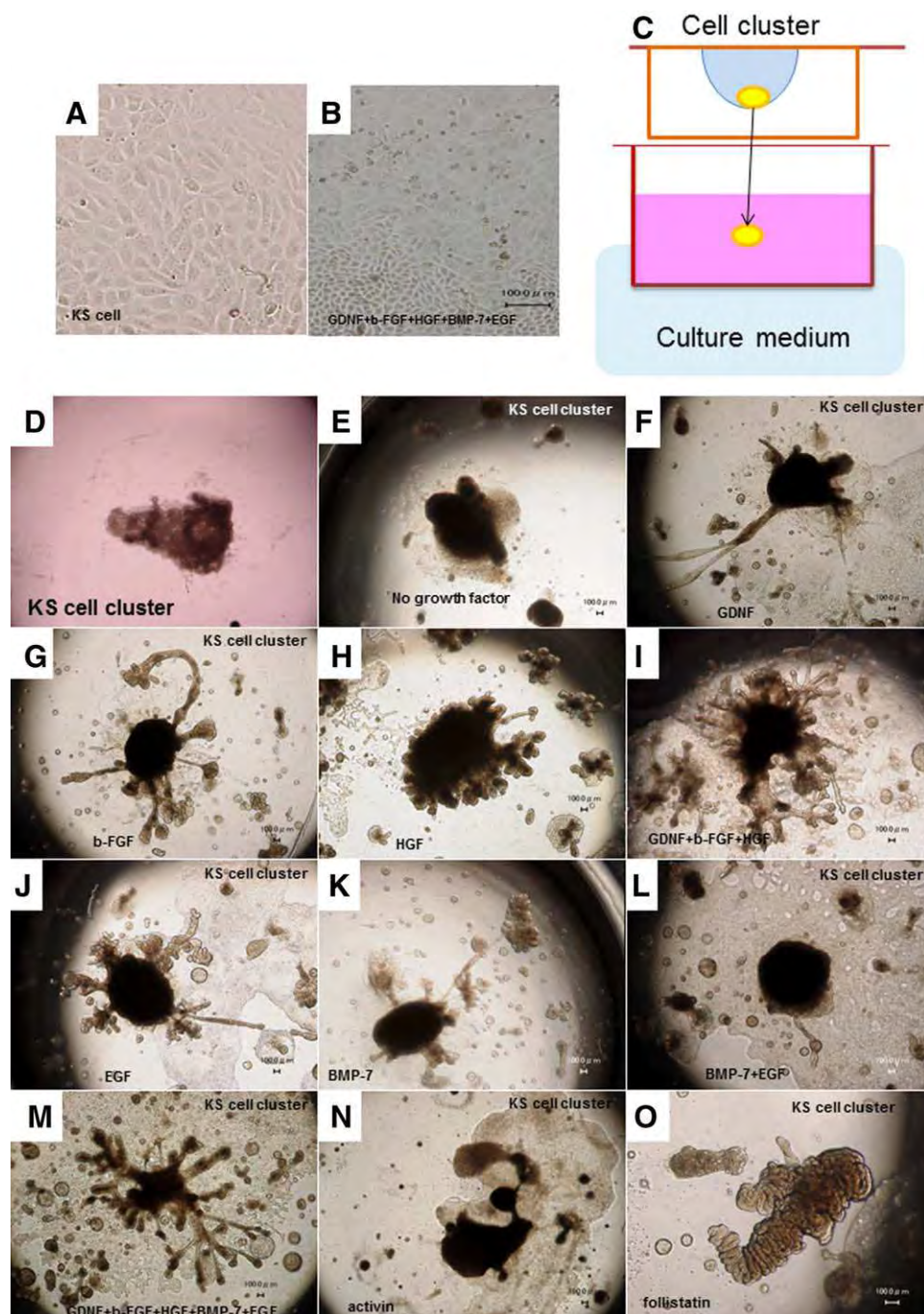


Figure 2. Development of kidney-like structures from KS cells in vitro. **(A):** KS cells on type IV collagen. **(B):** KS cell sheet. Dulbecco's modified Eagle's medium (DMEM)/F-12, 10% FCS, 250 ng/ml GDNF, 250 ng/ml b-FGF, 250 ng/ml HGF, 250 ng/dl BMP-7, and 500 ng/ml EGF. **(C):** The method used for three-dimensional culture. A KS cell cluster was placed into half Matrigel using a combination of culture conditions. **(D–O):** KS cell clusters were cultured under various conditions for 3 weeks. **(D):** KS cell cluster in half Matrigel. **(E):** DMEM/F-12 and 10% FCS. **(F):** DMEM/F-12, 10% FCS and 250 ng/ml GDNF. **(G):** DMEM/F-12, 10% FCS, and 250 ng/ml b-FGF. **(H):** DMEM/F-12, 10% FCS, and 250 ng/ml HGF. **(I):** DMEM/F-12, 10% FCS, 250 ng/ml GDNF, 250 ng/ml b-FGF, and 250 ng/ml HGF. **(J):** DMEM/F-12, 10% FCS, and 500 ng/ml EGF. **(K):** DMEM/F-12, 10% FCS and 250 ng/ml BMP-7. **(L):** DMEM/F-12, 10% FCS, 250 ng/dl BMP-7, and 500 ng/ml EGF. **(M):** DMEM/F-12, 10% FCS, 250 ng/ml GDNF, 250 ng/ml b-FGF, 250 ng/ml HGF, 500 ng/ml EGF, and 250 ng/ml BMP-7. **(N):** DMEM/F-12, 10% FCS, and 250 ng/ml activin A. **(O):** DMEM/F-12, 10% FCS, and 250 ng/ml follistatin. All cultures contained antibiotics (1% penicillin + streptomycin). **(H, I):** Representative pictures were presented after KS cell cluster culture for 3 weeks from three to four independent experiments. Scale bar = 100 µm. Abbreviations: FCS, fetal calf serum; b-FGF, basic fibroblast growth factor; EGF, epidermal growth factor; GDNF, glial cell line-derived neurotrophic factor; HGF, hepatocyte growth factor; KS cell, kidney stem/progenitor cell.

are reported as kidney stem cell markers that were expressed in embryonic kidney (Fig. 1E–1G) [8, 10, 14]. The Musahi-1-positive cells decreased when we cultured the KS cells under

differentiated culture condition (Supporting Information Fig. S1A, S1B). In addition, aquaporin-1 altered the expression and distribution when we cultured KS cells under differentiated

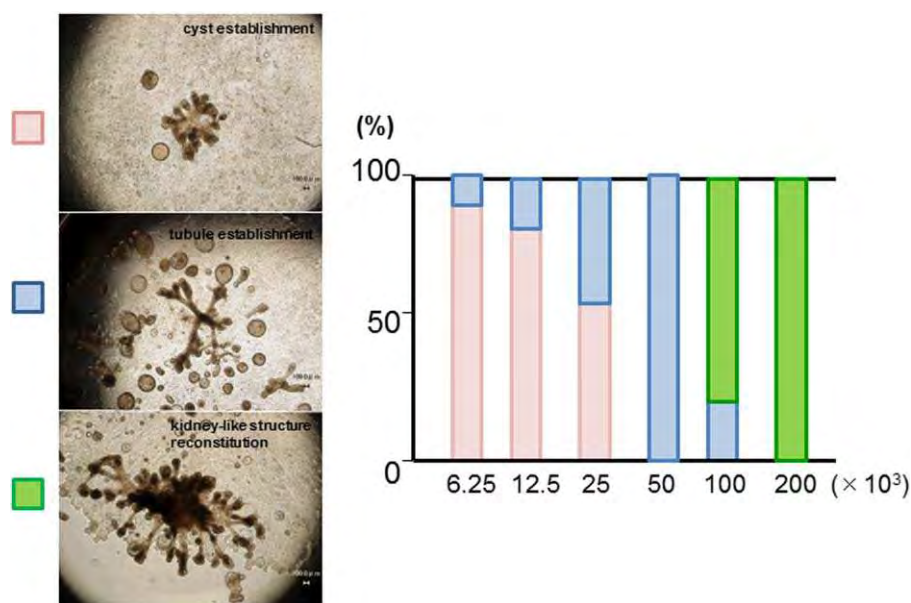


Figure 3. The relationship between cell number in the cluster and the ability to reconstitute a kidney-like structure. Red bar: cyst formation, Blue bar: long distinct tubules formation, Green bar: tubules with ball-like structures at the tip. Horizontal axis represents kidney stem/progenitor cell (KS cell) number ($6.25\text{--}200 \times 10^3$ cells)/cluster. The KS cell clusters were cultured for 3 weeks. Representative photomicrographs were from three independence experiments. Scale bar = 100 μm .

culture condition (Supporting Information Fig. S1C, S1D). Based on these findings, KS cells may be very close to adult kidney-specific tissue stem cells. Thus, in this study, we explore their potential to self-organize and reconstruct the kidney.

Reconstituting Kidney-Like Structure from Kidney Stem/Progenitor Cell Cluster

The KS cells grew like cobblestone in 2D condition (Fig. 2A). The KS cells did not show any signs of morphogenesis in the presence of any growth factors when tested under 2D culture conditions (Fig. 2B). Therefore, we generated cell clusters from the KS cells using the hanging drop method (Fig. 2C). The cell clusters (Fig. 2D) were transferred into three-dimensional extracellular matrix (ECM) gels and cultured in the presence of multiple growth factors. These growth factors were chosen because they reported to be critical in certain stages of kidney development [15–19]. Different growth factor combinations have been tested (Fig. 2E–2O) and a combination of GDNF, b-FGF, HGF, EGF, and BMP-7 consistently induce the most kidney-like structure (Fig. 2M), defined as a central large cyst (pelvis-like structure) with multiple tubular projections (collecting duct/kidney tubule-like structure), with ball-like termini (glomerulus-like structure) after 3–4 weeks of culture. The efficiency of inducing such structures was more than 70%. As long as sufficient numbers of KS cells were put into the cluster (describe later), the kidney-like structures developed 9–10 times out of 12 attempts.

This morphogenesis seemed unique to KS cells as either embryonic kidney-derived UB cell cluster or metanephric mesenchyme cell cluster did not undergo such a process (compare Supporting Information Fig. S2A–S2C). Moreover, another tissue stem cell type, a PDX-1-positive cell line (Supporting Information Fig. S2D, S2E) that has been reported to be a pancreas progenitor cell [20], did not reconstitute the renal

structure under the same culture conditions (Supporting Information Fig. S2F). However, the PDX-1-positive cell cluster reconstituted pancreatic-like formation in another culture condition (Supporting Information Fig. S2G). These results suggested that each tissue stem cell has a unique ability to differentiate into its organ of origin.

We also noticed that three-dimensional structure of KS cells depended on the size of the initial KS cell cluster (Fig. 3): (a) when less than 6.25×10^3 cells were used for the cluster, only cystic structures developed, (b) long, distinct tubular structures became apparent as the initial cell number was increased up to 50×10^3 cells, and (c) kidney-like structures developed when the initial cell number exceeded 100×10^3 cells (Fig. 3).

Morphological Analysis of Kidney-Like Structure

To characterize the kidney-like structures further, we examined each substructure at the cellular level. Ball-like structures at the tips of numerous tubules contained many cells (Fig. 4A). We examined each substructure at the cellular level. Round, glomerulus-like structures were observed at the tips of numerous tubules after 4 weeks of culture (Fig. 4B). The glomerular configurations consisted of lumens covered by Bowman's capsule-like structures (Fig. 4C). They were distinct from the cysts and looked similar to the kidney glomeruli by electron microscopy (EM) analysis (compare Fig. 4D, 4E with Fig. 4F, 4G). The tubules that connected directly to the glomerulus-like structures were slightly thicker than those in the center of the tubular structures (Fig. 4H). These tubules were composed of cubic-columnar epithelial cells with many villi on the lumen side (Fig. 4I). This structure was similar to that of the kidney proximal tubules in vivo, which also have the brush border (compare Fig. 4J with Fig. 4K, 4L). Following the proximal tubule-like structures, another distinct tubular structure was observed, in which the lumen was surrounded by ciliated (Fig. 4M), flatter epithelial cells resembling the structure of the

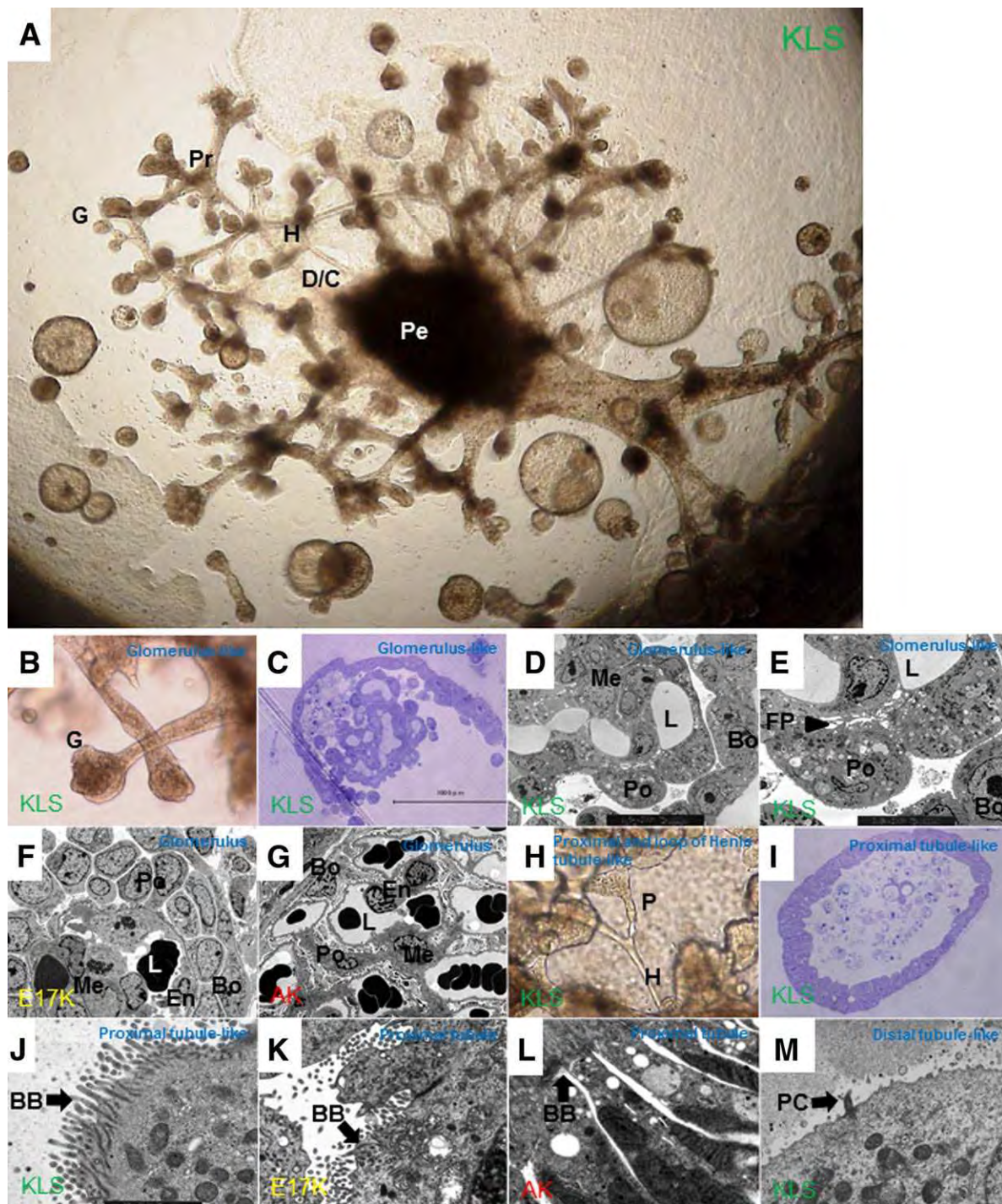


Figure 4. Morphological analysis of the kidney-like structure. **(A):** A kidney stem/progenitor cell cluster formed a KLS after 4 weeks of incubation using Dulbecco's modified Eagle's medium/F-12 plus 10% FCS, 250 ng/ml GDNF, 250 ng/ml b-FGF, 250 ng/ml HGF, 250 ng/dl BMP-7, and 500 ng/ml EGF. Glomerulus-like structures were formed at the tips of the tubular structures, proximal-like tubules, distal-like tubules, collecting duct-like tubules, and renal pelvis-like structures. **(B):** Light microscopy of a glomerulus-like structure. **(C):** A section of the glomerulus-like structure, as viewed using Toluidine blue staining. **(D):** Electron microscopy of a glomerulus-like structure ($\times 800$). **(E):** Glomerulus-like structure ($\times 3,000$). **(F):** Glomerulus of a 17-day-old embryonic kidney ($\times 2,000$). **(G):** Glomeruli of the adult kidney ($\times 2,000$). **(H):** Light microscopy of proximal-like tubules and the loop of Henle-like structure. **(I):** Tubules stained with Toluidine blue. The tubular structure consists of several cubic-columnar epithelial cells. **(J):** Proximal tubule-like cells. BB-like structure: (arrow) ($\times 10,000$). **(K):** Proximal tubular cells of E17 kidney. BB structure. Arrow: BB ($\times 8,000$). **(L):** Proximal tubular cells of adult kidney. BB structure. Arrow: BB ($\times 9,000$). **(M):** Primary cilia on distal tubule-like cells ($\times 10,000$). Arrow: PC. Proximal, proximal tubules-like structure; distal, distal tubules-like structure. Representative photomicrographs were from more than five independent experiments. Scale bar = 100 μm . Abbreviations: BB, brush border; Bo, Bowman capsule epithelial-like cell; CD, collecting duct-like structure; D/C, distal tubule-like structure or collecting duct-like structure; En, endothelial cell; G, glomerulus-like structure; H, loop of Henle-like structure; KLS, kidney-like structure; L, lumen; LOH, loop of Henle-like structure; Me, mesangial-like cell; P, proximal-like tubule; PC, primary cilia; Pe, renal pelvis-like structure; Po, podocyte-like cell; Pr, proximal tubule-like structure.

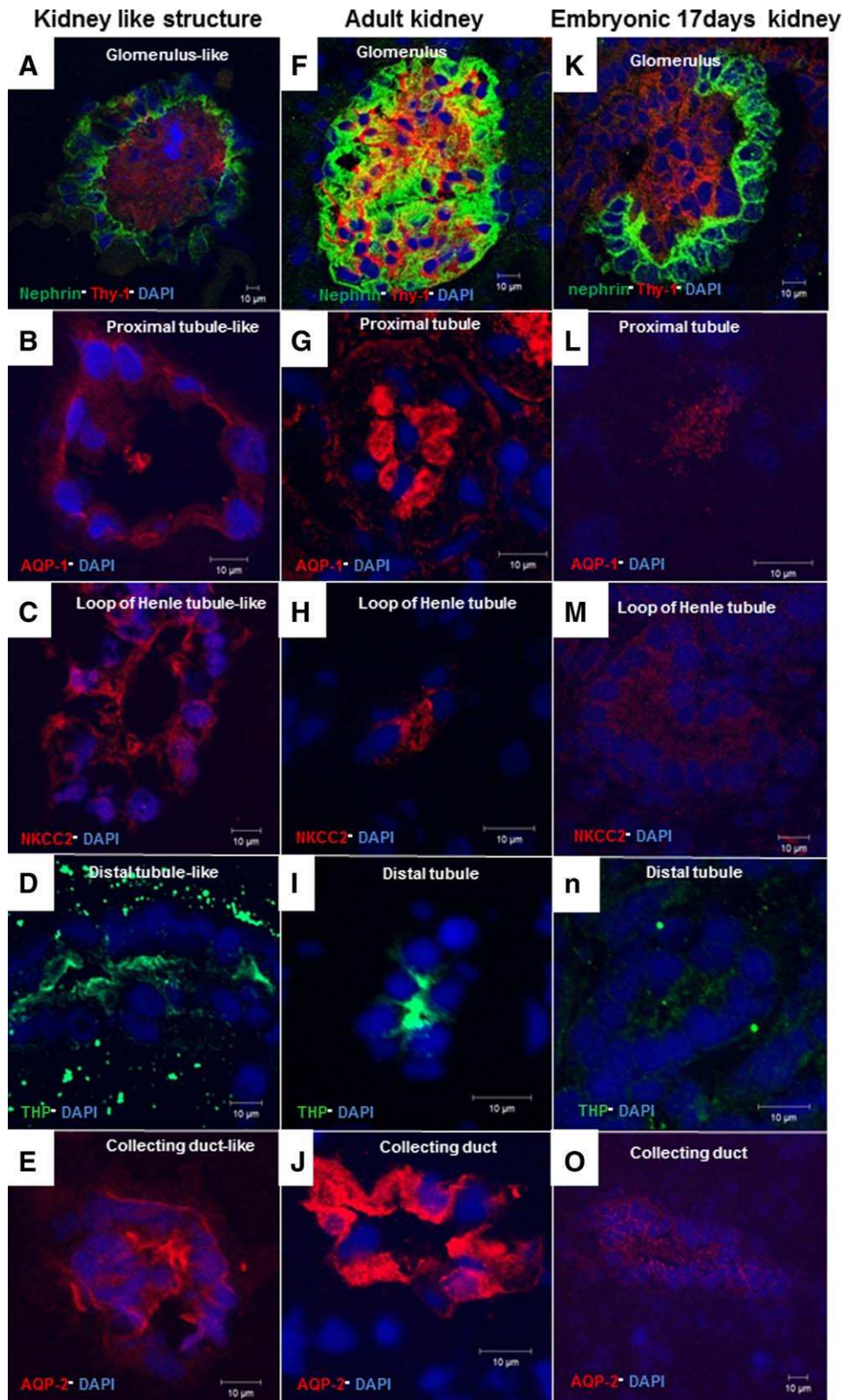


Figure 5. Segment-specific marker protein expression of the kidney-like structure. (A–E): Staining of each segment of the kidney-like structures. (F–J): Staining of an adult rat kidney (8–12W rats). (K–O): Staining of an embryonic 17 days old kidney. Staining of sections of the glomerulus-like structures or glomeruli. (A, F, K): Green, nephrin; red, Thy-1; blue, DAPI. Staining of the tubule-like structures or tubules. (B, G, L): Red, AQP-1; blue: DAPI. (C, H, M): Red, NKCC2; blue, DAPI. (D, I, N): Green, THP; blue, DAPI. (E, J, O): Red, AQP-2; blue, DAPI. Scale bar = 10 μm. Representative photomicrographs were from 6 to 10 independent experiments. Abbreviations: AQP-1, aquaporin-1; NKCC2, Na-K-Cl cotransporter 2; THP, Tamm-Horsfall glycoprotein.

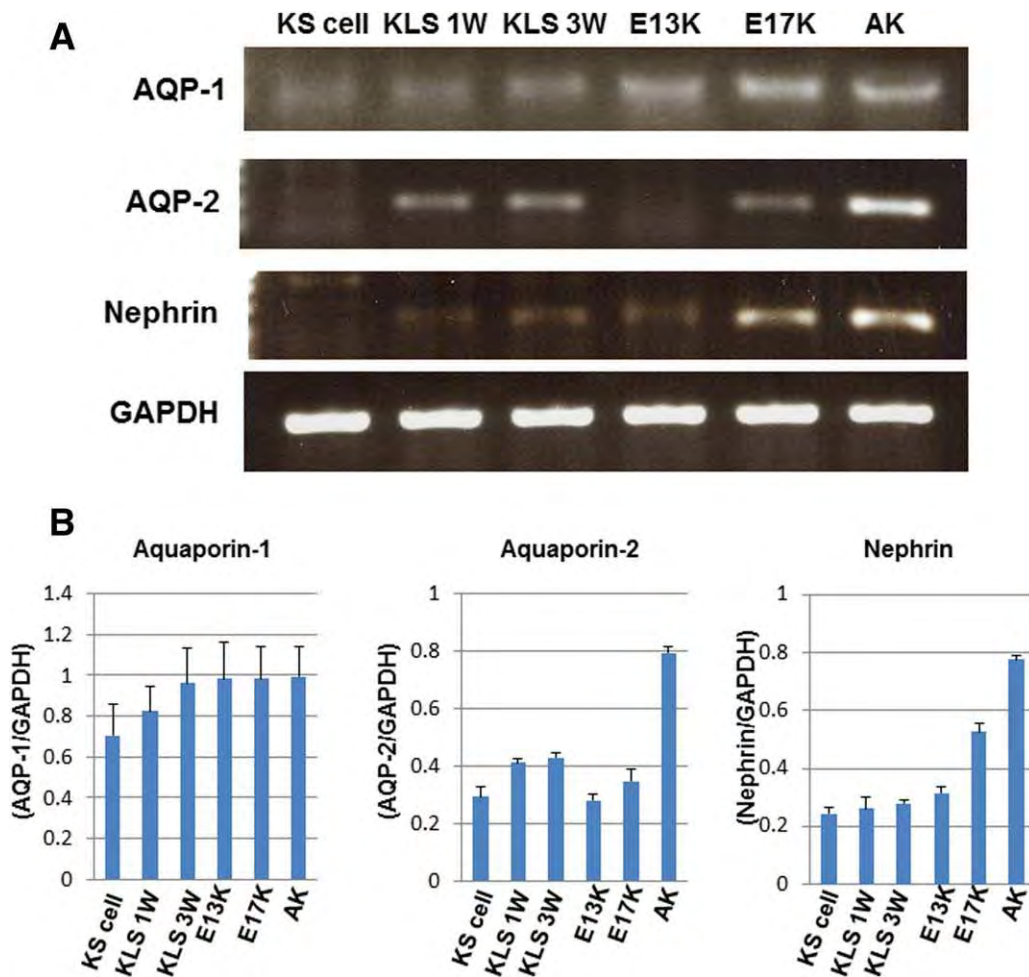


Figure 6. Time course of the expression of kidney-specific genes in kidney-like structures. **(A):** Each gene expression band was scanned and subjected to densitometry. Each kidney-specific gene was expressed more strongly as the time in culture increased, paralleling the days of embryonic kidney development ($n = 3$, representative data shown). **(B):** The AQP-1/GAPDH, AQP-2/GAPDH, and Nephrin/GAPDH were measured. Representative results obtained from two independent experiments. Data represent mean \pm SD values. Abbreviations: 1W, kidney-like structures cultured for 1 week; 3W, kidney-like structures cultured for 3 weeks; AK, adult kidney (8–12 weeks); AQP-1, aquaporin-1; AQP-2, aquaporin-2; E13, 13-day-old embryonic kidney; E17, 17-day-old embryonic kidney; KS, kidney stem/progenitor cell.

more distal kidney tubules. Thus, the kidney-like structure turned out to contain at least three distinct segments, similar to kidney glomerulus, proximal tubules, and distal tubules.

Molecular Marker Analysis of Kidney-Like Structure

An immunohistochemical analysis revealed that Nephrin [21] (a podocyte marker, Fig. 5A) and Thy-1 [22] (a mesangial cell marker, Fig. 5A) were expressed in the glomerulus-like structures, and Nephrin-positive cells and Thy-1-positive cells were observed at distinct sites in the glomerulus-like structures (Fig. 5A). The Nephrin and Thy-1 protein distribution of glomerular structure in kidney-like structure are very close to that of embryonic day 17 kidney glomeruli (compare Fig. 5A with Fig. 5F, 5K). Although we found foot process-like protrusion in the EM picture (Fig. 4E, arrowhead), the majority of the nephrin-positive cells were segregated from the Thy-1 positive cells, indicating that the podocyte-like cells have not form a functional filtration barrier.

Following the glomerulus-like structure, the proximal tubule-like structures were present, where the cells in the tubular structure stained positive for aquaporin-1 [23], a

proximal cell marker (compare Fig. 5B with Fig. 5G, 5L). In the thinner tubular segment, some tubules were positive for NKCC2 [24], a marker for the loop of Henle cells (compare Fig. 5C with Fig. 5H, 5M), and some were positive for THP (compare Fig. 5D with Fig. 5I, 5N) [25], a marker for distal-collecting duct cells, and others were positive for aquaporin-2 (compare Fig. 5E with Fig. 5J, 5O) [26], a collecting duct cell marker. Interestingly, expression levels of these tubular markers in the kidney-like structures appear closer to those in the adult kidney than the E17 kidney. Low magnification immunostaining images revealed that the cells at the tips, in the glomerulus-like structures, were different from the cells in the proximal tubule-like structures (Supporting Information Fig. S3A–S3D). Similar results were obtained for the collecting duct-like structures and distal tubule-like structures (Supporting Information Fig. S3E–S3G). However, we were unable to say that loop of Henle and distal tubules are formed successively as distinct segments.

It is of note that very little vWF or CD31 (an endothelial marker) expression was observed in the cells of the

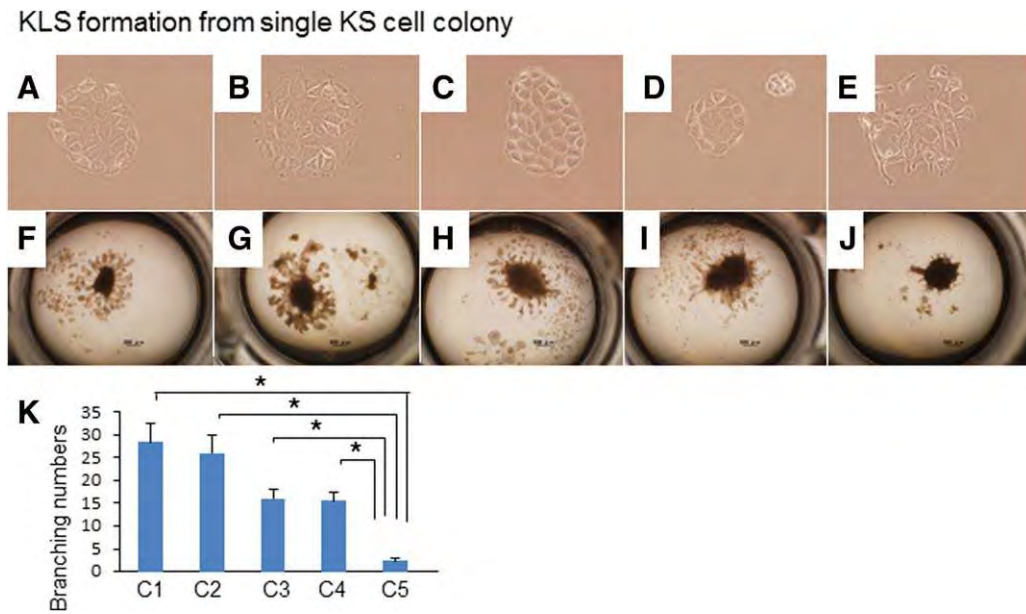


Figure 7. KLS formation from single KS cell clones. Five randomly selected single KS cell clones were established and named, C1–5. Light microscopic photographs. C1; **A**, C2; **B**, C3; **C**, C4; **D**, C5; **E**. KLSs were formed from each KS single-cell clone, C1–5. Light microscopic photographs. C1; **F**, C2; **G**, C3; **H**, C4; **I**, C5; **J**. **(K)**: A comparison of the number of tubules produced by individual KS cell clone; each cell revealed a slightly different ability to reconstitute a kidney-like structure. *, $p < .05$. Representative data from three independent experiments. Scale bar = 100 μm . Abbreviations: KLS, kidney-like structure; KS cell, kidney stem/progenitor cell.

glomerulus-like structures (Supporting Information Fig. S4A–S4C). These endothelial cells were observed in the glomerulus of the adult kidney (positive control; Supporting Information Fig. S4D, S4E).

When the expression levels of glomerulus- (nephrin), proximal tubule-(aquaporin 1), and collecting duct-(aquaporin 2)-specific gene were majored in the kidney-like structures at different time points, they were increased at the later time points (Fig. 6), consistent with the idea that the cells in the kidney-like structures were in the process of differentiation/maturation.

A Single Clone of KS Cells Can Develop into the Kidney-Like Structures

We have shown previously that more than certain numbers of KS cells were required to undergo full-blown morphogenesis to occur. Then one could argue that only a part of KS cells possess tissue stem cell-like characteristics. To counter this argument, we showed here that kidney-like structures could be developed from a single KS cell. We established five different clones of KS cells by limiting dilution (C1–5; Fig. 7A–7E), and these cells were expanded in 2D culture. Cell clusters of each clone were generated by the hanging drop method, followed by three-dimensional ECM gel culture in the presence of growth factors, as described. Four of the five clones formed kidney-like structures (Fig. 7F–7J, 7K). Although it is not clear when the KS cells begin to differentiate or how differentiation progressed, many, if not all, KS cells have the ability to reconstitute different kidney epithelial cells. This observation, together with the fact that KS cells retain their characteristics after several passages [12], suggests that these cells are adult kidney stem cells.

DISCUSSION

Diep et al. reported that adult nephron progenitor cells can produce new nephrons in adult zebrafish in vivo [27], and Rinkevich et al. reported that the adult mammalian kidney undergoes continuous tubulogenesis via expansions of fate-restricted clones [28]. A cluster of KS cells was shown to differentiate into a kidney-like structure without requiring embryonic primordial cell types, such as metanephric mesenchyme and ureteric bud cells, suggesting that organogenesis beginning from adult tissue stem/progenitor cells may follow a different developmental program than organogenesis during embryonic development. In addition, these researchers reported that cell aggregates, rather than single stem cells, are necessary to regenerate the kidney, which is very similar to the results reported here.

We further characterized KS cells with different markers. Because KS cells are derived from S3 segment of kidney proximal tubular cells, they should originate from nephron progenitor cells present in the metanephric mesenchyme. Recently, Kobayashi et al. reported such cells are positive for Six2 and such cells are reported to be absent in the adult kidney [8]. KS cells were positive for Six2 (Fig. 1B), suggesting that these cells may retain embryonic nephron stem cell characteristics. How Six2 became positive in adult kidney-derived KS cells is an interesting topic for further investigation. Sagrinati et al. reported that CD133-positive parietal epithelial cells of the Bowman's capsule are adult kidney stem cells [14] and recently Lindgren et al. reported that such cells are also reside in the proximal tubule [10]. They used CD133 and Vimentin as markers of possible kidney adult stem cells. KS cells were positive for these markers (Fig. 1). To our knowledge, there is no single bona fide marker specific for adult

kidney stem cells at present. Given the fact that KS cells were positive for embryonic nephron tissue stem cell marker Six2 and possible adult kidney tissue stem cell marker combination CD133/Vimentin, KS cells are likely to be very close, if not identical, to adult kidney stem cells. It should be underscored that KS cells could differentiate into collecting duct-like cells or mesangial-like cells, which are not derived from nephron progenitors.

Eiraku et al. reported the reconstitution of a three-dimensional retinal structure from ESCs in vitro [29] by inducing ESCs to differentiate into a cluster of neural lineage cells followed by three-dimensional culture. Together with our results, this finding suggests that tissue progenitor cells likely possess an intrinsic program to produce the three-dimensional structure of the organ from which they originate.

The kidney-like structures could not show the vascularization and make urine. The further examinations are required to elucidate the issues. However, we believed that these kidney-like structures should be attractive for in vitro kidney regeneration and could contribute for not only the elucidation of kidney regeneration but also for in vitro study toward alternatives to animal experiments and custom-made medicine.

CONCLUSIONS

In summary, we have identified adult KS cells in rat that can regenerate a kidney-like structure from a single cell in vitro. Although the physiological roles of such cells are currently unclear, analogous cells in the adult human kidney would be a valuable resource for the regeneration of kidneys in vitro.

ACKNOWLEDGMENTS

A portion of this study was supported by the Health and Labor Sciences Research Grants for Research on Tissue

Engineering from the Ministry of Health Labor and Welfare of Japan, the programme for the promotion of fundamental studies in Health Sciences of the National Institute of Biomedical Innovation (VIBIO), a Grant-in-Aid for Young Scientists (B) and a grant from the Okayama Medical Foundation, the Ministry of Economy, Trade and Industry (METI), Japan, and joint research with Organ Technologies, Inc. We appreciate the technical contributions of Dr. Takeshi Sugaya (Cimic, Co., Ltd., Japan) and Dr. Naoshi Shinozaki (Cornea Center & Eye Bank, Tokyo Dental College, Ichikawa General Hospital) and the kind advice of Dr. Kazuhiro Sakurada (Sony Computer Science Laboratories, Inc., Japan) and Dr. Naoya Kobayashi (Okayama Saidaigi Hospital).

AUTHOR CONTRIBUTIONS

S.K.: conception, design, financial support, collection, assembly of data, manuscript writing, and final approval of manuscript; H.S.: manuscript writing and final approval of manuscript; H.M.: administrative support and final approval of manuscript.

DISCLOSURE OF POTENTIAL CONFLICTS OF INTEREST

We declare that the establishment of rKS56 cells and the potential for their therapeutic application to renal disorders were filed and submitted to the Japan Patent Office (Issue No. 2003-071029: Kidney stem cells, isolation methods to separate kidney stem cells, therapeutic approach for kidney diseases) in March 2003. The methods used to reconstitute organ structures were filed and submitted to the Japan Patent Office in August 2009 (Issue No. 2010-063659: Process for production of bioartificial organ). There are no further patents, products in development or marketed products to declare. Co-author, Hiroaki Asai is employed by Organ Technologies, Inc.

REFERENCES

- 1 Saxen L. Organogenesis of the Kidney. Cambridge: Cambridge University Press, 1987.
- 2 Yokoo T, Ohashi T, Shen JS et al. Human mesenchymal stem cells in rodent whole-embryo culture are reprogrammed to contribute to kidney tissues. *Proc Natl Acad Sci USA* 2005;102:3296-3300.
- 3 Song JJ, Guyette JP, Gilpin SE et al. Regeneration and experimental orthotopic transplantation of a bioengineered kidney. *Nat Med* 2013;19:646-651.
- 4 Rosines E, Sampogna RV, Johkura K et al. Staged in vitro reconstitution and implantation of engineered rat kidney tissue. *Proc Natl Acad Sci USA* 2007;104:20938-20943.
- 5 Kim D, Dressler GR. Nephrogenic factors promote differentiation of mouse embryonic stem cells into renal epithelia. *J Am Soc Nephrol* 2005;16:3527-3534.
- 6 Mae S, Shono A, Shiota F et al. Monitoring and robust induction of nephrogenic intermediate mesoderm from human pluripotent stem cells. *Nat Commun* 2013;4:1367.
- 7 Taguchi A, Kaku Y, Ohmori T et al. Redefining the in vivo origin of metanephric nephron progenitors enables generation of complex kidney structures from pluripotent stem cells. *Cell Stem Cell* 2014;14:53-67.
- 8 Kobayashi A, Valerius MT, Mugford JW et al. Six2 defines and regulates a multipotent self-renewing nephron progenitor population throughout mammalian kidney development. *Cell Stem Cell* 2008;7:169-181.
- 9 Maeshima A, Yamashita S, Nojima Y. Identification of renal progenitor-like tubular cells that participate in the regeneration processes of the kidney. *J Am Soc Nephrol* 2003;14:3138-3146.
- 10 Lindgren D, Boström AK, Nilsson K et al. Isolation and characterization of progenitor-like cells from human renal proximal tubules. *Am J Pathol* 2011;178:828-837.
- 11 Abedin MJ, Imai N, Rosenberg ME et al. Identification and characterization of Sall1-expressing cells present in the adult mouse kidney. *Nephron Exp Nephrol* 2011;119:e75-82.
- 12 Kitamura S, Yamasaki Y, Kinomura M et al. Establishment and characterization of renal progenitor like cells from S3 segment of nephron in rat adult kidney. *FASEB J* 2005; 19:1789-1797.
- 13 Kinomura M, Kitamura S, Tanabe K et al. Amelioration of cisplatin-induced acute renal injury by renal progenitor-like cells derived from the adult rat kidney. *Cell Transplantation* 2008;17:143-158.
- 14 Sagrinati C, Netti GS, Mazzinghi B et al. Isolation and characterization of multipotent progenitor cells from the Bowman's capsule of adult human kidneys. *J Am Soc Nephrol* 2006;17:2443-2456.
- 15 Vega QC, Worby CA, Lechner MS et al. Glial cell line-derived neurotrophic factor activates the receptor tyrosine kinase RET and promotes kidney morphogenesis. *Proc Natl Acad Sci USA* 1996;93:10657-10661.
- 16 Perantoni AO, Dove LF, Karavanova I. Basic fibroblast growth factor can mediate the early inductive events in renal development. *Proc Natl Acad Sci USA* 1995;92:4696-4700.
- 17 Santos OF, Barros EJ, Yang XM et al. Involvement of hepatocyte growth factor in kidney development. *Dev Biol* 1994;163:525-529.

- 18** Cybulsky AV, Goodyer PR, McTavish AJ. Epidermal growth factor receptor activation in developing rat kidney. *Am J Physiol* 1994; 267:F428–436.
- 19** Dudley AT, Lyons KM, Robertson EJ. A requirement for bone morphogenetic protein-7 during development of the mammalian kidney and eye. *Genes Dev* 1995;9: 2795–2807.
- 20** Taniguchi M, Yamaguchi T, Otsuki M. Induction of PDX-1-positive cells in the main duct during regeneration after acute necrotizing pancreatitis in rats. *J Pathol* 2002;197: 638–646.
- 21** Ruotsalainen V, Ljungberg P, Wartiovaara J et al. Nephin is specifically located at the slit diaphragm of glomerular podocytes. *Proc Natl Acad Sci USA* 1999;6: 7962–7967.
- 22** Yamamoto T, Yamamoto K, Kawasaki K et al. Immunoelectron microscopic demonstration of Thy-1 antigen on the surfaces of mesangial cells in the rat glomerulus. *Nephron* 1986;43:293–298.
- 23** Sabolić I, Valenti G, Verbavatz JM et al. Localization of the CHIP28 water channel in rat kidney. *Am J Physiol* 1992;263:C1225–1233.
- 24** Igarashi P, Vanden Heuvel GB, Payne JA et al. Cloning, embryonic expression, and alternative splicing of a murine kidney-specific Na-K-Cl cotransporter. *Am J Physiol* 1995;269:F405–418.
- 25** Sikri KL, Alexander DP, Foster CL. Localization of Tamm-Horsfall glycoprotein in the normal rat kidney and the effect of adrenalectomy on its localization in the hamster and rat kidney. *J Anat* 1982;135:29–45.
- 26** Fushimi K, Uchida S, Hara Y et al. Cloning and expression of apical membrane water channel of rat kidney collecting tubule. *Nature* 1993;361:549–552.
- 27** Diep CQ, Ma D, Deo RC et al. Identification of adult nephron progenitors capable of kidney regeneration in zebrafish. *Nature* 2011;470:95–100.
- 28** Rinkevich Y, Montoro DT, Contreras-Trujillo H et al. In vivo clonal analysis reveals lineage-restricted progenitor characteristics in mammalian kidney development, maintenance, and regeneration. *Cell Rep* 2014;22:1270–1283.
- 29** Eiraku M, Takata N, Ishibashi H et al. Self-organizing optic-cup morphogenesis in three-dimensional culture. *Nature* 2011;472:51–56.



See www.StemCells.com for supporting information available online.

DEFINE YOUR FLOW



Own the direction of your research with the trailblazing ZE5™ Cell Analyzer

30-parameter analysis, unmatched sample flexibility, and easy to learn and use Everest™ Software now give both novice and expert users the power to set their own pace for discovery.

Visit us at bio-rad.com/info/DefineYourFlow

BIO-RAD

In Vivo Rescue of the Hematopoietic Niche By Pluripotent Stem Cell Complementation of Defective Osteoblast Compartments

RHIANNON CHUBB,^a JAMES OH,^a ALYSSA K. RILEY,^b TAKAHARU KIMURA,^c SEAN M. WU,^{b,d,e}
JOY Y. WU ^{a,c,d}

Key Words. Pluripotent stem cell • Osteoblast • Bone formation • Hematopoietic niche

^aEndocrine Unit and
^bCardiovascular Research
Center, Massachusetts
General Hospital, Boston,
Massachusetts, USA; ^cDivision
of Endocrinology and
^dDivision of Cardiovascular
Medicine, Stanford University
School of Medicine, Stanford,
California, USA; ^eHarvard
Stem Cell Institute,
Cambridge, Massachusetts,
USA

Correspondence: Joy Y. Wu,
M.D., Ph.D., 300 Pasteur Dr., S-
025, Stanford, California 94305,
USA. Telephone: 650-736-9654;
Fax: 650-725-7085; e-mail:
jyw1@stanford.edu

Received December 16, 2016;
accepted for publication June
25, 2017; first published online
in *STEM CELLS EXPRESS* July 25,
2017.

[http://dx.doi.org/
10.1002/stem.2670](http://dx.doi.org/10.1002/stem.2670)

ABSTRACT

Bone-forming osteoblasts play critical roles in supporting bone marrow hematopoiesis. Pluripotent stem cells (PSCs), including embryonic stem cells (ESCs) and induced PSCs (iPSC), are capable of differentiating into osteoblasts. To determine the capacity of stem cells needed to rescue aberrant skeletal development and bone marrow hematopoiesis *in vivo*, we used a skeletal complementation model. Mice deficient in *Runx2*, a master transcription factor for osteoblastogenesis, fail to form a mineralized skeleton and bone marrow. Wild-type (WT) green fluorescent protein (GFP)⁺ ESCs and yellow fluorescent protein (YFP)⁺ iPSCs were introduced into *Runx2*-null blastocyst-stage embryos. We assessed GFP/YFP⁺ cell contribution by whole-mount fluorescence and histological analysis and found that the proportion of PSCs in the resulting chimeric embryos is directly correlated with the degree of mineralization in the skull. Moreover, PSC contribution to long bones successfully restored bone marrow hematopoiesis. We validated this finding in a separate model with diphtheria toxin A-mediated ablation of hypertrophic chondrocytes and osteoblasts. Remarkably, chimeric embryos harboring as little as 37.5% WT PSCs revealed grossly normal skeletal morphology, suggesting a near-complete rescue of skeletogenesis. In summary, we demonstrate that fractional contribution of PSCs *in vivo* is sufficient to complement and reconstitute an osteoblast-deficient skeleton and hematopoietic marrow. Further investigation using genetically modified PSCs with conditional loss of gene function in osteoblasts will enable us to address the specific roles of signaling mediators to regulate bone formation and hematopoietic niches *in vivo*. *STEM CELLS* 2017;35:2150–2159

SIGNIFICANCE STATEMENT

Given the central role of bone-forming osteoblasts in supporting bone marrow hematopoiesis and in maintaining bone mass and strength, osteoblasts represent an important target tissue for regenerative medicine. Although several groups have reported the directed differentiation of pluripotent stem cells (PSCs) into osteoblasts *in vitro*, the field has lacked a rigorous assay with which to evaluate the bone-forming and hematopoiesis-supporting capacity of PSC-derived osteoblasts *in vivo*. Here, we describe two novel complementation assays, with which we demonstrate that PSC-derived osteoblasts can compensate for the loss of osteoblast lineage cells in transgenic mice to form mineralized bone and bone marrow hematopoietic niche *in vivo*. Remarkably, the loss of >50% of endogenous osteoblasts during embryonic skeletal development can be rescued by the injected PSCs. These assays will greatly enhance the ability of researchers to evaluate the contribution of specific osteoblast lineage populations to skeletal development and hematopoiesis.

INTRODUCTION

Within the bone marrow, hematopoiesis is critically dependent upon a supportive microenvironment, or niche, comprising interactions between hematopoietic and non-hematopoietic cells. Among non-hematopoietic stromal cells, bone-forming osteoblasts of mesenchymal origin and their precursors are crucial

components of the bone marrow hematopoietic niche. Growing evidence indicates that cells at each stage of differentiation from mesenchymal stem cells to fully mature osteoblasts serve distinct functions in supporting hematopoiesis [1–6].

The stage-specificity of hematopoietic support likely derives from the unique production of cytokines and growth factors by cellular

populations at varying points of differentiation along the osteoblast lineage. However, clarification of the relative contributions of specific subsets of osteoblast lineage cells to hematopoietic niches is currently limited by two significant barriers: (a) the inability to prospectively distinguish osteoprogenitors, differentiating osteoblasts, and mature osteoblasts and to harvest them in large numbers, and (b) the lack of a rigorous *in vivo* model for assessment of osteogenic and hematopoietic-supporting potential of various cellular populations.

To circumvent these limitations, we have turned to pluripotent stem cells (PSCs) as a potential source of osteoblasts. PSCs are unique in their ability to both self-renew and give rise to differentiated tissues. They represent a potentially unlimited source of osteoblast lineage cells for localized bone repair and regeneration, as well as for disease modeling and drug screening for systemic skeletal diseases. One source of stem cell-derived osteoblasts is embryonic stem cells (ESCs), which are derived from the inner cell mass of the blastocyst [7–9] and can contribute to any tissue. ESCs have been differentiated into several different tissue types including neurons [10–12], cardiomyocytes [13, 14], and pancreatic progenitors [15]. ESCs have also been differentiated into osteoblasts by several laboratories. A typical protocol to direct the differentiation of mouse [16, 17] or human [18] ESCs into osteoblasts involves formation of embryoid bodies (EBs) that are subsequently disaggregated and plated in osteogenic medium containing ascorbic acid and β -glycerophosphate (reviewed in ref. 19). The addition of factors such as dexamethasone, retinoic acid, bone morphogenetic proteins, and vitamin D3 [20–24] as well as the use of three-dimensional scaffolds [25–31] have been reported to enhance osteogenic differentiation. While the inability to derive patient-matched ESC lines may hinder the use of ESCs in cellular transplantation, banks of ESC lines to match various human leukocyte antigen-types could potentially be generated [32].

As an alternative approach, a combination of only four transcription factors—Oct3/4, Sox2, c-Myc, and Klf4—can convert mouse fibroblasts into induced PSC (iPSC) [33]. Human iPSCs can similarly be derived from human fibroblasts [34]. The ability to derive patient-matched iPSCs from accessible somatic cells offers great potential for understanding disease mechanisms, screening for novel therapeutics, and developing cell-based regenerative therapies. As with ESCs, both mouse [35, 36] and human [37] iPSCs have been differentiated into osteoblasts using similar protocols (reviewed in ref. [19]). More recently, Kanke et al. have differentiated iPSCs into osteoblasts in a monolayer culture without EB formation via mesodermal intermediates using small molecule inhibitors [38]. Therefore, ESCs and iPSCs represent a renewable source of bone-forming osteoblasts with significant clinical implications for understanding osteoblast support of hematopoiesis as well as skeletal pathophysiology.

The success of stem cell-derived osteoblasts in regenerative applications will depend largely on their ability to recapitulate osteoblast function. A major barrier to the development of a source of osteoblasts for regenerative purposes is the lack of a rigorous method for evaluating the osteogenic potential of mesenchymal progenitors or osteoblast precursors. The differentiation of ESC and iPSCs into osteoblasts in culture is typically assayed by mineral deposition, alkaline

phosphatase activity, and expression of osteoblast genes [16–18, 21, 23, 24]. However, even under osteogenic conditions, the differentiation of stem cells can result in a heterogeneous mix of multiple cellular lineages, and the above assays can yield positive results even when only a small percentage of osteoblasts are present. Furthermore, these assays do not accurately predict the ability of stem cell-derived osteoblasts to form bone *in vivo* [27, 39]. Therefore, bone formation should be directly evaluated *in vivo*. Assays of osteogenic capacity typically rely on ectopic bone formation, for instance, by implantation under the skin or kidney capsule of syngeneic or immunodeficient mice, often combined with a carrier material [20, 25, 27, 28, 39–43], or by healing of a critical-size calvarial defect [31, 44] or burr-hole fracture [25, 30]. However, these assays do not determine the ability of stem cell-derived osteoblasts to contribute to normal endogenous bone formation.

In mice, hematopoietic stem cells can reconstitute the entire hematopoietic system following lethal irradiation [45]. Analogous experiments to assess the regenerative capacity of stem cells that give rise to the skeleton, however, cannot be performed for several reasons—the skeleton is composed of greater than 200 distinct bones, it is not possible to ablate the postnatal skeleton in a manner compatible with survival, and mesenchymal stem cells introduced into the circulation have not been shown definitively to engraft in the skeleton [46]. Since a mineralized skeleton is dispensable for survival during embryogenesis, this developmental period affords an opportunity to investigate the skeletal contributions of PSCs via a blastocyst chimera assay.

Therefore, we sought to develop a more physiologic assessment of PSC contribution to skeletal function *in vivo* by organ complementation. Organ complementation has been used to demonstrate that β cell function in mutant mice lacking a pancreas can be restored by contribution of wild-type (WT) stem cells [47], and we have recently used a similar approach to examine the contribution of PSCs to cardiac development [48]. Here, we report that PSCs can reconstitute skeletal elements and rescue bone marrow hematopoiesis *in vivo*. Based on cell ablation studies, we find that as little as 37.5% chimerism is sufficient to restore grossly normal skeletal development.

MATERIALS AND METHODS

Experimental Animals

Runx2^{-/-} mice [49, 50] and Osx1-Cre mice [51] have been described. ROSA26^{eGFP-DTA} mice were purchased from the Jackson Laboratory (Bar Harbor, ME, <https://www.jax.org/jax-mice-and-services>). All mice were examined at embryonic day 18.5 (E18.5) unless otherwise noted. Experimental animal protocols were approved by the Institutional Animal Care and Use Committee of Massachusetts General Hospital.

Skeletal Complementation

The derivation of the ESC and iPSC lines has previously been reported [48]. Runx2^{+/-} mice were mated to CD1 WT mice to generate F1 Runx2^{+CD1^{-/-}} mice. F1 Runx2^{+CD1^{-/-}} female mice were superovulated for timed matings to F1 Runx2^{+CD1^{-/-}} male mice. Embryos were staged by vaginal plugging of the

female, with noon on the day of appearance of the plug designated as E0.5. E3.5 blastocysts were harvested for injection with ESCs or iPSCs at passage less than 25.

For the osterix (*Osx*):diphtheria toxin A (DTA) study, *Osx1-Cre/+* mice were mated to *ROSA26^{eGFP-DTA}* (DTA) mice to generate enhanced green fluorescent protein (eGFP)⁺ embryos carrying either DTA/+ only (control) or *Osx1-Cre/+;DTA/+* (ablated) alleles. Unlabeled WT ESCs were injected into eGFP⁺ blastocyst-stage embryos from each group to generate chimeras. P5 through P20 unlabeled WT ESCs were microinjected into E3.5 blastocysts from superovulated DTA/+ females that had been mated to *Osx1-Cre/+* males. For both approaches, the injected blastocysts were subsequently transferred into the uterus of 2.5 days postcoitum pseudopregnant 6- to 8-week-old CD-1 foster mothers previously mated with vasectomized [52]. Chimeric embryos were recovered at E18.5.

Genotyping

Microsatellite markers are DNA loci with repeated short nucleotide sequences that can vary in length. We identified a microsatellite marker in the *Runx2* locus that differed in length based on genetic background (CD1 vs. C57BL/6) (Supporting Information Fig. S1A). We crossed *Runx2^{+/-}* males to CD1 females, and intercrossed the resulting F1 heterozygous mice, in which the WT *Runx2* allele is of CD1 background (*Runx2^{+CD1/-}*). In contrast, the injected ESC and iPSCs are of C57BL/6 origin. By polymerase chain reaction (PCR) genotyping for the presence of *Runx2* WT (CD1 or C57BL/6 background), *Runx2* null, and green fluorescent protein (GFP)/YFP alleles (Supporting Information Fig. S1B), we could distinguish the genotype of the original host blastocyst in resulting chimeric embryos with PSC contribution (Supporting Information Fig. S1C, S1D).

Genotyping was performed by polymerase chain reaction on tail genomic DNA. The following primers were used for genotyping: *Runx2* WT allele forward 5'-AGCGACGTGAGCCC GGTGGT-3', reverse 5'-CTCAATCGGGGCACTGCGGC-3'; *Runx2* null allele forward 5'-TACGGTATCGCCGCTCCCGATTCCG-3', reverse 5'-ATGATCTCCACCATGGTGCGGTTG-3'; GFP forward 5'-TCATCTGCACCACCGGCAAGC-3', reverse 5'-AGCAGGACCATGT GATCGCGC-3'; Cre forward 5'-CGCGGTCTGGCAGTAAAACTATC-3', reverse 5'-CCCACGTCAGTACGTGAGATATC-3'. Microsatellite analysis was performed with forward 5'-TAGGTATTTTGGCA CGCGCGC-3' and reverse 5'-GCGTAACTCTGGTCTCGA-3' primers. PCR amplification was performed at 94°C for 3 minutes, 30 cycles of 94°C for 45 seconds, 61°C for 30 seconds, 72°C for 30 seconds followed by 72°C for 6 minutes then hold at 4°C.

Flow Cytometry

Liver and spleen were homogenized to obtain single cells. Following addition of propidium iodide to gate out dead cells, flow cytometric cell counting was performed on a FACSCalibur or FACSAria II flow cytometer (BD Biosciences, San Jose, CA, <http://www.bdbiosciences.com/us/home>) using CellQuest v3.3 software (BD Biosciences, San Jose, CA, <http://www.bdbiosciences.com/us/home>). Doublet discrimination and exclusion was performed by gating cells according to their forward scatter height (FSC-H) versus forward scatter width (FSC-W) and side scatter height (SSC-H) versus side scatter width (SSC-W)

distributions. To determine the proportion of eGFP⁺/eGFP⁻ cells in each tissue sample, the data were analyzed with FlowJo v7.6 software (FlowJo, LLC Ashland, OR, <https://www.flowjo.com>).

Skeletal Preparations

Skeletons were fixed in 95% ethanol, then stained overnight in 0.015% alcian blue in acetic acid/ethanol. Soft tissues were cleared in 1% KOH, then stained overnight in 0.01% alizarin red. Percentage mineralization was calculated by measuring the area of alizarin red staining using Fiji image analysis software [53].

Histology and Immunohistochemistry

Mouse limbs were snap frozen in liquid nitrogen and stored at -80°C until used. Undecalcified frozen bones were mounted on OCT medium and 10 μm slices were cut on a Leica CM1850 cryostat. Frozen sections were fixed in 4% paraformaldehyde for 10 minutes at room temperature (RT). After washing with phosphate-buffered saline (PBS), endogenous biotin was blocked using the Avidin/Biotin Blocking System (BioLegend). Sections were blocked in PBS with 10% normal donkey serum for 1 hour at RT, and then stained overnight at 4°C with chicken anti-GFP (Aves) and rat anti-CD45 biotin (BioLegend) antibodies. After washing with PBS, sections were stained for 1 hour at RT with donkey anti-chicken CF488A (Sigma-Aldrich) and Alexa Fluor 647 Streptavidin (BioLegend). Nuclei were counterstained with 4',6-diamidino-2-phenylindole (Sigma-Aldrich). Images were taken with Zeiss LSM780 confocal microscope.

RESULTS

To evaluate the ability of PSCs to contribute to skeletal development during embryogenesis, we used an organ complementation approach. *Runx2/Cbfa1* is a transcription factor that is absolutely required for osteoblast maturation [54]; *Runx2^{-/-}* mice fail to form a mineralized skeleton [50, 55]. In chimeric embryos resulting from the introduction of GFP⁺ or YFP⁺ WT PSCs into *Runx2^{-/-}* blastocysts, we reasoned that only PSCs expressing WT *Runx2* could contribute to the formation of a mineralized skeleton (Fig. 1A). To determine the genotype of the host blastocyst, we developed a microsatellite assay to distinguish the origin of WT alleles (host vs. injected PSCs) (Supporting Information Fig. S1). While *Runx2* is not required for survival during early embryogenesis, *Runx2^{-/-}* mice die of perinatal respiratory failure [50, 55]. Because we anticipated a small number of *Runx2*-deficient embryos with substantial PSC contribution and did not want to lose these mice to perinatal lethality, we therefore analyzed all embryos before delivery at E18.5. We tested several lines of GFP/YFP-labeled ESC and iPSC lines (Table 1) and found the highest contributions with V6.5 SA-eGFP⁺ ESCs (67% embryos with contribution) and TTF-R21-6 YFP⁺ iPSCs (34.9% embryos with contribution). The overall frequency of *Runx2^{-/-}* embryos was 22.9%–23.8% (Table 1), as expected based on Mendelian inheritance.

We first examined *Runx2^{-/-}* blastocysts injected with eGFP⁺ ESCs (Fig. 1B). Alizarin staining of skeletal preparations highlights areas of mineralization. In the control embryo by E18.5, there was abundant mineralization of the skull, ribs,

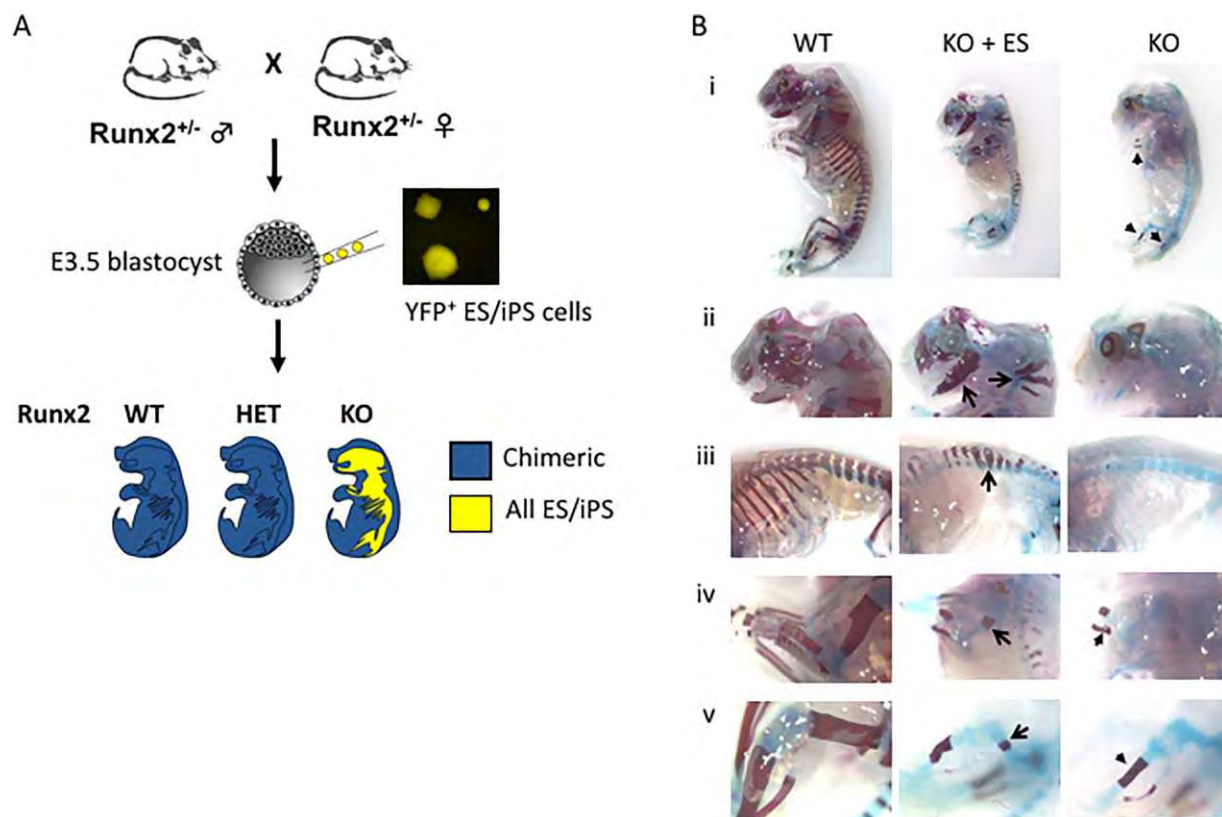


Figure 1. Skeletal complementation with pluripotent stem cells. **(A):** In chimeric embryos resulting from $Runx2^{-/-}$ blastocysts injected with wild-type (WT) stem cells, the mineralized skeleton will be entirely derived from stem cells. **(B):** Skeletal preparation of WT (left), $Runx2^{-/-}$ (knockout [KO], right) and embryonic stem cell-injected KO blastocyst (KO + ESC) E18.5 embryos (i). WT (left panels) embryo reveals normal mineralization of the head (ii), ribs and vertebrae (iii), forelimb (iv), and hindlimb (v) as highlighted by alizarin red staining. KO embryos (right panels) exhibit minimal mineralization of the ulna, radius, and tibia (arrowheads in i). In chimeric embryos derived from KO blastocysts injected with WT embryonic stem cells, patchy mineralization is observed in the skull, maxilla, mandible (arrows, panel ii), vertebrae (arrows, panels ii and iii), humerus (arrow, panel iv) and femur (arrow, panel v). Abbreviations: ESC, embryonic stem cell; HET, heterozygous; iPSC, induced pluripotent stem cell; KO, knockout; WT, wild type.

Table 1. Pluripotent stem cell lines

Injected line	No. injected	No. with stem cell contribution (%)	No. $Runx2^{-/-}$ (%)	No. $Runx2^{-/-}$ with contribution (%)
Embryonic stem cell lines				
RN23	22	0	4 (18.2)	0
RN21G3	5	0	2 (40)	0
YFP ESC	10	1 (10)	3 (30)	0
eYFP4	10	0	3 (30)	0
eYFP6	17	1 (5.9)	2 (11.8)	0
eYFP8	1	0	1 (100)	0
eYFP11	18	0	3 (16.7)	0
eYFP12	101	32 (31.7)	26 (25.7)	8 (7.9)
SA-GFP	91	61 (67)	19 (20.9)	15 (16.5)
Total	275	95 (34.5)	63 (22.9)	23 (8.4)
Induced pluripotent stem cell lines				
Nkx-z35	37	4 (10.8)	2 (5.4)	0
Nk5-2	28	0	6 (21.4)	0
YFP iPSC	17	2 (11.8)	2 (11.8)	0
iYFPLz2	85	29 (34.1)	11 (12.9)	3 (3.5)
TTF-R21-6	341	119 (34.9)	100 (29.3)	38 (11.1)
Total	508	154 (30.3)	121 (23.8)	41 (8.1)

vertebral column, and long bones. In contrast, the $Runx2^{-/-}$ embryo exhibited minimal mineralization only in the mid-shaft of distal long bones (radius/ulna and tibia/fibula) due to

mineralization of chondrocytes (Fig. 1Bi, iv, v); as reported previously, no mineralization was seen in the skull, mandible, humerus, or femur [55]. In a partially rescued chimeric embryo derived from a $Runx2^{-/-}$ host, patchy mineralization was observed in the skull, mandible, maxilla, vertebrae, and proximal long bones (humerus and femur) (Fig. 1B). We observed similar patchy contribution of YFP^{+} iPSCs in chimeric embryos (data not shown).

To quantitate the contribution of GFP^{+} ESCs to chimeric embryos, we performed flow cytometry analysis for GFP expression in the liver and the spleen. There was good correlation between the frequency of GFP^{+} ESC-derived cells in liver and spleen ($R^2 = 0.955$, Fig. 2A), and increasing GFP frequency correlated with increasing GFP visualized in the skin by whole-mount fluorescence (Fig. 2B). Moreover, as stem cell contribution increased, skeletal morphology and mineralization improved ($R^2 = 0.801$, Fig. 2C, 2D). Similar findings were observed with chimeras derived from iPSC injections ($R^2 = 0.747$, Fig. 3).

During embryonic development, hematopoiesis initiates in the yolk sac, then migrates to the aorta-gonad-mesonephros region, fetal liver, and spleen before ultimately taking up residence in the bone marrow perinatally [56]. $Runx2^{-/-}$ mice lack a bone marrow cavity, and therefore hematopoiesis is sustained in extramedullary sites such as the spleen [57]. In

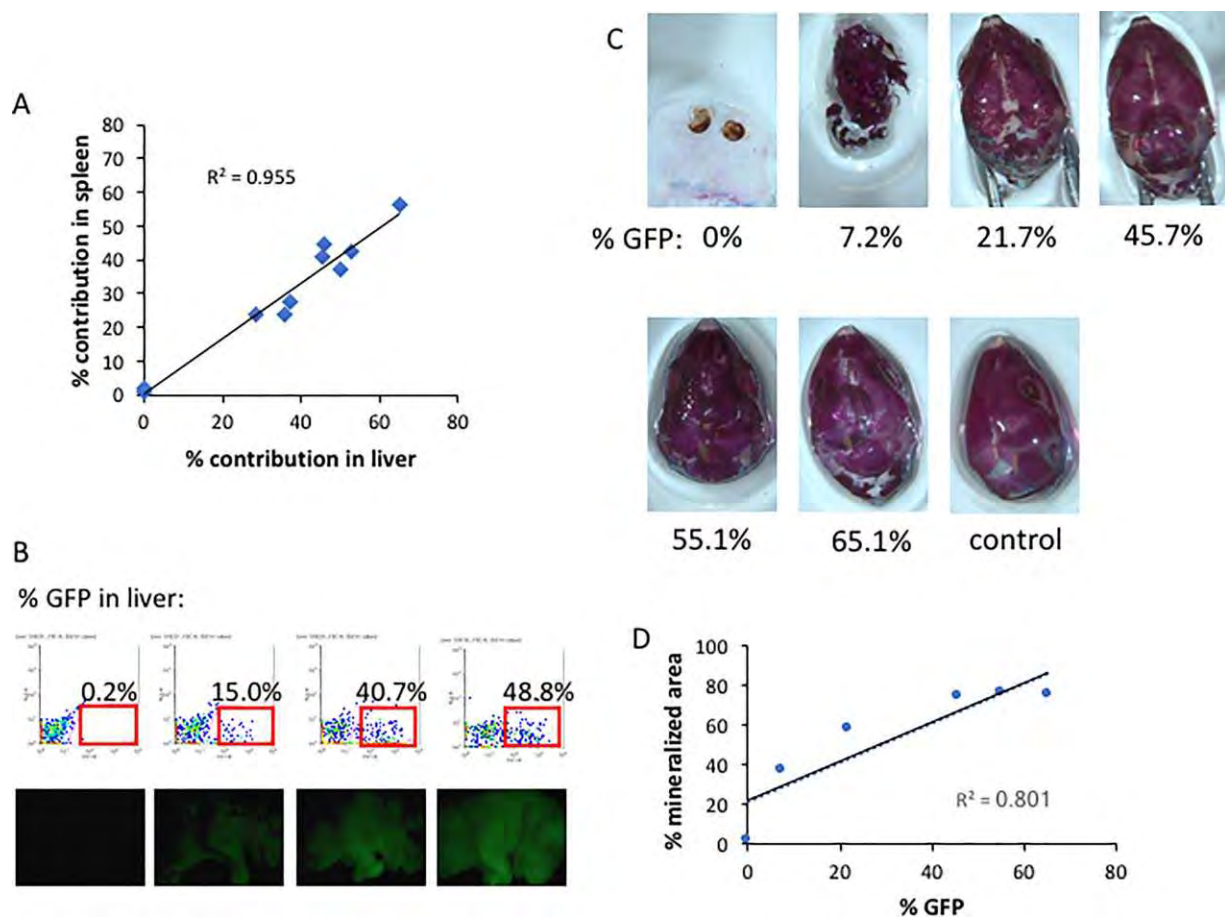


Figure 2. Embryonic stem cell (ESC) contribution in chimeric embryos. **(A):** The frequency of green fluorescent protein (GFP⁺) cells in the liver by flow cytometry correlates with the frequency of GFP⁺ in the spleen in chimeric embryos. **(B):** Representative flow cytometry profiles for percentage GFP expression in the liver, with corresponding whole mount images of GFP fluorescence shown below each panel. **(C):** Skeletal preparations of the skull reveal increasing rescue of skull mineralization with increasing ESC contribution. A control skull from a Runx2 wild-type embryo is shown for reference. **(D):** Quantitation of the percentage mineralized area of each skull as a function of percentage GFP contribution in the liver. Abbreviation: GFP, green fluorescent protein.

the humerus of Runx2^{-/-}, the entire skeletal element consists only of chondrocytes with no bone marrow cavity (Fig. 4A). In contrast, in a chimeric embryo with approximately 15% contribution (estimated proportion of GFP⁺ cells) from stem cells, hematopoietic cells were identifiable within the bone marrow cavity (Fig. 4B). Stem cell contribution exceeding 50% appears to restore a near-normal bone marrow cavity in Runx2^{-/-} blastocyst-derived chimeric embryos (Fig. 4C, 4D). To confirm that hematopoietic cells are present with the bone marrow cavities of chimeric embryos, we performed immunohistochemical staining for the hematopoietic cell marker CD45 (Fig. 4E). We found that the majority of CD45⁺ hematopoietic cells are derived from the host blastocyst, although stem cell-derived (GFP⁺) hematopoietic cells ranged in frequency from 5% to 40%. The frequency of GFP⁺ hematopoietic cells did not appear to correlate with the overall degree of stem cell contribution as assessed by GFP frequency in the liver (Fig. 4F). Thus, the presence of a fraction of PSC-derived progeny can rescue the bone marrow hematopoietic microenvironment in vivo.

In the skull, the degree of mineralization seemed to correlate with the proportion of PSCs up until approximately 50% contribution, above which skull mineralization appeared

grossly normal (Figs. 2C, 3B). Ossification of calvarial bones occurs by intramembranous bone formation, in which mesenchymal progenitors give rise directly to osteoblasts. In contrast, bones of the axial and appendicular skeleton are formed by endochondral ossification, in which skeletal elements form via a cartilage template intermediate [58]. In the ribs of Runx2^{-/-} embryos injected with either ESC or iPSCs, we noticed that rescue of rib mineralization always appeared to initiate in the same proximal location and extended only for limited distances (Fig. 5). During endochondral bone formation, chondrocyte differentiation and hypertrophy are followed by apoptosis of hypertrophic chondrocytes, which in turn triggers vascular invasion bringing osteoprogenitors that will form trabecular and cortical bone [58, 59]. Runx2 is expressed in prehypertrophic chondrocytes and required for chondrocyte hypertrophy and vascular invasion [60, 61]. In the ribs, vascular invasion initiates at the proximal end between E15.5 and E16.5, at the same location where we found partial mineralization in PSC-injected Runx2^{-/-} chimeric embryos (Supporting Information Fig. S2). Our observations in the ribs (Fig. 5) raised the possibility that persistence of Runx2-deficient chondrocytes that are unable to hypertrophy and undergo apoptosis might hinder the expansion of PSC-

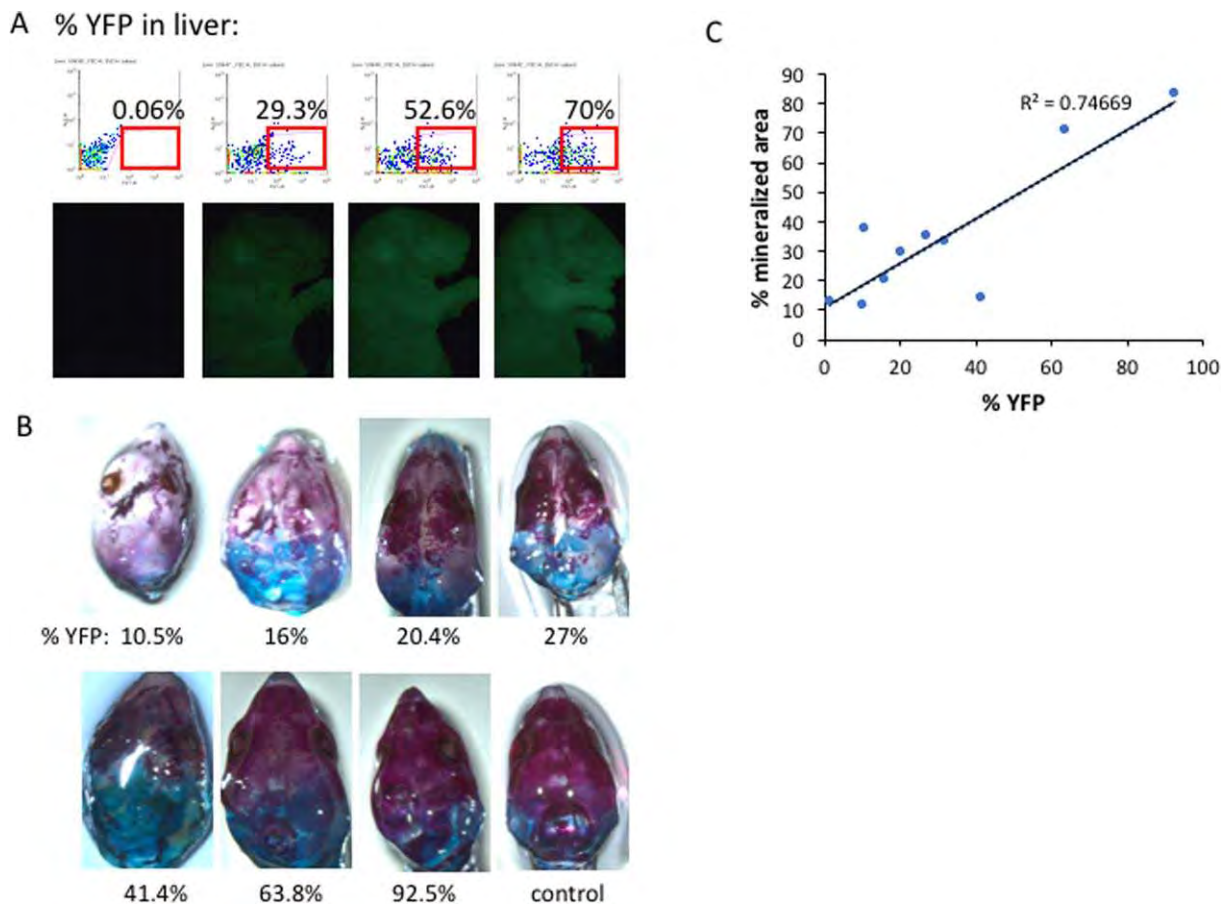


Figure 3. Induced pluripotent stem cell (iPSC) contribution in chimeric embryos. **(A):** Representative flow cytometry profiles for percentage YFP expression in the liver, with corresponding whole mount images of YFP fluorescence shown below each panel. **(B):** Skeletal preparations of the skull reveal increasing rescue of skull mineralization with increasing iPSC contribution. A control skull from a Runx2 wild-type embryo is shown for reference. **(C):** Quantitation of the percentage mineralized area of each skull as a function of percentage yellow fluorescent protein contribution in the liver. Abbreviation: YFP, yellow fluorescent protein.

derived osteoblasts in endochondral bones. Since osteoblast progenitors have migratory potential only during early differentiation [62], any obstacle to migration might limit the domain of mature osteoblasts and ossification within a skeletal element.

To determine whether clearing skeletal elements of Runx2-deficient late hypertrophic chondrocytes and osteoprogenitors might enable WT PSCs to contribute to a greater proportion of the skeleton, we developed a cellular ablation model. *Osx1-Cre* mice expressing Cre recombinase in late hypertrophic chondrocytes and osteoprogenitors under control of the *Osx* promoter [51] were crossed to *ROSA26-flox-eGFP-flox-DTA* mice (Fig. 6A). In response to *Osx*-driven Cre expression during skeletal development, expression of DTA will ablate *Osx*-expressing cells. In mice carrying both *Osx1-Cre* and DTA transgenes, skeletal elements were absent in the hindlimb (Fig. 6B). We screened E3.5 blastocysts for the presence of the DTA allele by GFP expression, of which 50% are expected to also carry the *Osx1-Cre* transgene, and injected these with WT (GFP-negative) ESCs. In the resulting chimeric mice, the contribution of stem cells can be estimated by the percentage of GFP-negative cells in the liver. In *Osx1-Cre/+; DTA/+* double transgenic mice, increasing

rescue of skeletal formation was noted with increased stem cell contribution. In the skeleton, ESC contributions of 20% or less resulted in minimal skeletogenesis, while contributions above 37.5% resulted in significant restoration of the skeleton as assessed by skeletal preparations (Fig. 6C). Therefore, ESC- and iPSC-derived osteoblasts can reconstitute the hematopoietic niche in vivo, and above a contribution threshold of ~40%, can restore near normal gross skeletal morphology.

DISCUSSION

Osteoblasts are essential component of skeletal tissues, vital for bone formation and repair. Osteoblast lineage cells are also essential to the support of hematopoiesis in the bone marrow microenvironment. Because osteoblasts are situated in mineralized tissue, the ability to harvest and investigate large populations of osteoblast lineage cells at defined stages of differentiation has so far been limited. Here, we demonstrate with skeletal complementation models that PSCs can contribute robustly to skeletal development during embryogenesis, and can compensate for the absence of osteoblasts to restore the hematopoietic niche.

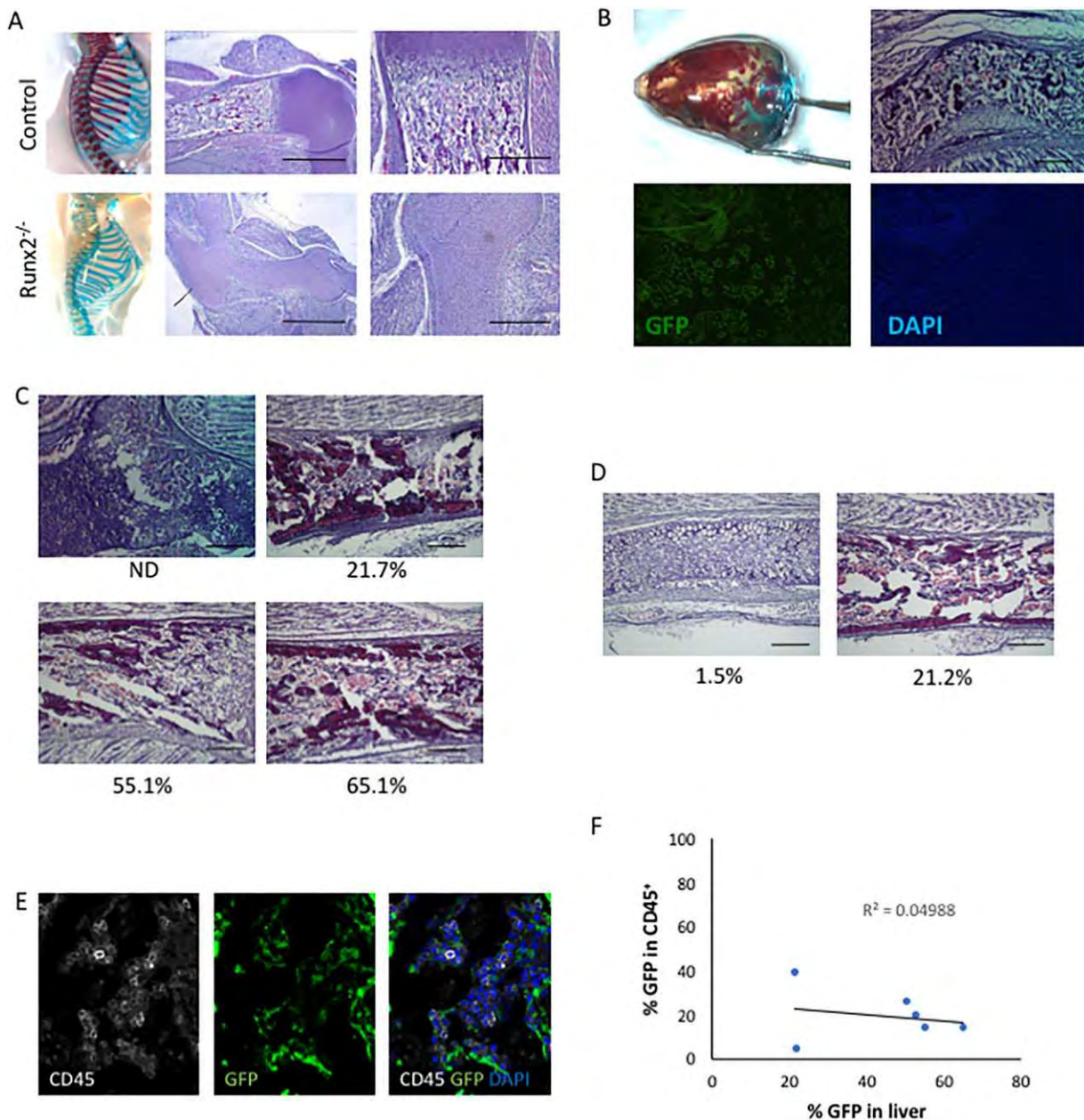


Figure 4. Rescue of bone marrow hematopoiesis by stem cell-derived osteoblasts. **(A):** Skeletal preparations and hematoxylin- and eosin-stained sections of the proximal humerus of E18.5 control (upper) and $Runx2^{-/-}$ (lower) embryos. Note the absence of hematopoietic bone marrow in the $Runx2^{-/-}$ humerus. Scale bar = 1 mm (middle panels) or 200 μ m (right panels). **(B):** Skull skeletal preparation demonstrating partial rescue in a $Runx2^{-/-}$ host blastocyst injected with stem cells. Histological analysis reveals the formation of a bone marrow cavity. Green fluorescent protein (GFP) expression confirms chimeric contribution of stem cells. Scale bar = 200 μ m. **(C):** Histological analyses of humeri of $Runx2^{-/-}$ blastocysts injected with embryonic stem cells (ESCs). ESC contribution (%) as determined by flow cytometry is provided under each panel. Scale bar = 200 μ m. **(D):** Histological analyses of humeri of $Runx2^{-/-}$ blastocysts injected with induced pluripotent stem cells. iPSC contribution (%) as determined by flow cytometry is provided under each panel. Scale bar = 200 μ m. **(E):** Immunohistochemical staining for CD45 (white), GFP (green), and nuclei (4',6-diamidino-2-phenylindole, blue) reveals CD45⁺ hematopoietic cells in the bone marrow. **(F):** The frequency of CD45⁺ hematopoietic cells that are stem cell-derived (GFP⁺) does not correlate with the percentage GFP contribution in the liver. Abbreviations: DAPI, 4',6-diamidino-2-phenylindole; GFP, green fluorescent protein.

We demonstrate that in $Runx2^{-/-}$ mice, which fail to form a mineralized skeleton or hematopoietic bone marrow, introduction of WT PSCs at the blastocyst stage partially rescues development of skeletal elements and can support the formation of hematopoietic bone marrow as demonstrated by the expression of CD45. As expected, the resulting hematopoietic cells are chimeric and can be of either host blastocyst or

injected stem cell origin. Due to the limited numbers of chimeric embryos with >40% PSC contribution to $Runx$ -deficient embryos, the functional nature of the hematopoietic cells was not evaluated. Additional studies are needed to more carefully examine the phenotype and function of rescued hematopoietic cells by flow cytometry, colony forming assays, and/or transplantation. Also of interest is whether substantial PSC

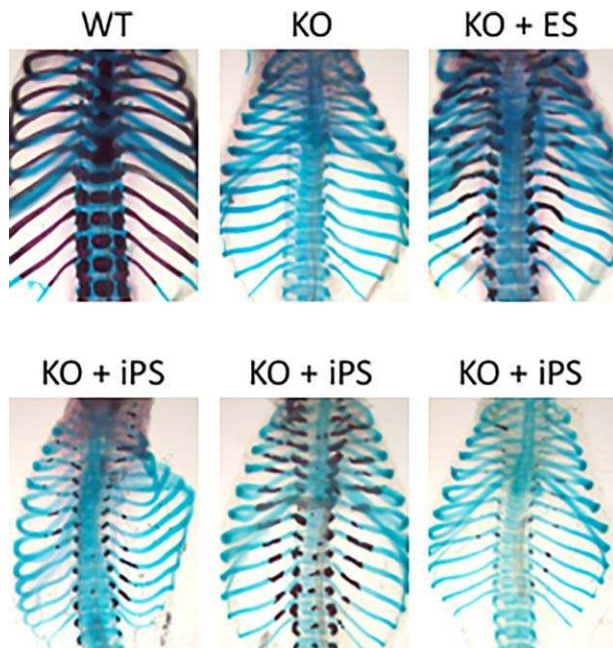


Figure 5. Stereotypical rescue of rib mineralization by skeletal complementation. Skeletal preparations of wild type and knockout ribs. In ribs of chimeric embryos rescued with ESC or induced pluripotent stem cell injection, mineralization is detected in proximal ends of thoracic ribs. Abbreviations: ESC, embryonic stem cell; KO, knockout; iPSC, induced pluripotent stem cell; WT, wild type.

contribution results in survival of Runx2-deficient mice past the perinatal period.

PSCs can contribute to both endochondral and intramembranous bone formation by skeletal complementation of Runx2-deficient embryos. Intramembranous ossification occurs without a cartilage intermediate, and the mineralization of the skull clearly correlates with the degree of PSC contribution. In contrast, in the ribs, which develop by endochondral ossification, our findings of limited rescue of mineralization in the ribs might reflect persistent Runx2-deficient cartilage template. Future studies will examine in detail whether the efficiency of skeletal rescue differs in endochondral vs intramembranous bones.

To examine the contribution of PSCs in the absence of a persistent cartilage template, we developed a second model to ablate both hypertrophic chondrocytes and osteoblasts. In this DTA ablation model, we find that, as in the calvariae, contribution of >50% stem cells is sufficient to restore a grossly normal pattern of skeletal mineralization, while chimerism in the range of 20%–50% is associated with partial rescue. These are in line with our findings with organ complementation of cardiac development, where we have found in the heart that 40%–50% contribution was sufficient to restore normal cardiac development [48]. Therefore, both the heart and the skeleton can tolerate loss of up to 50% of contributing cells without gross defects in organogenesis.

There are several potential uses for these models. They can be used to examine the abilities of osteoblast lineage

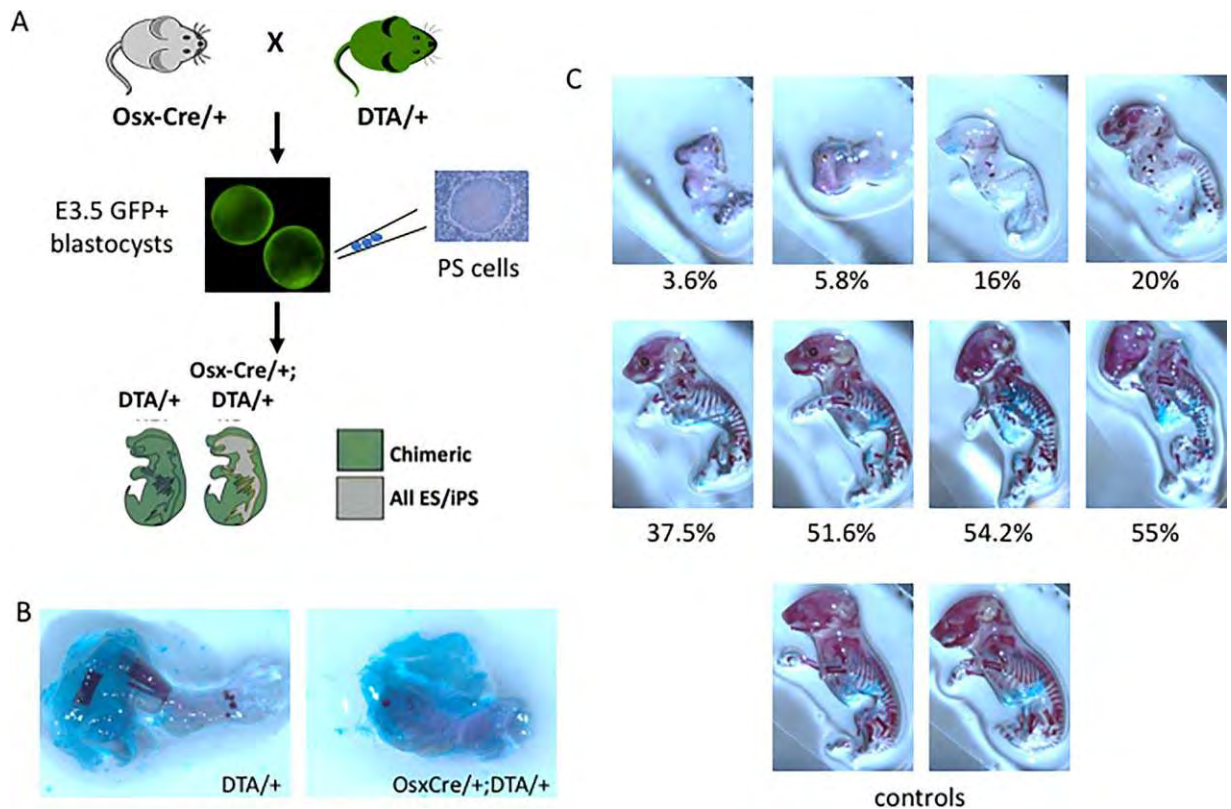


Figure 6. Skeletal complementation in an osteoprogenitor ablation model. **(A):** In chimeric embryos resulting from blastocysts expressing both *Osx1-Cre* and diphtheria toxin A (DTA) alleles and injected with wild-type pluripotent stem cells (PSCs), the mineralized skeleton will be entirely derived from PSC progenies. **(B):** Skeletal preparation of E18.5 hindlimb from *DTA/+* (left) and *OsxCre/+;DTA/+* embryos demonstrates near ablation of skeletal elements in the latter. **(C):** Increased stem cell contribution is associated with increasing normalization of the mineralized skeleton. Two control skeletons are shown for reference. Abbreviations: DTA, diphtheria toxin A; ESC, embryonic stem cell; GFP, green fluorescent protein; iPSC, induced pluripotent stem cell; PSC, pluripotent stem cell.

cells at defined stages of differentiation to contribute to the formation of a mineralized skeletal. We predict that while osteoprogenitors may contribute broadly to skeletal development, mature osteoblasts may have more restricted contribution due to their limited proliferative potential. Furthermore, since osteoblast lineage cells have unique roles in supporting hematopoiesis at specific stages of differentiation, we can now examine *in vivo* whether reconstitution of the hematopoietic marrow favors certain hematopoietic lineages depending on the stage of osteoblasts introduced. Future studies will explore these possibilities in greater detail and determine the relative efficiency of stem cell-derived osteoblast lineage cells to contribute to skeletal development.

CONCLUSION

In summary, we have demonstrated that pluripotent stem cells can contribute to bone formation and support of the bone marrow hematopoietic niche *in vivo*. We have developed two skeletal complementation assays that can be used to further study the contribution of osteoblast lineage cells to skeletal development and hematopoiesis.

REFERENCES

- Ding L, Morrison SJ. Haematopoietic stem cells and early lymphoid progenitors occupy distinct bone marrow niches. *Nature* 2013;495:231–235.
- Ding L, Saunders TL, Enikolopov G et al. Endothelial and perivascular cells maintain haematopoietic stem cells. *Nature* 2012;481:457–462.
- Fulzele K, Krause DS, Panaroni C et al. Myelopoiesis is regulated by osteocytes through G α -dependent signaling. *Blood* 2013;121:930–939.
- Greenbaum A, Hsu YM, Day RB et al. CXCL12 in early mesenchymal progenitors is required for haematopoietic stem-cell maintenance. *Nature* 2013;495:227–230.
- Panaroni C, Fulzele K, Saini V et al. PTH Signaling in osteoprogenitors is essential for B-lymphocyte differentiation and mobilization. *J Bone Miner Res* 2015;30:2273–2286.
- Rankin EB, Wu C, Khatri R et al. The HIF signaling pathway in osteoblasts directly modulates erythropoiesis through the production of EPO. *Cell* 2012;149:63–74.
- Evans MJ, Kaufman MH. Establishment in culture of pluripotential cells from mouse embryos. *Nature* 1981;292:154–156.
- Martin GR. Isolation of a pluripotent cell line from early mouse embryos cultured in medium conditioned by teratocarcinoma stem cells. *Proc Natl Acad Sci USA* 1981;78:7634–7638.
- Thomson JA, Itskovitz-Eldor J, Shapiro SS et al. Embryonic stem cell lines derived from human blastocysts. *Science* 1998;282:1145–1147.
- Carpenter MK, Inokuma MS, Denham J et al. Enrichment of neurons and neural precursors from human embryonic stem cells. *Exp Neurol* 2001;172:383–397.
- Schuldiner M, Eiges R, Eden A et al. Induced neuronal differentiation of human

embryonic stem cells. *Brain Res* 2001;913:201–205.

12 Zhang SC, Wernig M, Duncan ID et al. *In vitro* differentiation of transplantable neural precursors from human embryonic stem cells. *Nat Biotechnol* 2001;19:1129–1133.

13 Kehat I, Gepstein A, Spira A et al. High-resolution electrophysiological assessment of human embryonic stem cell-derived cardiomyocytes: A novel *in vitro* model for the study of conduction. *Circ Res* 2002;91:659–661.

14 Xu C, Police S, Rao N et al. Characterization and enrichment of cardiomyocytes derived from human embryonic stem cells. *Circ Res* 2002;91:501–508.

15 Assady S, Maor G, Amit M et al. Insulin production by human embryonic stem cells. *Diabetes* 2001;50:1691–1697.

16 Buttery LD, Bourne S, Xynos JD et al. Differentiation of osteoblasts and *in vitro* bone formation from murine embryonic stem cells. *Tissue Eng* 2001;7:89–99.

17 Phillips BW, Belmonte N, Vernochet C et al. Compactin enhances osteogenesis in murine embryonic stem cells. *Biochem Biophys Res Commun* 2001;284:478–484.

18 Sottile V, Thomson A, McWhir J. *In vitro* osteogenic differentiation of human ES cells. *Cloning Stem Cells* 2003;5:149–155.

19 Wu JY. Pluripotent stem cells and skeletal regeneration—Promise and potential. *Curr Osteoporos Rep* 2015;13:342–350.

20 Bielby RC, Boccaccini AR, Polak JM et al. *In vitro* differentiation and *in vivo* mineralization of osteogenic cells derived from human embryonic stem cells. *Tissue Eng* 2004;10:1518–1525.

21 Bourne S, Polak JM, Hughes SP et al. Osteogenic differentiation of mouse embryonic stem cells: Differential gene expression analysis by cDNA microarray and purification of osteoblasts by cadherin-11 magnetically activated cell sorting. *Tissue Eng* 2004;10:796–806.

ACKNOWLEDGMENTS

We thank the Harvard Stem Cell Institute flow cytometry core and the MGH Center for Comparative Medicine staff for care of the mice. This worked was supported by the Harvard Stem Cell Institute (to S.M.W. and J.Y.W.) as well as by National Institutes of Health Grants DP2OD004411 (to S.M.W.) and DP2OD008466 (to J.Y.W.).

AUTHOR CONTRIBUTIONS

R.C., J.O., A.K.R., and T.K.: collection and/or assembly of data, data analysis and interpretation; S.M.W.: conception and design, financial support, provision of study material, data analysis and interpretation, manuscript writing; J.Y.W.: conception and design, financial support, provision of study material, collection and/or assembly of data, data analysis and interpretation, manuscript writing, final approval of manuscript

DISCLOSURE OF POTENTIAL CONFLICTS OF INTEREST

The authors indicated no potential conflicts of interest.

22 Camargos BM, Tavares RL, Del Puerto HL et al. BMP-4 increases activin A gene expression during osteogenic differentiation of mouse embryonic stem cells. *Growth Factors* 2015;33:133–138.

23 Zur Nieden NI, Kempka G, Ahr HJ. *In vitro* differentiation of embryonic stem cells into mineralized osteoblasts. *Differentiation* 2003;71:18–27.

24 Zur Nieden NI, Price FD, Davis LA et al. Gene profiling on mixed embryonic stem cell populations reveals a biphasic role for beta-catenin in osteogenic differentiation. *Mol Endocrinol* 2007;21:674–685.

25 Alfred R, Taiani JT, Krawetz RJ et al. Large-scale production of murine embryonic stem cell-derived osteoblasts and chondrocytes on microcarriers in serum-free media. *Biomaterials* 2011;32:6006–6016.

26 Evans ND, Gentleman E, Chen X et al. Extracellular matrix-mediated osteogenic differentiation of murine embryonic stem cells. *Biomaterials* 2010;31:3244–3252.

27 Kuznetsov SA, Cherman N, Robey PG. *In vivo* bone formation by progeny of human embryonic stem cells. *Stem Cells Dev* 2011;20:269–287.

28 Marolt D, Campos IM, Bhumiratana S et al. Engineering bone tissue from human embryonic stem cells. *Proc Natl Acad Sci USA* 2012;109:8705–8709.

29 Rutledge K, Cheng Q, Pryzhkova M et al. Enhanced differentiation of human embryonic stem cells on extracellular matrix-containing osteomimetic scaffolds for bone tissue engineering. *Tissue Eng Part C Methods* 2014;20:865–874.

30 Taiani JT, Krawetz RJ, Yamashita A et al. Embryonic stem cells incorporate into newly formed bone and do not form tumors in an immunocompetent mouse fracture model. *Cell Transplant* 2013;22:1453–1462.

31 Xin X, Jiang X, Wang L et al. A site-specific integrated Col2.3 GFP reporter

identifies osteoblasts within mineralized tissue formed *in vivo* by human embryonic stem cells. *STEM CELLS TRANSLATIONAL MEDICINE* 2014;3:1125–1137.

32 Yamanaka S. A fresh look at iPS cells. *Cell* 2009;137:13–17.

33 Takahashi K, Yamanaka S. Induction of pluripotent stem cells from mouse embryonic and adult fibroblast cultures by defined factors. *Cell* 2006;126:663–676.

34 Yu J, Vodyanik MA, Smuga-Otto K et al. Induced pluripotent stem cell lines derived from human somatic cells. *Science* 2007;318:1917–1920.

35 Li F, Bronson S, Niyibizi C. Derivation of murine induced pluripotent stem cells (iPS) and assessment of their differentiation toward osteogenic lineage. *J Cell Biochem* 2010;109:643–652.

36 Tashiro K, Inamura M, Kawabata K et al. Efficient adipocyte and osteoblast differentiation from mouse induced pluripotent stem cells by adenoviral transduction. *STEM CELLS* 2009;27:1802–1811.

37 Lian Q, Zhang Y, Zhang J et al. Functional mesenchymal stem cells derived from human induced pluripotent stem cells attenuate limb ischemia in mice. *Circulation* 2010;121:1113–1123.

38 Kanke K, Masaki H, Saito T et al. Step-wise differentiation of pluripotent stem cells into osteoblasts using four small molecules under serum-free and feeder-free conditions. *Stem Cell Reports* 2014;2:751–760.

39 Phillips MD, Kuznetsov SA, Cherman N et al. Directed differentiation of human induced pluripotent stem cells toward bone and cartilage: *In vitro* versus *in vivo* assays. *STEM CELLS TRANSLATIONAL MEDICINE* 2014;3:867–878.

40 Bilousova G, Jun Du H, King KB et al. Osteoblasts derived from induced pluripotent stem cells form calcified structures in scaffolds both *in vitro* and *in vivo*. *STEM CELLS* 2011;29:206–216.

41 de Peppo GM, Marcos-Campos I, Kahler DJ et al. Engineering bone tissue substitutes

from human induced pluripotent stem cells. *Proc Natl Acad Sci USA* 2013;110:8680–8685.

42 Jin GZ, Kim TH, Kim JH et al. Bone tissue engineering of induced pluripotent stem cells cultured with macrochanneled polymer scaffold. *J Biomed Mater Res A* 2013;101:1283–1291.

43 Kim K, Zhao R, Doi A et al. Donor cell type can influence the epigenome and differentiation potential of human induced pluripotent stem cells. *Nat Biotechnol* 2011;29:1117–1119.

44 Jukes JM, Both SK, Leusink A et al. Endochondral bone tissue engineering using embryonic stem cells. *Proc Natl Acad Sci USA* 2008;105:6840–6845.

45 Spangrude GJ, Heimfeld S, Weissman IL. Purification and characterization of mouse hematopoietic stem cells. *Science* 1988;241:58–62.

46 Karp JM, Leng Teo GS. Mesenchymal stem cell homing: The devil is in the details. *Cell Stem Cell* 2009;4:206–216.

47 Kobayashi T, Yamaguchi T, Hamanaka S et al. Generation of rat pancreas in mouse by interspecific blastocyst injection of pluripotent stem cells. *Cell* 2010;142:787–799.

48 Sturzu AC, Rajarajan K, Passer D et al. Fetal mammalian heart generates a robust compensatory response to cell loss. *Circulation* 2015;132:109–121.

49 Hirai T, Kobayashi T, Nishimori S et al. Bone is a major target of PTH/PTHrP receptor signaling in regulation of fetal blood calcium homeostasis. *Endocrinology* 2015;156:2774–2780.

50 Otto F, Thornell AP, Crompton T et al. *Cbfa1*, a candidate gene for cleidocranial dysplasia syndrome, is essential for osteoblast differentiation and bone development. *Cell* 1997;89:765–771.

51 Rodda SJ, McMahon AP. Distinct roles for Hedgehog and canonical Wnt signaling in specification, differentiation and maintenance of osteoblast progenitors. *Development* 2006;133:3231–3244.

52 Hogan BL, Bedington RS, Constantini F et al. *Manipulating the Mouse Embryo. A*

Laboratory Manual. 2nd ed. Cold Spring Harbor Laboratory Press, NY 1994.

53 Schindelin J, Arganda-Carreras I, Frise E et al. Fiji: An open-source platform for biological-image analysis. *Nat Methods* 2012;9:676–682.

54 Ducy P, Zhang R, Geoffroy V et al. *Osf2/Cbfa1*: A transcriptional activator of osteoblast differentiation. *Cell* 1997;89:747–754.

55 Komori T, Yagi H, Nomura S et al. Targeted disruption of *Cbfa1* results in a complete lack of bone formation owing to maturational arrest of osteoblasts. *Cell* 1997;89:755–764.

56 Orkin SH, Zon LI. Hematopoiesis: An evolving paradigm for stem cell biology. *Cell* 2008;132:631–644.

57 Deguchi K, Yagi H, Inada M et al. Excessive extramedullary hematopoiesis in *Cbfa1*-deficient mice with a congenital lack of bone marrow. *Biochem Biophys Res Commun* 1999;255:352–359.

58 Kronenberg HM. Developmental regulation of the growth plate. *Nature* 2003;423:332–336.

59 Maes C, Kobayashi T, Selig MK et al. Osteoblast precursors, but not mature osteoblasts, move into developing and fractured bones along with invading blood vessels. *Dev Cell* 2010;19:329–344.

60 Takarada T, Hinoi E, Nakazato R et al. An analysis of skeletal development in osteoblast-specific and chondrocyte-specific runt-related transcription factor-2 (*Runx2*) knockout mice. *J Bone Miner Res* 2013;28:2064–2069.

61 Takeda S, Bonnamy JP, Owen MJ et al. Continuous expression of *Cbfa1* in nonhypertrophic chondrocytes uncovers its ability to induce hypertrophic chondrocyte differentiation and partially rescues *Cbfa1*-deficient mice. *Genes Dev* 2001;15:467–481.

62 Maes C, Kobayashi T, Kronenberg HM. A novel transgenic mouse model to study the osteoblast lineage *in vivo*. *Ann NY Acad Sci* 2007;1116:149–164.



See www.StemCells.com for supporting information available online.

RESEARCH ARTICLE

Adipose-derived stem cells attenuate pulmonary microvascular hyperpermeability after smoke inhalation

Koji Ihara^{1,2,3*}, Satoshi Fukuda¹, Baigalmaa Enkhtaivan¹, Raul Trujillo¹, Dannelys Perez-Bello¹, Christina Nelson¹, Anita Randolph¹, Suzan Alharbi¹, Hira Hanif¹, David Herndon⁴, Donald Prough¹, Perenlei Enkhbaatar¹

1 Department of Anesthesiology, The University of Texas Medical Branch, Galveston, Texas, United States of America, **2** Department of Plastic and Reconstructive Surgery, Kagoshima City Hospital, Kagoshima, Japan, **3** Department of Plastic and Reconstructive Surgery, Tokyo Women's Medical School, Tokyo, Japan, **4** Department of Surgery, Shriners Hospital for Children, Galveston, Texas, United States of America

* ihara.koji@twmu.ac.jp



OPEN ACCESS

Citation: Ihara K, Fukuda S, Enkhtaivan B, Trujillo R, Perez-Bello D, Nelson C, et al. (2017) Adipose-derived stem cells attenuate pulmonary microvascular hyperpermeability after smoke inhalation. *PLoS ONE* 12(10): e0185937. <https://doi.org/10.1371/journal.pone.0185937>

Editor: Yu Ru Kou, National Yang-Ming University, TAIWAN

Received: June 18, 2017

Accepted: September 21, 2017

Published: October 5, 2017

Copyright: © 2017 Ihara et al. This is an open access article distributed under the terms of the [Creative Commons Attribution License](https://creativecommons.org/licenses/by/4.0/), which permits unrestricted use, distribution, and reproduction in any medium, provided the original author and source are credited.

Data Availability Statement: All relevant data are within the paper and its Supporting Information files.

Funding: This study was supported by the Shriners of North America (grants SHC84050 and 85100). The funders had no role in study design, data collection and analysis, decision to publish, or preparation of the manuscript.

Competing interests: The authors have declared that no competing interests exist.

Abstract

Background

Pulmonary edema is a hallmark of acute respiratory distress syndrome (ARDS). Smoke inhalation causes ARDS, thus significantly increasing the mortality of burn patients. Adipose-derived stem cells (ASCs) exert potent anti-inflammatory properties. The goal of the present study was to test the safety and efficacy of ASCs, in a well-characterized clinically relevant ovine model of ARDS.

Methods

Female sheep were surgically prepared. ARDS was induced by cooled cotton smoke inhalation. Following injury, sheep were ventilated, resuscitated with lactated Ringer's solution, and cardiopulmonary hemodynamics were monitored for 48 hours in a conscious state. Pulmonary microvascular hyper-permeability was assessed by measuring lung lymph flow, extravascular lung water content, protein content in plasma and lung lymph fluid. Sheep were randomly allocated to two groups: 1) ASCs: infused with 200 million of ASCs in 200mL of PlasmaLyteA starting 1 hours post-injury, n = 5; 2) control, treated with 200mL of PlasmaLyteA in a similar pattern, n = 5.

Results

Lung lymph flow increased 9-fold in control sheep as compared to baseline. Protein in the plasma was significantly decreased, while it was increased in the lung lymph. The treatment with ASCs significantly attenuated these changes. Treatment with ASCs almost led to the reversal of increased pulmonary vascular permeability and lung water content. Pulmonary gas exchange was significantly improved by ASCs. Infusion of the ASCs did not negatively affect pulmonary artery pressure and other hemodynamic variables.

Conclusions

ASCs infusion was well tolerated. The results suggest that intravenous ASCs modulate pulmonary microvascular hyper-permeability and prevent the onset of ARDS in our experimental model.

Introduction

Acute respiratory distress syndrome (ARDS) is a severe form of acute lung injury caused by sepsis, pneumonia, trauma, severe burn, and smoke inhalation injury [1]. Although survival from ARDS has increased in recent years with the use of intensive supportive cares, such as lung-protective ventilation and fluid-conservative management, the mortality of ARDS patients is still high [1]. Due to the lack of specific treatment, smoke inhalation injury and ARDS are a major cause of morbidity and mortality in burn patients [2]. Pathophysiological changes in the lungs after smoke inhalation injury are characterized by increased pulmonary microvascular permeability, edema formation, and airway obstruction. Chemical components of smoke stimulate the release of neuropeptides from peripheral endings of sensory neurons within the airways to induce neurogenic inflammation. Plasma extravasation and oedema then result as secondary responses. Neurogenic inflammation results in narrowing of airway lumina, which is attributable to airway mucosal hyperaemia, formation of obstructive casts in the airway, and bronchospasm. These changes result in severe impairment of respiratory gas exchange [3].

Mesenchymal stem cells (MSCs) have been shown to be beneficial in many pathological conditions, such as myocardial infarction [4], graft versus host disease [5] and spinal cord injury [6]. Believed to be multipotent cells, MSCs are capable of differentiating into multi cell types i.e., adipocytes, chondrocytes and osteocytes [7]. In addition, they can also differentiate into a variety of cell lineages that form mesenchymal tissues, such as marrow stroma, muscle, cartilage, tendon, fat, and bone [8–10]. Other studies have shown that MSCs lead to improved clearance of alveolar fluid and have anti-inflammatory effects on host tissue in preclinical models of ARDS and sepsis [11]. To date, two clinical studies (Phase 1) on the safety of MSCs use in patients with ARDS have been successfully completed [12, 13], and recently, we have reported on the beneficial effects of clinical grade human bone marrow-derived MSCs in ovine models of ARDS induced by pneumonia/sepsis [14].

In the present study, we tested the hypothesis that intravenously administered adipose-derived stem cells (ASCs) effectively ameliorate the severity of pulmonary microvascular hyper-permeability in ovine models of ARDS induced by smoke inhalation.

Material and methods

Animal care and use

This study was approved by the Institutional Animal Care and Use Committee of the University of Texas Medical Branch (1308034) and conducted in compliance with the guidelines of the National Institutes of Health and the American Physiological Society for the care and use of laboratory animals.

Surgical preparation

Ten female Merino sheep weighing 30 ± 40 kg were surgically prepared 5 ± 7 days before the experiment. Under aseptic conditions, the animals were chronically instrumented with multiple vascular catheters for hemodynamic monitoring as previously described [15]. In brief, under isoflurane anesthesia (IsoSol, VEDCO, St. Joseph, MO) administered via endotracheal tube, a 7F Swan-Ganz thermodilution catheter (model 131F7, Edwards Critical Care Division, Irvine, CA) was inserted into the right jugular vein through a 9.0F Intro-Flex-Percutaneous Sheath Introducer (CENTURION, Williamston, MI) and was advanced into the common pulmonary artery. The right femoral artery was cannulated, and a polyvinylchloride catheter (16-gauge, 24-in., Intracath, Becton Dickinson Vascular Access, Sandy, UT) was positioned in the descending aorta. Through a left thoracotomy at the level of the fifth intercostal space, a Silastic catheter (0.062-in. inner diameter, 0.125-in. outer diameter; Dow-Corning, Midland, MI) was positioned in the left atrium. To determine pulmonary transvascular fluid flux (lung lymph flow), a thoracotomy in the fifth and seventh intercostal space was performed, and the efferent vessel of the caudal mediastinal lymph node was cannulated with Silastic medical grade tubing (0.025-in inner diameter, Dow Corning, Midland, MI) with a modified method based on the technique of Staub et al [16]. The animal was given a 5-day recovery period. During this time, they had free access to food and water. Pre and post surgical analgesia was provided with buprenorphine (Buprenorphine SR™, SR Veterinary Technologies, Windsor, CO).

Measured variables

Before beginning studies, catheters were connected to pressure transducers (model PX4X4, Baxter Edwards Critical Care Division, Irvine, CA) with continuous flushing devices. Electronically calculated mean pressures (MAP: mean arterial pressure; CVP: central venous pressure; MPAP: mean pulmonary artery pressure; and LAP: left atrium pressure) were recorded on a monitor with graphic and digital displays (MP30, Philips, Andover, MA). Pressures were measured while sheep were standing and calm. Zero calibrations were taken at the olecranon joint on the frontal leg while the animals were standing. Core body temperature was measured with the thermistor of the Swan-Ganz catheter. 10mL of Saline solution at 1°C served as the thermal indicator. Arterial blood gas samples were analyzed at 37°C and carboxyhemoglobin (COHb) was measured using a conventional blood gas analyzer (RAPIDPoint 500 System, Siemens Healthcare Diagnostics, Tarrytown, NY); consequently corrected for core body temperature. The partial arterial oxygen pressure (PaO_2)/inspired oxygen fraction (FiO_2) ratio, cardiac index (CI), systemic vascular resistance index (SVRI), and oxygenation index (OI) were calculated using standard formulas. Lung lymph flow was measured with graduated test tubes and a stopwatch. Plasma and lymph protein concentrations were measured using a refractometer.

Experimental protocol

After baseline (BL) measurements and sample collections were completed in the healthy state, a tracheostomy was performed under ketamine (KetaVed, Phoenix Scientific, St. Joseph, MO) anesthesia (5mg/kg) and a cuffed tracheostomy tube (10mm diameter, Shiley, Irvine, CA) was inserted into the trachea. In addition, a Foley urinary retention catheter (C.R. Bard, Inc., Covington, GA) was placed in the urinary bladder to monitor fluid balance. Anesthesia was maintained with 2% to 5% Isoflurane (IsoSol, VEDCO, St. Joseph, MO) in O_2 . Smoke inhalation was induced using a modified bee smoker. The bee smoker was filled with 40 g of burning cotton towels and then attached to the tracheostomy tube via a modified endotracheal tube containing an indwelling thermistor from a Swan-Ganz catheter. Four sets of twelve breaths of smoke (total 48 breaths) were delivered, and the carboxyhemoglobin level was determined

immediately after each set. The temperature of the smoke was not allowed to exceed 40°C during the smoking procedure [15, 17, 18]. Immediately after injury, anesthesia was discontinued, and the animals were allowed to awaken but were maintained on mechanical ventilation (Hamilton-G5, Hamilton Medical, Switzerland) throughout the 48-h experimental period.

After the injury, sheep were randomly allocated to one of the two groups ($n = 5$ each): 1) control (injured, treated with vehicle); and 2) ASCs treatment (injured, treated with 200 million of adipose-derived stem cells). The cells were administered intravenously over 30 min via central line, starting 1 h after injury.

All sheep were continuously (around the clock) monitored for 48 hours in the Translational Intensive Care Unit. The variables of hemodynamics, pulmonary function, blood gas exchange, and lung lymph flow (transvascular fluid flux) were recorded every 6 hours.

All sheep were mechanically ventilated in APVcmv mode with positive end-expiratory pressure set at 5 cmH₂O, tidal volume maintained at 12 mL/kg and a respiratory rate of 20 breaths per minute. The breath rate was periodically adjusted to maintain arterial carbon dioxide tension close to baseline values. One hundred percent oxygen was delivered in the first three hours after injury to accelerate the dissociation of carbon monoxide from hemoglobin. The fraction of inspiratory oxygen was periodically adjusted to maintain the arterial oxygen tension above 95 mmHg.

All sheep received fluid resuscitation during the experiment with lactated Ringer's solution following the Parkland formula. During experimental periods, the animals were allowed free access to food, but not to water to accurately measure fluid intake.

ASCs isolation and culture conditions

Subcutaneous adipose tissue was isolated from healthy sheep from the left fifth intercostal incision in preparative surgery and was washed extensively with PBS containing 2% penicillin/streptomycin. The tissue was then minced (2mm or less). Each 10 grams of minced fat tissue was placed in processing 50 ml tube with 2.5 ml of Matrase™ and up to 30 ml of lactated Ringer's solution. Fat tissue was incubated at 37°C for 2 hours using ARC System (InGeneron, Inc). Because ovine adipose tissue has higher levels of saturated fat compared to adipose tissue from humans, longer incubation time was needed for the enzymatic digestion of the fat. Following complete digestion, solution was filtered in Steriflip™ to collect the filtrate. The filtrate was concentrated using ARC System by centrifuge at 600g for 10 minutes. Two washing steps with 60 ml of lactated Ringer's solution were applied in order to have a pellet of stromal vascular fraction. Finally, the pellet was re-suspended in complete media [Dulbecco's Minimum Essential Medium with 10% FBS and 2% antibacterial/antimycotic solution (10,000IU/mL Penicillin; 10,000ug/mL Streptomycin)]. The final pellet was seeded into tissue culture flask of 175 cm², and placed in the 5% CO₂ and 37°C incubator. After incubating for 24 hours, the media was replaced to remove unattached cells and debris. Cells were cultured and frozen down in aliquots. Second passage cells were used for the experiments.

The cells were characterized as below: 1) adherence to plastic in standard culture conditions, 2) expression of specific surface antigen assessed by flow cytometer or PCR (Negative for CD45, CD31, CD14, CD11b and MHC Class II DQ/DR. Positive for CD44, CD73, CD90 and CD105), 3) differentiation potential for osteoblasts, adipocytes and chondroblasts (Fig 1).

Necropsy

Forty-eight hours after injury, animals were deeply anesthetized and euthanized by intravenous administration of xylazine (3.0mg/kg), ketamine (40mg/kg), and buprenorphine (0.01mg/kg) following IACUC approved protocols, and American Veterinary Medical

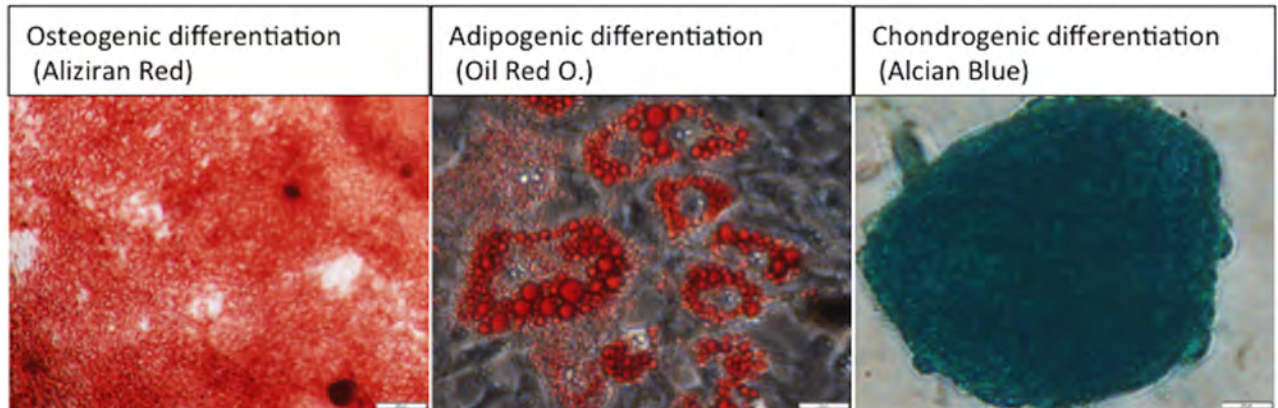


Fig 1. Multipotent differentiation potential of ASCs. The cells were differentiated into osteoblasts (demonstrated by staining with Alizarin Red), adipocytes (demonstrated by staining with Oil O Red) and chondroblasts (demonstrated by staining with Alcian blue).

<https://doi.org/10.1371/journal.pone.0185937.g001>

Association Guidelines for Euthanasia. The lower one-half of the lower lobe of the right lung was used for the determination of bloodless wet-to-dry weight ratio. The organ tissue samples were harvested, snap-frozen in liquid nitrogen and stored at -80°C for later analysis.

Immunohistochemistry

For the distribution study, we prepared 3 sheep in the same manner, and treated with 200 million of GFP-labeled ASCs. Sheep were euthanized 24 hours after the injury. Several organs including the lung, liver, kidney, and spleen were removed, processed and paraffin embedded. 5 μm coronal sections were stained for histopathology analysis of ASCs distribution. In preparation for immunohistochemistry (IHC), samples were deparaffinized and rehydrated in xylene, 100% and 95% alcohol. Antigen retrieval was completed in 95% 0.01M citrate buffer pH 6 followed by a quenching process of 3% endogenous hydrogen peroxide. The sections were blocked with the endogenous avidin- biotin complex (Life Technologies; Waltham, MA) to reduce nonspecific binding. Slides were stained with primary antibody rabbit anti- GFP (1:1000; Abcam Cambridge, MA) and secondary biotinylated anti- rabbit IgG (Vector Laboratories, Burlingame, CA). Horseradish peroxidase streptavidin (Vector Laboratories, Burlingame, CA) was used for color visualization in addition to diaminobenzidine (DAB; Dako, Carpinteria, CA). Sections were counterstained with Harris hematoxylin (Protocol, Thermo-Fischer Scientific, Waltham, MA).

Statistical analysis

All values were expressed as means \pm SEM. Statistic analysis (Prism 6 software [GraphPad Software, Inc. San Diego, CA]) was performed among the groups by two-way ANOVA, followed by post hoc Bonferroni test. COHb levels after smoke inhalation injury and wet-to-dry weight ratio between the groups were compared using non-parametric procedures (Mann-Whitney U test) after confirming non-normal distribution. A value of $P < 0.05$ was regarded as statistically significant.

Results

All animals survived the 48-hour experimental period. The arterial carboxyhemoglobin levels determined immediately after smoke exposure averaged $74.6 \pm 4.3\%$ in the control group and $69.5 \pm 3.3\%$ in the ASCs group. There was no significant difference between these values.

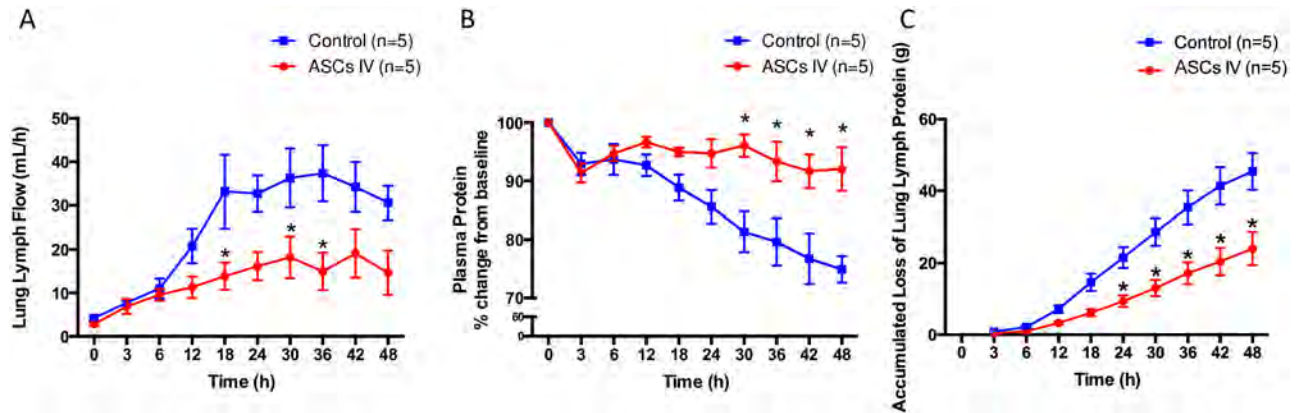


Fig 2. Fluid and protein leakage from lung. Intravenous administration of ASCs significantly reduced the pulmonary microvascular hyperpermeability in sheep caused by cotton smoke inhalation. (A) Lung lymph flow, an index of pulmonary transvascular fluid flux, was increased ~9-fold in control sheep compared to baseline. This was associated with a significant total protein decrease in plasma (B) and its increase in lung lymph(C). Treatment with ASCs prevented these changes.

<https://doi.org/10.1371/journal.pone.0185937.g002>

Lung lymph flow, an index of pulmonary transvascular fluid flux, was increased ~9-fold in control sheep compared to baseline (37.4 ± 14.4 at 36hr, 4.2 ± 1.1 at Baseline). This was associated with a significant total protein decrease in plasma and its increase in lung lymph. The treatment with ASCs significantly attenuated increases in lymph flow (control vs. ASCs; 31.2 ± 6.2 and 13.9 ± 3.1 at 18hr, 33.3 ± 5.6 and 18.2 ± 4.8 at 30hr, 34.1 ± 5.5 and 15.0 ± 4.3 at 36hr, $p < 0.05$) (Fig 2A). The plasma protein significantly decreased immediately after the injury vs. baseline and continued to drop in the control group. Treatment with ASCs prevented these changes (Fig 2B). Accumulated loss of protein with lung lymph tended to increase in both groups, but it was significantly lower after 24hrs in ASC group (Fig 2C). Moreover, the treatment with ASCs almost reversed increased pulmonary vascular permeability index $\{(\text{lung lymph protein} \times \text{lung lymph flow}) / \text{plasma protein}\}$ (Fig 3A) and reduced lung water content (Lung wet-to-dry weight ratio) (5.7 ± 2.6 and 7.9 ± 3.6 , $p = 0.0556$) (Fig 3B).

$\text{PaO}_2/\text{FiO}_2$ ratio decreased below 300 after 24hours in control group. However, pulmonary gas exchange was significantly improved by ASCs treatment. ASCs treatment delayed the

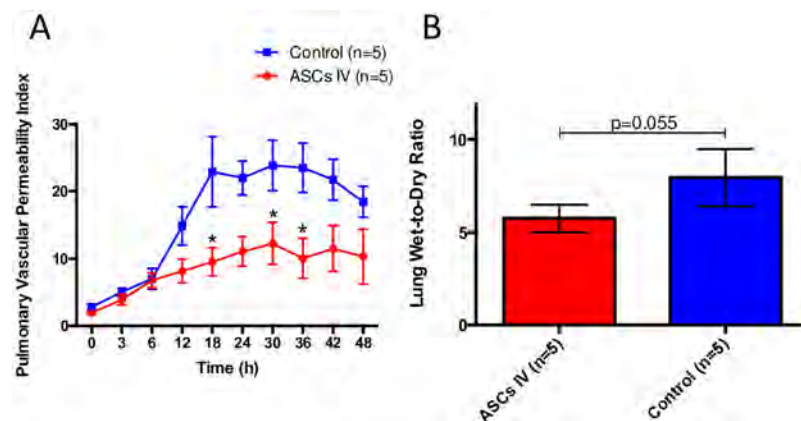


Fig 3. Pulmonary vascular permeability. (A) The treatment with ASCs almost reversed increased pulmonary vascular permeability index and (B) reduced lung water content (Lung Wet-to-Dry Ratio). Smoke inhalation injury causes pulmonary vascular hyperpermeability to both fluid and protein, which was attenuated by ASCs treatment.

<https://doi.org/10.1371/journal.pone.0185937.g003>

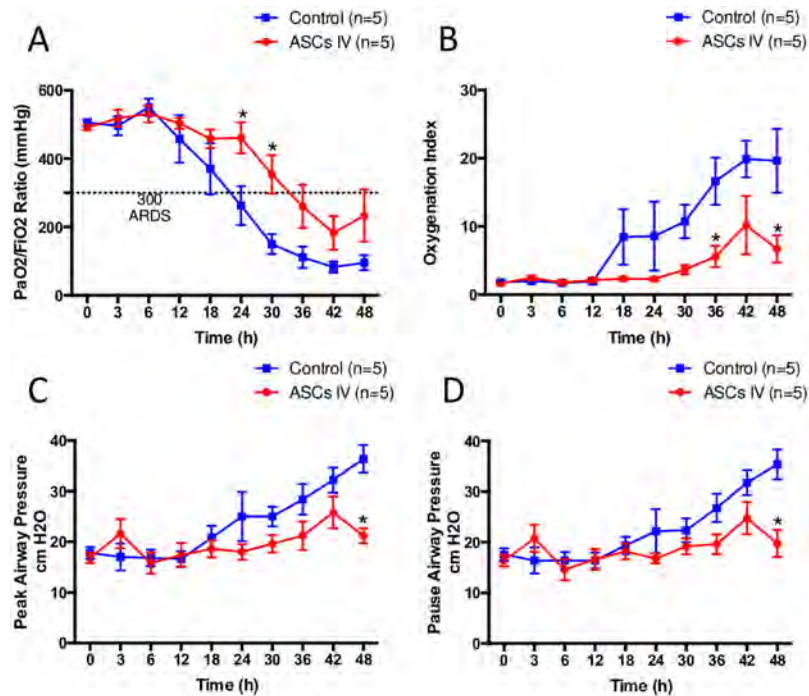


Fig 4. Pulmonary function. The administration of ASCs significantly improved pulmonary gas exchange, evaluated by determining PaO₂/FiO₂ ratio (A), and pulmonary oxygenation index (B). Peak and Pause airway pressures were gradually elevated after 18 hours and reached more than 2 fold in the control group at the end of the study. The treatment also significantly reduced elevated airway pressures (C, D).

<https://doi.org/10.1371/journal.pone.0185937.g004>

onset of ARDS (PaO₂/FiO₂ ratio, control vs. ASCs: 262±127 and 406±101 at 24hr, 150±29 and 354±56 at 30hr, p<0.05) (Fig 4A). Oxygenation index increased markedly in the control group after 18hr and continued to increase over the 48hrs study period. The latter was significantly attenuated by ASCs (P<0.05 at 36hr and 48hr [Fig 4B]).

Peak and Pause airway pressures were increased more than 2 fold in the control group. These changes were significantly inhibited by the ASCs treatment (Fig 4C and 4D).

In treatment group, urine output was significantly higher compared to the control group at 18, 24 and 30hrs after injury (Fig 5A). Increases in accumulated net fluid balance (fluid retention) were significantly attenuated by ASCs treatment compared to control group at 42 and 48hrs after injury (Fig 5B).

Systemic hemodynamics (Table 1)

Mean arterial pressure increased in both groups following injury as compared to baseline values. There was no difference in comparison between the two groups. Systemic vascular resistance also similarly increased post-injury in both groups. Additionally, the pulmonary capillary wedge pressure and central venous pressure did not deviate between the two groups over the experimental period.

The pulmonary artery pressure was not affected during the 30-minute infusion of 200 million ASCs into the jugular vein. In the post-injury time, the changes in pulmonary artery pressure were comparable in both groups except it was significantly higher at 18hrs in ASCs group. Cardiac index displayed no sustained post-injury changes, and there were no differences between sheep receiving therapeutic treatment and control group.

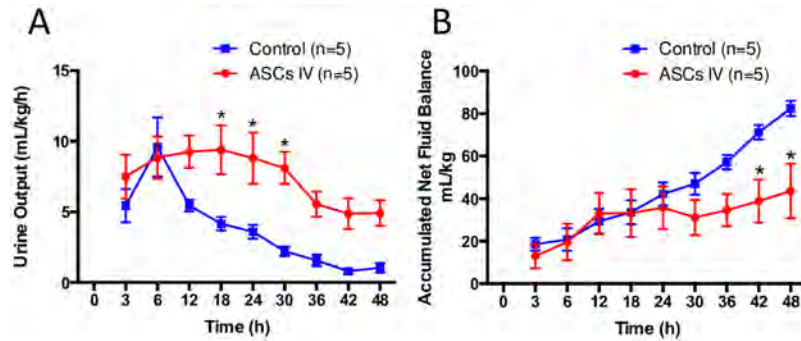


Fig 5. Fluid balance. (A) Urine output was significantly higher in the treatment group. (B) Increases in accumulated net fluid balance (fluid retention) were significantly attenuated by ASCs treatment compared to control group.

<https://doi.org/10.1371/journal.pone.0185937.g005>

Histopathology

Many structurally intact ASCs were detected in the lung interstitial space and seemed to migrate by changing their shape (Fig 6A). Few stained cells were found in liver vasculatures and sinus 24hours after injury (Fig 6B). In spleen, many smaller particles were stained by anti-GFP antibody, and no structurally intact cells were detected (Fig 6C). Urinary tubules were filled by stained particles and some cells were found in glomerulus (Fig 6D), but its integrity was disrupted.

Table 1. Systemic hemodynamics.

	Baseline	Time After Injury, h									
		3	6	12	18	24	30	36	42	48	
MAP, mmHg											
Control	97.8±3.6	108±3.8	105±4.7	99±1.8	94.8±2.4	99.2±2.9	95.6±2.2	94.4±3.9	97.2±1.7	93±4.2	
ASCs	96.6±3.1	114.4±3.4	111.0±3.0	103.8±3.2	101.8±2.6	96.8±4.0	97.6±1.5	99.0±4.0	104.4±2.1	101.8±3.0	
PAP, mmHg											
Control	20.6±0.9	22.0±1.6	24.0±1.4	20.2±0.7	21.4±1.2	29.0±2.5	29.2±2.2	26.4±2.3	26.2±1.8	25.8±1.8	
ASCs	22.2±2.4	27.4±1.7	28.2±1.3	26.4±2.8	30.4±2.7*	27.4±1.5	27.2±1.6	27.8±1.9	28.4±1.4	26.2±2.3	
PCWP, mmHg											
Control	12.4±0.9	13.2±1.7	14.0±1.6	10.6±0.4	11.4±0.5	15.8±0.7	15.6±2.1	14.0±2.1	14.0±1.8	14.2±1.8	
ASCs	13.2±1.9	17.0±1.2	15.2±0.6	14.4±1.2	16.0±1.7	15.2±0.7	15.0±1.2	14.8±2.0	14.6±1.9	15.0±1.8	
CVP, mmHg											
Control	8.2±1.0	7.4±1.2	7.6±1.0	6.6±1.0	6.2±1.0	9.0±1.3	6.0±1.6	7.6±1.9	10.2±1.6	10.8±1.7	
ASCs	7.8±1.4	11.0±1.2	10.4±0.7	7.8±0.9	9.4±0.8	9.8±1.6	9.0±1.7	8.0±2.0	9.0±2.1	9.4±2.2	
CI, L×min ⁻¹ ×m ⁻²											
Control	6.1±0.4	6.2±0.5	5.9±0.2	5.6±0.3	5.4±0.2	5.1±0.6	5.1±0.4	5.2±0.3	5.6±0.5	5.9±0.2	
ASCs	6.4±0.3	6.7±0.4	6.5±0.4	6.3±0.2	6.1±0.2	6.2±0.5	5.3±0.2	6.0±0.4	6.8±0.7	6.0±0.7	
SVRI, dynes×sec×cm ⁻⁵ ×m ⁻²											
Control	1204.2 ±100.7	1322.4 ±94.0	1325.5±66.9	1336.7 ±75.8	1329.1 ±54.3	1457.9 ±132.9	1444.3 ±117.3	1356.1 ±69.6	1275.3 ±116.6	1123.2±60.2	
ASCs	1120.9±44.0	1250.9 ±98.9	1262.7 ±105.5	1226.8 ±19.3	1208.2 ±59.3	1153.3±95.0	1348.2±87.5	1219.0 ±68.7	1177.7 ±142.4	1314.5 ±180.6	

(MAP, mean arterial pressure; CVP, central venous pressure; MPAP, mean pulmonary artery pressure; and LAP, left atrium pressure)

<https://doi.org/10.1371/journal.pone.0185937.t001>

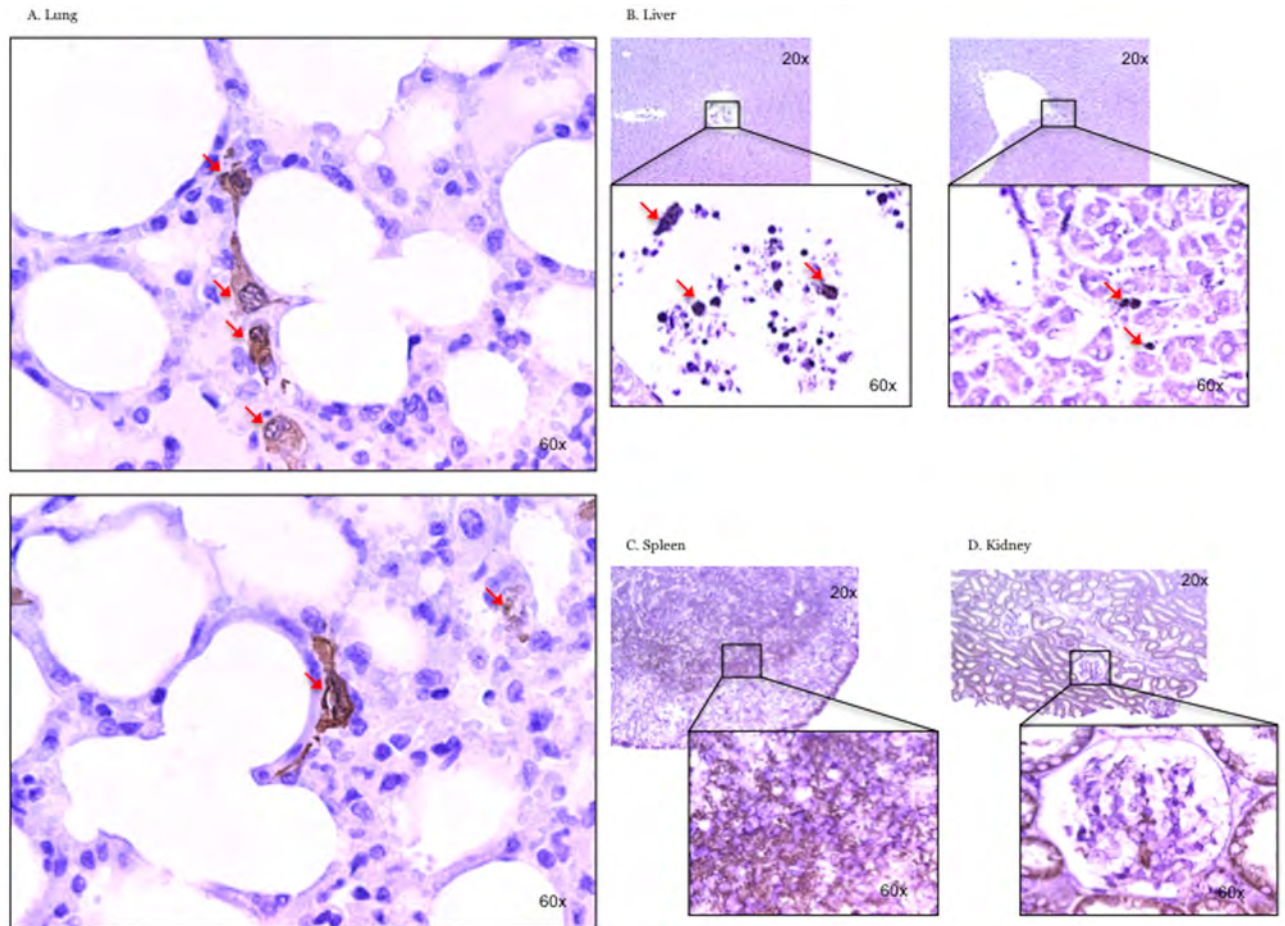


Fig 6. Histopathology. Many structurally intact ASCs were detected in the lung interstitial space (A). Few stained cells were found in liver (B). In the spleen, many smaller particles were stained by anti-GFP antibody (C). Urinary tubules were filled by stained particles (D).

<https://doi.org/10.1371/journal.pone.0185937.g006>

Discussion

The main findings of the present work was as follows:

1) Intravenous administration of ASCs significantly reduced the pulmonary microvascular hyperpermeability in sheep caused by cotton smoke inhalation. This was evidenced by significantly attenuated increases in lung lymph flow, an index of pulmonary microvascular fluid flux, pulmonary microvascular hyperpermeability index and reduced lung water content. These observations were supported by the findings that ASCs significantly reduced the systemic fluid retention, increased the plasma protein, prevented protein loss in lymph, and increased the urinary output. 2) The administration of ASCs significantly improved pulmonary gas exchange, evaluated by determining $\text{PaO}_2/\text{FiO}_2$ ratio (arterial/inspired air oxygen partial pressures), and pulmonary oxygenation index. The treatment also significantly reduced elevated airway pressures. The data from present study suggest that ASCs treatment delayed the onset of mild ARDS and prevented the development of moderate and severe ARDS as the $\text{PaO}_2/\text{FiO}_2$ ratio stayed above 300 up to 30hrs and above 200 in the remaining time period. It is worth noting that the intravenous administration of ASCs was well tolerated, as there were not any negative hemodynamic changes observed, including pulmonary arterial pressure during the 30-minute infusion time.

MSCs are multipotent cells with low immunogenicity that secrete multiple anti-inflammatory cytokines capable of modulating the immune response, attenuating bacterial infection by secretion of antimicrobial peptides, and controlling oxidative stress through the transfer of functional mitochondria to the damaged host cells [11, 19±21]. It has previously been shown that MSCs from different origins ameliorated the severity of acute lung injury [22±25]. In contrast to our research, a majority of these studies were conducted with the rodent model, and treated with bone marrow-derived human mesenchymal stem cells. The sheep model has proven to be an excellent paragon for biomedical research. The anatomy and physiology of the sheep respiratory system is well understood and much more comparable to humans. Hence, the ovine model is appropriate for vaccines, asthma pathogenesis, and inhalation treatment studies.

As mentioned, adipose-derived stem cells exerted a strong effect on systemic and pulmonary microvascular hyper-permeability caused by smoke inhalation; however, the study is limited by insufficiently described mechanistic aspects underlying these salutary effects. It has been shown that beneficial effects of MSCs are mediated by many different factors including their ability to modulate innate and adaptive immune cells, by enhancing anti-inflammatory pathways, such as IL-10 and IL-1 receptor antagonist [26, 27]. Previous studies reported that MSCs alleviate severity of organ injury by their antioxidative effects [28]. MSCs attenuate neutrophil activity and protect against ventilator-induced lung injury [29]. Pati S et al. reported that bone marrow derived mesenchymal stem cells inhibit inflammation and preserve vascular endothelial integrity in the lungs after hemorrhage shock by inhibiting leucocyte adhesion molecules [30]. In our previous studies, we have demonstrated important roles of oxidative stress, neutrophil activation, adhesion molecules, and pro-inflammatory cytokines, such as IL-1 and IL-6 in smoke inhalation-induced acute lung injury in sheep model [31±38]. Thus, based on previous studies by others and our group, we speculate that ASCs may have attenuated severity of smoke inhalation-induced acute lung injury by exerting their potent anti-inflammatory (secretory function) properties.

Previous studies also reported that MSCs attenuate lung injury through lipoxin A4 (LXA4) [39, 40]. It has also been shown that potent permeability factor angiopoietin-2 (ANG2) to play a critical role in the pathophysiology of ARDS [41±43]. We have measured both LXA4 and ANG2 in the lung tissue at 48 hours (time of necropsy); however, these values were not affected by ASCs treatment, suggesting that LXA4 and ANG2 pathways are not involved in the beneficial effect of ASCs on microvascular hyper-permeability and lung tissue injury at least at 48 hours.

Another limitation of our present study is that we were not able to measure inflammatory or permeability markers in the lung tissue at different time points after the injury. It is possible that the peak time of the expression of ANG2 and LXA4 occurred much earlier; as we have reported in our previous studies that inflammatory mediators (lung IL-1 β , TNF- α , IL-6) in mice lung tissue peaked around 9 hours after the injury [36]. We have also reported on the time course of cytokines in sheep sepsis study, in which IL-6 and PARP activation in lung tissue peaked at 8 hours and 12 hours after injury [37].

In the present study, we have determined the distribution of intravenously administered ASCs. We found many structurally intact ASCs in the lung parenchyma 24 hours after the injury (microscopic image). Some intact cells were also spotted in the liver sinus. However, we were not able to find intact ASCs in spleen or urine in spite of the positive signals of green fluorescent protein (GFP) by whole organ imaging or flow cytometer.

Microscopically, we found numerous small particles stained with anti-GFP antibody in spleen and renal tubules. It is worth nothing that whole organ imaging gives some idea of cell

distribution, but this method does not provide information on the cell morphology, while microscopic assay (immunohistochemistry) enables the determination of cell integrity.

Nevertheless, the above results suggest that most of the intravenously administered ASCs are deposited in the lung tissue, migrating to interstitial space. Currently, we have no evidence confirming their differentiation to lung epithelial or endothelial cells; however we do not exclude the possibility of their engraftment, thus repairing the injured cells—this hypothesis should be further investigated. It appears that there was none or minimal (liver) distribution of these cells in non-pulmonary organs at least 24 h injection (another limitation of this study is that we were not able to harvest lung tissue at different times after the ASCs infusion).

Previously, numbers of investigators reported *in vivo* cell distribution. Schrepfer et al. demonstrated that most of intravenously (IV) infused MSCs were trapped in the lung 5 minutes after injection, and lung passing was size dependent [44]. Fischer et al. investigated the pulmonary first-pass effect and found MSCs in carotid artery immediately post-injection, but the numbers were less than 1% of infused cells [45]. Barbash et al. showed that IV injected MSCs were redistributed in liver, kidney and bladder 4 hours after injection using whole body fluorescent imaging [46]. These studies suggest that a small amount of cells pass through the lung microvasculature. However, this notion should be confirmed by future studies with frequent sampling at various time points after the infusion.

Nevertheless, we are reporting for the first time, to our knowledge, the beneficial effects of ASCs in a clinically relevant translation ovine model of acute lung injury induced by smoke inhalation. This is of a particular importance, because there are no clinical studies demonstrating efficacy of MSCs in ARDS patients except two phase-1 safety studies with limited numbers of patients [12, 13]. Previously, our group demonstrated beneficial effects of clinical grade human bone marrow-derived MSCs in ovine model of ALI/ARDS induced by pneumonia sepsis [14].

In conclusion, the results of our previous and present studies as well as prior studies by others, strongly suggest that ASCs could be a safe and efficient therapeutic option for the treatment of ARDS patients. These studies also indicate a need for large, multicenter and prospective clinical studies on the safety and efficacy of ASCs in ARDS patients. Future studies exploring mechanistic aspects specifically focusing on the salutary effects of ASCs on endothelial permeability are warranted.

Supporting information

S1 Data. Data of control sheep; N = 5.
(XLSX)

S2 Data. Data of treatment sheep; N = 5.
(XLSX)

Author Contributions

Conceptualization: Perenlei Enkhbaatar.

Data curation: Koji Ihara, Christina Nelson.

Formal analysis: Koji Ihara.

Investigation: Koji Ihara, Satoshi Fukuda, Baigalmaa Enkhbaatar, Raul Trujillo, Dannelys Perez-Bello, Anita Randolph, Suzan Alharbi, Hira Hanif.

Methodology: Koji Ihara, David Herndon, Donald Prough, Perenlei Enkhbaatar.

Project administration: Koji Ihara, Perenlei Enkhbaatar.

Supervision: David Herndon, Donald Prough, Perenlei Enkhbaatar.

Validation: Koji Ihara.

Visualization: Koji Ihara.

Writing ± original draft: Koji Ihara.

Writing ± review & editing: Perenlei Enkhbaatar.

References

1. Matthay MA, Ware LB, Zimmerman GA. The acute respiratory distress syndrome. *J Clin Invest* 2012; 122: 2731±2740. <https://doi.org/10.1172/JCI60331> Epub 2012 Aug 1. PMID: 22850883
2. Rehberg S, Maybauer MO, Enkhbaatar P, Maybauer DM, Yamamoto Y, Traber DL. Pathophysiology, management and treatment of smoke inhalation injury. *Expert Rev Respir Med* 2009; 3: 283±297 <https://doi.org/10.1586/ERS.09.21> PMID: 20161170
3. Enkhbaatar P, Pruitt BA Jr, Suman O, Mlcak R, Wolf SE, Sakurai H, et al. Pathophysiology, research challenges, and clinical management of smoke inhalation injury. *Lancet* 2016; 388: 1437±1446 [https://doi.org/10.1016/S0140-6736\(16\)31458-1](https://doi.org/10.1016/S0140-6736(16)31458-1) PMID: 27707500
4. Pittenger MF, Martin BJ. Mesenchymal stem cells and their potential as cardiac therapeutics. *Circ Res* 2004; 95: 9±20 <https://doi.org/10.1161/01.RES.0000135902.99383.6f> PMID: 15242981
5. Le Blanc K, Rasmusson I, Sundberg B, Catherstrom C, Hassan M, Uzunel M, et al. Treatment of severe acute graft-versus-host disease with third party haploidentical mesenchymal stem cells. *Lancet* 2004; 363: 1439±1441
6. McDonald JW, Liu XZ, Qu Y, Liu S, Mickey SK, Turetsky D, et al. Transplanted embryonic stem cells survive, differentiate and promote recovery in injured rat spinal cord. *Nat Med* 1999; 5: 1410±1412 PMID: 10581084
7. Dominici M, Blanc KL, Mueller I, Slaper-Cortenbach I, Marini F, Krause D, et al. Minimal criteria for defining multipotent mesenchymal stromal cells. The International Society for Cellular Therapy position statement. *Cytotherapy* 2006; 8: 315±317 <https://doi.org/10.1080/14653240600855905> PMID: 16923606
8. Pittenger MF, Mackay AM, Beck SC, Jaiswal RK, Douglas R, Mosca JD, et al. Multilineage potential of adult human mesenchymal stem cells. *Science* 1999; 284: 143±147 PMID: 10102814
9. Chamberlain G, Fox J, Ashton B, Middleton J. Mesenchymal stem cells: Their phenotype, differentiation capacity, immunological features, and potential for homing. *Stem Cells* 2007; 25: 2739±2749 <https://doi.org/10.1634/stemcells.2007-0197> PMID: 17656645
10. Barry FP, Murphy JM. Mesenchymal stem cells: clinical applications and biological characterization. *Int J Biochem Cell Biol* 2004; 36: 568±584 <https://doi.org/10.1016/j.biocel.2003.11.001> PMID: 15010324
11. Walter J, Ware LB, Matthay MA. Mesenchymal stem cells: mechanisms of potential therapeutic benefit in ARDS and sepsis. *Lancet Respir Med* 2014; 2: 1016±1026. [https://doi.org/10.1016/S2213-2600\(14\)70217-6](https://doi.org/10.1016/S2213-2600(14)70217-6) Epub 2014 Oct 28.
12. Wilson JG, Liu KD, Zhou NJ, Caballero L, McMillan M, Fang X, et al. Mesenchymal stem (stromal) cells for treatment of ARDS: a phase 1 clinical trial. *Lancet Respir Med* 2015; 3: 24±32. [https://doi.org/10.1016/S2213-2600\(14\)70291-7](https://doi.org/10.1016/S2213-2600(14)70291-7) Epub 2014 Dec 17. PMID: 25529339
13. Liu KD, Wilson JG, Zhou HJ, Caballero L, McMillan ML, Fang X, et al. Design and implementation of the START (Stem cells for ARDS Treatment) trial, a phase ½ trial of human mesenchymal stem/stromal cells for the treatment of moderate-severe acute respiratory distress syndrome. *Ann Intensive Care* 2014; 4: 22. <https://doi.org/10.1186/s13613-014-0022-z> eCollection 2014. PMID: 25593740
14. Asmussen S, Ito H, Traber DL, Lee JW, Cox RA, Hawkins HK, et al. Human mesenchymal stem cells reduce the severity of acute lung injury in a sheep model of bacterial pneumonia. *Thorax* 2014; 69: 819±825. <https://doi.org/10.1136/thoraxjnl-2013-204980> Epub 2014 Jun 2. PMID: 24891325
15. Soejima K, Schmalstieg FC, Sakurai H, Traber LD, Traber DL. Pathophysiological analysis of combined burn and smoke inhalation injuries in sheep. *Am J Physiol Lung Cell Mol Physiol* 2001; 280: L1233±1241 PMID: 11350803
16. Staub NC, Bland RD, Brigham KL, Demling R, Erdmann AJ 3rd, Woolverton WC. Preparation of chronic lung lymph fistulas in sheep. *J Surg Res* 1975; 19: 315±320 PMID: 1195727

17. Kimura R, Traber DL, Herndon DN, Linares HA, Lubbesmeyer HJ, Traber DL. Increasing duration of smoke exposure induces more severe lung injury in sheep. *J Appl Physiol* 1988; 64: 1107±1113 PMID: [3366733](https://pubmed.ncbi.nlm.nih.gov/3366733/)
18. Traber DL, Maybauer MO, Maybauer DM, Westphal M, Traber LD. Inhalational and acute lung injury. *Shock* 2005; 24: 82±87 PMID: [16374378](https://pubmed.ncbi.nlm.nih.gov/16374378/)
19. Matthay MA, Thompson BT, Read EJ, McKenna DH Jr, Liu KD, Calfee CS, et al. Therapeutic potential of mesenchymal stem cells for severe acute lung injury. *Chest* 2010; 138: 965±972. <https://doi.org/10.1378/chest.10-0518> PMID: [20923800](https://pubmed.ncbi.nlm.nih.gov/20923800/)
20. Lee JW, Fang XH, Krasnodembskaya A, Howard JP, Matthay MA. Mesenchymal stem cells for acute lung injury: Role of paracrine soluble factors. *Stem Cells* 2011; 29: 913±919. <https://doi.org/10.1002/stem.643> PMID: [21506195](https://pubmed.ncbi.nlm.nih.gov/21506195/)
21. Islam MN, Das SR, Emin MT, Wei M, Sun L, Westphalen K, et al. Mitochondrial transfer from bone-marrow-derived stromal cells to pulmonary alveoli protects against acute lung injury. *Nat Med* 2012; 18: 759±765. PMID: [22504485](https://pubmed.ncbi.nlm.nih.gov/22504485/)
22. Rojas M, Xu JG, Woods CR, Mora AL, Spears W, Roman J, et al. Bone marrow-derived mesenchymal stem cells in repair of the injured lung. *Am J Respir Cell Mol Biol* 2005; 33: 145±152. <https://doi.org/10.1165/rcmb.2004-0330OC> PMID: [15891110](https://pubmed.ncbi.nlm.nih.gov/15891110/)
23. Li J, Li D, Liu X, Tang S, Wei F. Human umbilical cord mesenchymal stem cells reduce systemic inflammation and attenuate LPS-induced acute lung injury in rats. *J Inflamm (Lond)* 2012; 9: 33. <https://doi.org/10.1186/1476-9255-9-33> PMID: [22974286](https://pubmed.ncbi.nlm.nih.gov/22974286/)
24. Zhang S, Danchuk SD, Imhof KM, Semon JA, Scruggs BA, Bonvillain RW, et al. Comparison of the therapeutic effects of human and mouse adipose-derived stem cells in a murine model of lipopolysaccharide-induced acute lung injury. *Stem Cell Res Ther* 2013; 4: 13. <https://doi.org/10.1186/scri161> PMID: [23360775](https://pubmed.ncbi.nlm.nih.gov/23360775/)
25. Hao Q, Zhu YG, Monsel A, Gennai S, Lee T, Xu F, et al. Study of bone marrow and embryonic stem cell-derived human mesenchymal stem cells for treatment of Escherichia coli endotoxin-induced acute lung injury in mice. *Stem Cell Transl Med* 2015; 4: 832±840. <https://doi.org/10.5966/sctm.2015-0006> Epub 2015 May 21 PMID: [25999518](https://pubmed.ncbi.nlm.nih.gov/25999518/)
26. Manning E, Pham S, Li S, Vazquez-Padron RI, Mathew J, Ruiz P, et al. Interleukin-10 delivery via mesenchymal stem cells: a novel gene therapy approach to prevent lung ischemia-reperfusion injury. *Hum Gene Ther* 2010; 21: 713±727 <https://doi.org/10.1089/hum.2009.147> PMID: [20102275](https://pubmed.ncbi.nlm.nih.gov/20102275/)
27. Ortiz LA, Dutreil M, Fattman C, Pandey AC, Torres G, Go K, et al. Interleukin 1 receptor antagonist mediates the antiinflammatory and antifibrotic effect of mesenchymal stem cells during lung injury. *Proc Natl Acad Sci U S A* 2007; 104: 11002±11007 <https://doi.org/10.1073/pnas.0704421104> PMID: [17569781](https://pubmed.ncbi.nlm.nih.gov/17569781/)
28. Mohammadzadeh M, Halabian R, Gharehbaghian A, Amirizader N, Jahanian-Najafabadi A, Roushandedeh AM, et al. Nrf-2 overexpression in mesenchymal stem cells reduces oxidative stress-induced apoptosis and cytotoxicity. *Cell Stress Chaperones* 2012; 17: 553±565
29. Lai TS, Wang ZH, Cai SX. Mesenchymal stem cell attenuates neutrophil-predominant inflammation and acute lung injury in an in vivo rat model of ventilator-induced lung injury. *Chin Med J (Engl)* 2015; 128: 361±367
30. Pati S, Gerber MH, Menge TD, Wataha KA, Zhao Y, et al. Bone marrow derived mesenchymal stem cells inhibit inflammation and preserve vascular endothelial integrity in the lungs after hemorrhagic shock. *PLoS One* 2011; 6: e25171. <https://doi.org/10.1371/journal.pone.0025171> Epub 2011 Sep 28. PMID: [21980392](https://pubmed.ncbi.nlm.nih.gov/21980392/)
31. Enkhbaatar P, Traber DL. Pathophysiology of acute lung injury in combined burn and smoke inhalation injury. *Clin Sci (Lond)* 2004; 107: 137±143
32. Soejima K, Traber LD, Schmalstieg FC, Hawkins H, Jodoin JM, Szabo C, et al. Role of nitric oxide in vascular permeability after combined burns and smoke inhalation injury. *Am J Respir Crit Care Med* 2001; 163: 745±752 <https://doi.org/10.1164/ajrccm.163.3.9912052> PMID: [11254534](https://pubmed.ncbi.nlm.nih.gov/11254534/)
33. Enkhbaatar P, Murakami K, Shimoda K, Mizutani A, Traber L, Phillips GB, et al. The inducible nitric oxide synthase inhibitor BBS-2 prevents acute lung injury in sheep after burn and smoke inhalation injury. *Am J Respr Crit Care Med* 2003; 167: 1021±1026
34. Cox RA, Burke AS, Oliveras G, Enkhbaatar P, Traber LD, Zwischenberger JB, et al. Acute bronchial obstruction in sheep: histopathology and gland cytokine expression. *Exp Lung Res* 2005; 31: 819±837 <https://doi.org/10.1080/01902140600574967> PMID: [16684715](https://pubmed.ncbi.nlm.nih.gov/16684715/)
35. Cox RA, Burke AS, Traber DL, Herndon DN, Hawkins HK. Production of pro-inflammatory polypeptides by airway mucous glands and its potential significance. *Pulm Pharmacol Ther* 2007; 20: 172±177 <https://doi.org/10.1016/j.pupt.2006.03.013> PMID: [16814583](https://pubmed.ncbi.nlm.nih.gov/16814583/)

36. Lange M, Nakano Y, Traber DL, Hamahata A, Traber LD, Enkhbaatar P. Time course of the inflammatory and oxidative stress response to pulmonary infection in mice. *Exp Lung Res* 2012; 38: 157±163. <https://doi.org/10.3109/01902148.2012.663453> PMID: 22394289
37. Lange M, Szabo C, Traber DL, Horvath E, Hamahata A, Nakano Y, et al. Time profile of oxidative stress and neutrophil activation in ovine acute lung injury and sepsis. *Shock* 2012; 37: 468±472. <https://doi.org/10.1097/SHK.0b013e31824b1793> PMID: 22266977
38. Rehberg S, Yamamoto Y, Sousse LE, Jonkam C, Zhu Y, Traber LD, et al. Antithrombin attenuates vascular leakage via inhibiting neutrophil activation in acute lung injury. *Crit Care Med* 2013; 41: e439±446. <https://doi.org/10.1097/CCM.0b013e318298ad3a> PMID: 24107637
39. Wang Q, Lian QQ, Li R, Ying BY, He Q, Chen F, et al. Lipoxin A(4) activates alveolar epithelial sodium channel, Na, K-ATPase, and increases alveolar fluid clearance. *Am J Resp Cell Mol Biol* 2013; 48: 610±618. <https://doi.org/10.1165/rcmb.2012-0274OC> PMID: 23470626
40. Fang XH, Abbott J, Cheng LD, Colby JK, Lee JW, Levy BD, et al. Human mesenchymal stem (stromal) cells promote the resolution of acute lung injury in part through lipoxin A4. *J Immunol* 2015; 195: 875±881. <https://doi.org/10.4049/jimmunol.1500244> Epub 2015 Jun 26. PMID: 26116507
41. Orfanos SE, Kotanidou A, Glynos C, Athanasiou C, Tsigkos S, Dimopoulou I, et al. Angiopietin-2 is increased in severe sepsis: correlation with inflammatory mediators. *Crit Care Med* 2007; 35: 199±206 <https://doi.org/10.1097/01.CCM.0000251640.77679.D7> PMID: 17110873
42. Van der Heijden M, van Nieuw Amerongen GP, Koolwijk P, van Hinsbergh VW, Groeneveld AB. Angiopietin-2, permeability oedema, occurrence and severity of ALI/ARDS in septic and non-septic critically ill patients. *Thorax* 2008; 63: 903±909. <https://doi.org/10.1136/thx.2007.087387> Epub 2008 Jun 17. PMID: 18559364
43. Parikh SM, Mammoto T, Schulz A, Yuan HT, Christiani D, Karumanchi SA, et al. Excess circulating angiopoietin-2 may contribute to pulmonary vascular leak in sepsis in humans. *PLoS Med* 2006; 3: e46 <https://doi.org/10.1371/journal.pmed.0030046> PMID: 16417407
44. Schrepfer S, Deuse T, Reichenspumer H, Fischbein MP, Robbins RC, Pelletier MP. Stem cell transplantation: The lung barrier. *Transplant Proc* 2007; 39: 573±576 <https://doi.org/10.1016/j.transproceed.2006.12.019> PMID: 17362785
45. Fischer UM, Harting MT, Jimenez F, Monzon-Posadas WO, Xue H, Savitz SI, et al. Pulmonary passage is a major obstacle for intravenous stem cell delivery: the pulmonary first-pass effect. *Stem Cell Dev* 2009; 18: 683±692. <https://doi.org/10.1089/scd.2008.0253> PMID: 19099374
46. Barbash IM, Chouraqui P, Baron J, Feinberg MS, Etzion S, Tessone A, et al. Systemic delivery of bone marrow±derived mesenchymal stem cells to the infarcted myocardium feasibility, cell migration, and body distribution. *Circulation* 2003; 108: 863±868 <https://doi.org/10.1161/01.CIR.0000084828.50310.6A> PMID: 12900340

Stem Cell Therapy for Craniofacial Bone Regeneration: A Randomized, Controlled Feasibility Trial

Darnell Kaigler,*†‡§ Giorgio Pagni,* Chan Ho Park,* Thomas M. Braun,§ Lindsay A. Holman,*
Erica Yi,* Susan A. Tarle,* Ronnda L. Bartel,¶ and William V. Giannobile*†‡

*Department of Periodontics and Oral Medicine, University of Michigan, Ann Arbor, MI, USA

†University of Michigan Center for Oral Health Research, Ann Arbor, MI, USA

‡Department of Biomedical Engineering, University of Michigan, Ann Arbor, MI, USA

§Department of Biostatistics, University of Michigan, Ann Arbor, MI, USA

¶Aastrom Biosciences, Inc., Ann Arbor, MI, USA

Stem cell therapy offers potential in the regeneration of craniofacial bone defects; however, it has not been studied clinically. Tissue repair cells (TRCs) isolated from bone marrow represent a mixed stem and progenitor population enriched in CD90- and CD14-positive cells. In this phase I/II, randomized, controlled feasibility trial, we investigated TRC cell therapy to reconstruct localized craniofacial bone defects. Twenty-four patients requiring localized reconstruction of jawbone defects participated in this longitudinal trial. For regenerative therapy, patients were randomized to receive either guided bone regeneration (GBR) or TRC transplantation. At 6 or 12 weeks following treatment, clinical and radiographic assessments of bone repair were performed. Bone biopsies were harvested and underwent quantitative micro-computed tomographic (μ CT) and bone histomorphometric analyses. Oral implants were installed, subsequently restored, and functionally loaded with tooth restorations. Reconstructed sites were assessed for 1 year following therapy. No study-related, serious adverse events were reported. Following therapy, clinical, radiographic, tomographic, and histological measures demonstrated that TRC therapy accelerated alveolar bone regeneration compared to GBR therapy. Additionally, TRC treatment significantly reduced the need for secondary bone grafting at the time of oral implant placement with a five-fold decrease in implant bony dehiscence exposure (residual bone defects) as compared to GBR-treated sites ($p < 0.01$). Transplantation of TRCs for treatment of alveolar bone defects appears safe and accelerates bone regeneration, enabling jawbone reconstruction with oral implants. The results from this trial support expanded studies of TRC therapy in the treatment of craniofacial deformities (ClinicalTrials.gov number CT00755911).

Key words: Bone regeneration; Craniofacial tissue engineering; Stem cells; Cell therapy; Implants

INTRODUCTION

Treatment of oral and craniofacial diseases represent a substantial component of the global healthcare burden, with dental caries (tooth decay) and periodontal disease (gum disease) representing two of the most prevalent infections worldwide, oral cancer being the sixth most common cancer, and cleft lip and cleft palate representing two of the most common congenital defects (24,27). Though current treatment modalities provide functional and structural restorations of affected tissues, most approaches do not meet emerging concepts toward more biological treatment outcomes. New cell- and tissue-based strategies need development to overcome limitations of traditional treatments using allogeneic and synthetic substitutes for craniofacial reconstruction (29).

Bone marrow-derived mesenchymal stem cells are a commonly used cell type for utilization in cell-based regenerative approaches in craniofacial applications (8,9,15,17). Preclinical studies have demonstrated success in their use for bone regeneration (9,11,14,15), and more recently, several clinical reports have investigated the potential of autologous grafts containing bone marrow-derived cells in the repair of craniofacial defects (6,18–20,28). Though these preliminary reports hold promise, two limitations common to them are (1) the techniques used for cell isolation are crude and (2) the grafts used for transplantation are not well characterized.

To begin addressing these limitations, we report the first randomized, controlled clinical trial utilizing bone marrow-derived stem cells for the regeneration of

Received October 25, 2011; final acceptance April 25, 2012. Online prepub date: July 5, 2012.

Address correspondence to Darnell Kaigler, D.D.S., M.S., Ph.D., Department of Periodontics and Oral Medicine, University of Michigan, 1011 N. University, Ann Arbor, MI 48109, USA. Tel: +1-734-615-4023; E-mail: dkaigler@umich.edu or William V. Giannobile, D.M.D., D.Med.Sc., Michigan Center for Oral Health Research, University of Michigan, 1011 N. University Ave., Ann Arbor, MI 48109, USA. Tel: +1-734-763-2105; E-mail: william.giannobile@umich.edu

craniofacial bone. This study compares a novel cell therapy for the treatment of localized jaw bone defects to a conventional guided bone regeneration procedure (GBR) (22). The cells employed in this study, tissue repair cells (TRCs or ixmyelocel-T, Aastrom Biosciences, Ann Arbor, MI, USA), are composed of a mixture of bone marrow-derived cells including expanded CD90⁺ mesenchymal stem cells, CD14⁺ monocytes/macrophages, as well as mononuclear cells from the original bone marrow aspirate (2,30). The central hypothesis underlying this feasibility trial was that a cell therapy approach using TRCs would be safe and efficacious in the regeneration of localized craniofacial bone defects.

MATERIALS AND METHODS

All chemicals are from Sigma-Aldrich (St. Louis, MO, USA) unless stated otherwise.

Patients

Following U.S. Food and Drug Administration and University of Michigan Institutional Review Board (IRB) approval, 24 patients requiring a tooth extraction were recruited to participate in this phase I/II trial (ClinicalTrials.gov number CT00755911). No power analysis was performed to determine the sample size, but instead, the number of participants for this trial was chosen for feasibility rather than statistical precision as a first-in-humans investigation. Healthy male and female participants, ages 20–70, were included if they were able and willing to read, understand, and sign an informed consent. Patients were excluded from participation if they had or exhibited one of the following conditions: blood dyscrasia, active infectious disease, liver or kidney dysfunction, endocrine disorders, cancer, current or history of bisphosphonate use, metabolic bone disorder, HIV⁺, pregnant, current smoker, <2 mm of bone from apex of the tooth to be extracted to the floor of the maxillary sinus, <4 mm of bone from apex of the tooth to be extracted to the crest of the alveolar bone.

Study Design

From March 2008 to October 2009, 24 osseous defects of 24 patients were treated and evaluated for bone regeneration. Half (12) of the subjects were assigned to receive the TRC therapy, and the other half received the control GBR therapy. Further, the participants were allocated within each treatment arm for either a 6- or 12-week bone core harvest and comprehensive safety and efficacy measures. Thus, six patients each were assigned to one of four possible patient groups (treatment arm crossed with time of outcome). Patients were randomized in blocks of four with a computer-generated randomization schedule, with one patient in each block assigned to one of the four patient groups. Due to the nature of the TRC group requiring autologous

bone marrow aspiration, patient and surgeon masking was not possible. However, allocation of treatment was masked from examiners of primary outcome measures (radiographic, micro-computed tomography, histological and biochemical assessments). Additionally, patients assigned to the 12-week time point were not allowed to “cross over” to the 6-week time point.

Clinical Procedures

The bioreactor production of TRCs has been previously described (7). Briefly, following University of Michigan Institutional Review Board (IRB) approval, 12 healthy human participants giving informed consent underwent a bone marrow aspiration of the posterior ilium under conscious sedation and local anesthetic (ClinicalTrials.gov number CT00755911). Collected marrow was transferred to a sterile blood bag and then inoculated into a bioreactor, which is a proprietary computer-controlled, automated cell processing unit (Aastrom Biosciences). The cell cassette within this system provides a functionally closed, sterile environment in which cell production occurs. The fluid pathway in the cell cassette includes the cell growth chamber, a medium supply container, a mechanism for medium delivery, a waste medium collection container, and a container for the collection of harvested cells. The culture medium consists of Iscove’s modified Dulbecco’s medium (IMDM), 10% fetal bovine serum, 10% horse serum, 5 μ M hydrocortisone. This system incorporates single-pass perfusion in which fresh medium flows slowly over cells without retention of waste metabolites or differentiating cytokines. After cultivation for 12 days at 37°C and 5% CO₂, the TRC product was harvested by trypsinization, resuspended, and collected into a sterile bag where it was stored until the time of transplantation. According to previously described methods for characterization of TRCs (7,10), flow cytometry was performed immediately following enrichment of TRCs with fluorochromes conjugated to antibodies to CD90, CD34, CD19, vascular endothelial growth factor receptor 1 (VEGFR1), Tie2 (tyrosine kinase with immunoglobulin-like and epidermal growth factor-like domains 2), CD145, CD45, CD3, CD144, CD184, (Beckman Coulter, Indianapolis, IN, USA). The flow cytometry data confirmed the characterization of these cells as previously reported (7,10); hence, the data are not shown here.

For the 24 patients selected to participate in this study, tooth extraction of a nonrestorable tooth was performed and its removal resulted in an area of a localized osseous defect. In the TRC group ($n=12$), 1 ml of the TRC suspension (approximately 1.5×10^7 cells/ml) was placed onto an absorbable gelatin sponge (Gelfoam®, Pfizer, New York, NY, USA) sized to a dimension of ~ 2 cm³. The sponge was then delivered into the extraction socket. In the GBR group ($n=12$), only the sponge, soaked in 1 ml sterile saline, was transplanted into the socket. In

both treatment groups, a bioabsorbable collagen barrier membrane (Biomend[®], Zimmer Dental, Carlsbad, CA, USA) was placed over the sponge to contain the cell construct and the tissues were closed. Surgical reentry of the treated osseous defect was performed 6 or 12 weeks post-surgery, and a bone core of 2×7 mm was harvested with a trephine drill (Ace Surgical Supply Co., Brockton, MA, USA). The core was prepared for micro-computed tomography (μ CT) and histomorphometry through which bone mineral density (BMD), bone volume fraction (BVF), and bone area/tissue area (BA/TA) were all measured.

Outcome Assessments

Radiographic bone height was assessed at the time of bone biopsies. Standardized digital radiographs were assessed using Emago[®] software (Exan Academic, Inc., Port Coquitlam, BC, Canada). In comparison to baseline images, the follow-up images (6 and 12 weeks) were corrected for changes in gamma exposure and angulation differences. Linear measurements were taken from the base of the extraction socket to the alveolar crest along the long axis of the socket in the baseline, 6-week, and 12-week images from both GBR and TRC treatment groups. “Linear radiographic bone height” measures were calculated as a percentage of the regenerated bone height over the height of the initial defect.

If sufficient bone volume and density (23) was present at the time of surgical reentry of treated sites, oral implants (Screwplant[®], Implant Direct, Inc., Agoura Hills, CA, USA) of appropriate sizes were placed. If residual bone deficiencies remained at the time of implant placement causing implant exposure, an additional bone grafting procedure was performed. The degree to which implants were exposed was measured as the percent linear implant exposure (length of exposed area of implant divided by the total implant length) and the amount of secondary graft material was recorded at the time of surgery. This secondary grafting was performed with either an allogeneic bone graft material (Oragraft[®], Salvin Dental Specialties, Inc., Charlotte, NC, USA) alone or in combination with a barrier membrane.

The ability of the oral implant fixtures to sustain biomechanical forces under functional loading with single tooth implant restorations (crowns) was assessed at 3 and 6 months postloading, with qualitative radiographic evaluation of changes in crestal bone height at these time points.

Micro-computed tomographic (μ CT) analyses of bone core biopsies were performed as previously described (25). Briefly, the nondecalcified core was captured with the scanning direction parallel to the longitudinal axis of the core specimen. High-resolution scanning with an in-plane pixel size and slice thickness of 24 μ m was performed. To cover the entire thickness of the bone core biopsy, the number of slices was set at 400. MicroView[®] software (GE Medical Systems, London, ON, Canada) was used to make three-

dimensional (3D) reconstructions from the set of scans. To obtain 3D images, a threshold value of 1,100 was used. On 3D images of the specimen, the total volume (TV, mm³), bone volume (BV, mm³), and bone mineral density (BMD) of the bone core was measured directly, and the fractional bone volume (3D BV/TV, %) was calculated. After scanning, the core was decalcified and, following decalcification, was prepared histologically for standard hematoxylin and eosin (H&E) staining to perform bone histomorphometry, as previously described (14).

Alkaline Phosphatase (AP) Activity

To quantify the AP activity of TRCs, following 1 week of culture in “osteogenic” media [minimum essential medium (MEM) with 15% fetal bovine serum, 5 μ g/ml gentamycin, 5 mM β -glycerol phosphate, 100 nM dexamethasone, and 50 μ M ascorbic acid 2-phosphate], cells were lysed in passive lysis buffer (Promega Corporation) according to the manufacturer’s instructions and cell lysates were sonicated and centrifuged. The supernatant was recovered for the quantitative colorimetric AP assay as previously described (19). The cell pellet was used for DNA isolation and the determination of the DNA concentration using the Quant-iT[™] dsDNA BR Assay (Invitrogen, Life Technologies Corporation, Grand Island, NY, USA) as per the manufacturer’s instructions.

Mineralization Assay (Von Kossa)

To detect TRC mineralized matrix formation indicative of osteogenic differentiation, all 12 TRC populations were plated at a density of 30,000 cells per well in 12-well plates. At 100% confluence (which was reached following 3–5 days of culture in plates), cells were induced with “osteogenic media” (described above) for 21 days. TRCs were fixed in 4% paraformaldehyde for 30 min, immersed in fresh 5% silver nitrate and incubated in the dark for 30 min. After washing in water, TRCs were exposed to ultraviolet light for 30 min followed by a 4-min incubation in 1% sodium thiosulfate. Photographs were taken of the stained plates. These photographs were analyzed using the Mac software ImageJ (from the NIH, Bethesda, MD, USA), and the mineral density measurements were performed on the photographs. Mineral density calculations were performed by taking a measurement from the control Von Kossa plate (uninduced cells) and a measurement from the osteogenically induced plate. The density measurement from the control plate (indicative of background staining) was subtracted from the measurement of the induced plate, and this difference was reported as a relative value (“Von Kossa relative staining intensity”; % of control).

Statistical Analysis

A data safety monitoring board (DSMB) provided oversight throughout the course of the investigation and

findings from this committee were submitted along with the yearly reports to the U.S. FDA. The outcomes of the investigation followed the study protocol for the primary outcome variables as well as for several post hoc analyses, including correlation of BMD/BVF with osteogenic differentiation/mineralization, percentage of implant exposure, and need for additional bone grafting. Safety analyses were accumulated at each postbaseline visit and included reporting of adverse events by body system, severity, and relationship to TRC therapy, as assessed by the investigator. Statistical analysis was performed with the statistical software package R (R Foundation for Statistical Computing, Vienna, Austria). Data are reported as means \pm standard deviation, and 95% confidence intervals (CI) for the mean differences between groups (GBR and TRC) are reported in the tables; differences in means between the treatment groups were assessed with a two-sample *t* test. Correlation was based upon Pearson's product-moment correlation coefficient (*r*), with significance based on Fisher's *Z* transformation. Statistical significance was defined as *p* < 0.05.

RESULTS

Study Design and Patients

Throughout the study, there were no serious, study-related adverse events that were reported in examination of comprehensive safety assessments during the trial. It should be noted that one patient was lost to follow-up

and did not return for the final two study visits (following restoration). The baseline demographic characteristics of all study participants are shown in Table 1. Figure 1A shows the trial timeline, and Figure 1B displays the consort diagram of the patient allocation to groups. It should be noted that, in order to obtain a total of 12 patients in the TRC groups (six for 6 weeks and six for 12 weeks), it required a total of 16 participants to be randomized to this group because aspirates could not be obtained from four patients due to high body mass index (BMI) values (>25). This necessitated the requirement for an amended protocol which, from this point, excluded study participation of patients who presented at bone marrow aspiration with a BMI > 25.

Clinical Outcomes: Bone Density and Residual Bone Defects

Figure 2A shows images of GBR and TRC treatment defects at the time of tooth extraction (baseline) and 6 weeks after therapy. At 6 weeks, there was greater radiographic bone height achieved in the TRC group than in the GBR group, as measured by the percentage of the radiographic bone fill within the extraction defect (Fig. 2B) (*p* = 0.01). At 12 weeks, the GBR group displayed 74.6 \pm 3.3% bone fill while the TRC groups showed 80.1 \pm 2.0% bone fill, *p* = 0.28 (Table 2).

Figure 2C shows photographic images of TRC and GBR treatment sites at baseline, 6 weeks after treatment, and fully restored 1 year after initial surgery. Clinically, in

Table 1. Patient Demographics

	6-Week Time Point		12-Week Time Point	
	GBR	TRC	GBR	TRC
% Female	66.7	50	50	50
Ethnicity	6 Caucasians	1 Asian, 5 Caucasians	1 African American, 4 Caucasians, 1 Hispanic	1 African American, 5 Caucasians
Mean age (range, years)	53 (38–62)	48 (31–57)	53 (46–63)	44 (38–56)
Maxillary/mandibular teeth	4/2	4/2	5/1	5/1
Reason for extraction	Fractured tooth = 5 Periodontal disease = 1 Tooth decay = 0	Fractured tooth = 4 Periodontal disease = 1 Tooth decay = 1	Fractured tooth = 4 Periodontal disease = 0 Tooth decay = 2	Fractured tooth = 4 Periodontal disease = 1 Tooth decay = 1
Number of patients with bone defect present at time of extraction	3	4	4	4
Mean implant diameter (range, mm)	4.5 (3.7–4.7)	4.2 (3.7–4.7)	4.2 (3.7–4.7)	4.4 (3.7–4.7)
Mean implant length (range, mm)	12.0 (10–13)	12.3 (10–13)	11.5 (10–13)	12.3 (10–13)
Mean (keratinized) gingival thickness, mm (SD)	1.8 (1.2)	1.5 (0.5)	1.8 (0.7)	1.1 (0.2)
Mean (keratinized) gingival tissue width, mm (SD)	4.8 (2.9)	3.8 (0.7)	5.2 (1.2)	4.7 (1.8)

GBR, guided bone regeneration; TRC, tissue repair cell.

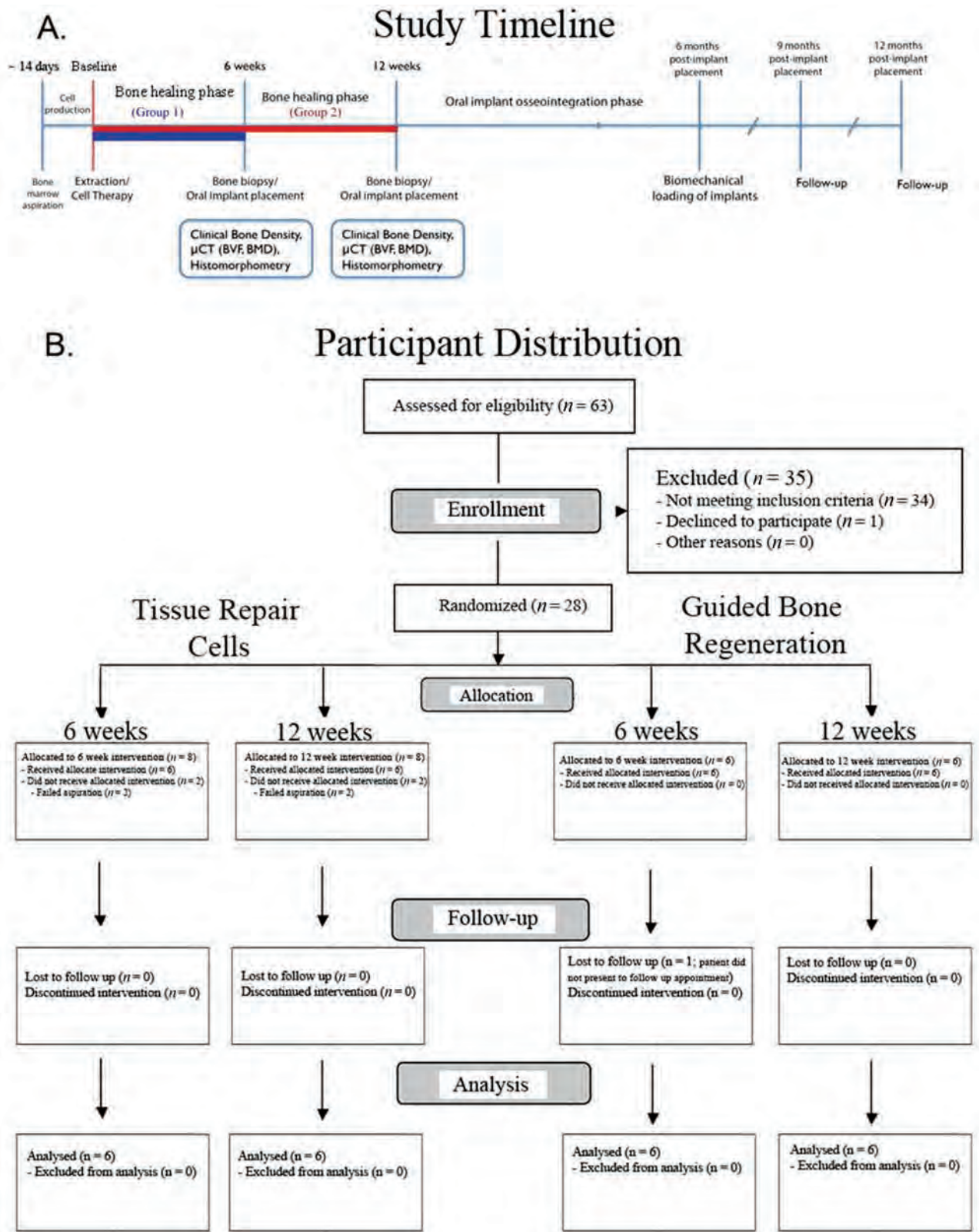


Figure 1. Trial profile and consort diagram. (A) Trial timeline. (B) Consort diagram of patient distribution. μ CT, micro-computed tomography; BVF, bone volume fraction; BMD, bone mineral density.

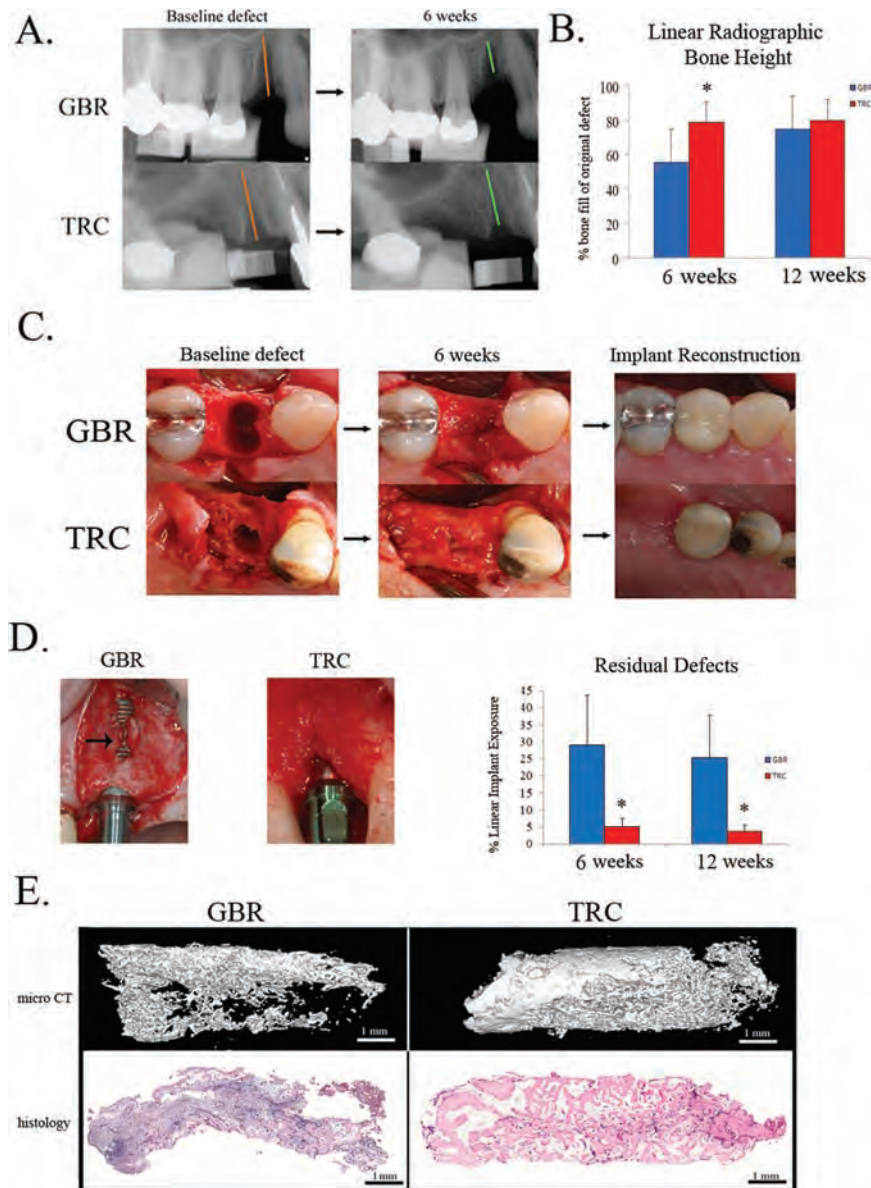


Figure 2. Tissue repair cells (TRCs) promote regeneration of alveolar bone defects. (A) Digital radiographic images of linear bone height density measures for guided bone regeneration (GBR) and TRC groups at the time of tooth extraction (baseline) and 6 weeks after treatment. (B) Standardized digital radiography (SDR) was used to assess linear changes in radiographic bone height from baseline to 6- and 12-week time points. In the baseline images (A), the (orange) lines show the full extent (height) of the original defect, created following extraction of the tooth. In the 6-week images, the (green) lines show the extent (height) to which there was radiographic bone fill. These heights were calculated and the linear length of the bone fill was determined by calculating the percentage of the original defect which was filled with radiographic evidence of bone. (C) Clinical photographs of the defect site created immediately following removal of the tooth, at reentry into the site 6 weeks following treatment, and 12 months following treatment after full restoration of the site with an oral implant supported crown. (D) In some patients, residual bony defects were noted at the time of reentry into the defect sites, and in other patients, remaining bone deficiencies were identified during implant placement. There was significantly greater implant exposure in those patients receiving GBR versus those patients receiving TRCs ($p < 0.04$). (E) Micro-computed tomographic and histomorphometric analyses. Micro-CT and histological evaluation (H&E staining) of bone formation in a representative specimen from a GBR-treated site and a TRC treated site 6 weeks following treatment (original magnification: $2\times$). Both sections show varying degrees of mature cortical bone with high vascularity, as indicated by the abundance of blood vessels. Bone volume fraction (BVF), bone mineral density (BMD), and histomorphometric measures were quantified and compared between TRC and GBR treated sites at 6 and 12 weeks.

Table 2. Summary of Primary Outcome Measures

	6-Week Time Point		12-Week Time Point	
	GBR	TRC	GBR	TRC
Linear bone height (%)				
Mean	55.3	78.9	74.6	80.1
Mean diff GBR & TRC	23.6		5.4	
95% CI	6.02, 41.09		-12.11, 22.95	
<i>p</i> value	0.01		0.28	
Bone volume fraction (BVF)				
Mean	0.13	0.28	0.24	0.30
Mean diff GBR & TRC	0.15		0.05	
95% CI	-0.03, 0.34		-0.14, 0.24	
<i>p</i> value	0.07		0.30	
Bone mineral density (BMD, mg/cc)				
Mean (mg/cc)	85.5	195.0	146.6	186.8
Mean diff GBR & TRC	109.5		40.2	
95% CI	-28.6, 247.5		-97.8, 178.3	
<i>p</i> value	0.08		0.29	
Bone area/tissue area (BA/TA)				
Mean	0.196	0.335	0.351	0.352
Mean diff GBR & TRC	0.139		0.002	
95% CI	-0.053, 0.332		-0.191, 0.194	
<i>p</i> value	0.09		0.49	

the GBR-treated sites, the regenerated tissues at 6 weeks appeared highly vascular and fibrous, and most specimens were notably soft during biopsy harvest. Overall, the regenerated tissues in the TRC sites exhibited a bone-like appearance clinically, were more dense, and demonstrated high vascularity during biopsy harvest.

At the time of reentry into the grafted sites, clinical assessments were performed to determine if there would be a need for additional bone grafting to stably place an oral implant. The decision was made to perform additional grafting if one of two possible scenarios occurred: (1) if residual bone defects persisted following initial treatment or (2) if bone deficiencies (i.e., dehiscences or fenestrations) were identified during oral implant placement (Fig. 2D). In all four groups, oral implants were able to be stably placed at their respective scheduled time points. However, due to a greater number of residual bone defects present in the groups initially treated with GBR, there was a greater need for the GBR groups (6 and 12 weeks) to receive secondary bone grafting procedures at the time of implant placement, relative to the need within the TRC-treated groups (Table 3). Additionally, in the GBR groups at both 6 and 12 weeks, there was about sixfold greater percent implant exposure which necessitated more extensive secondary grafting, relative to this need in the TRC treated groups ($p < 0.04$) (Fig. 2D and Table 3). Although different implant lengths and diameters were used at the time of implant installation, in general the sizes used were quite similar

(Table 1). For each of the treatment groups following the regenerative procedures, all implants achieved clinical evidence of integration into the restored bone and were able to sustain biomechanical loading when restored with an implant restoration 6 months following placement. Implant stability was followed for 1 year, and all implants remained functionally integrated at study completion.

Biopsy Analyses: μ CT and Histomorphometry

Bone core biopsies from the regenerative sites were analyzed 6 and 12 weeks following treatment using three-dimensional μ CT and histomorphometry (Fig. 2E and Table 2). Bone volume fraction (BVF) and bone mineral density (BMD) were the primary μ CT outcome measures, and analysis at 6 weeks showed that the BVF for the GBR group was $13 \pm 6\%$, compared to $28 \pm 8\%$ for the TRC-treated group ($p = 0.08$). Similarly, in comparisons of BMD measures between GBR- and TRC-treated groups, bone repair in the TRC group had a greater than twofold higher BMD (195.0 ± 63.3 mg/cc) than regenerated bone in the GBR group (85 ± 46.3 mg/cc; $p = 0.1$).

Following micro-CT analysis, bone core biopsies of regenerated bone were further evaluated histomorphometrically. When visualized under light microscopy, the majority of the samples were comprised of a highly cellular, dense connective tissue exhibiting the presence of an abundance of blood vessels, yet there were

Table 3. Residual Bone Defects Following Surgery

	6-Week Time Point		12-Week Time Point	
	GBR	TRC	GBR	TRC
Mean % linear implant exposure	29.2	5.1	25.3	3.8
95% CI	(-1.2, 60)	(-8.5, 18.7)	(-0.9, 51.5)	(-6.1, 14)
<i>p</i> value	0.04	0.04	0.03	0.03
Cases Requiring secondary bone grafting	5	2	3	2
Mean amount additional graft used (cc)	0.23	0.09	0.08	0.05
95% CI	(0.02, 0.44)	(-0.01, 0.2)	(-0.02, 0.2)	(-0.05, 0.16)
<i>p</i> value	0.08	0.08	0.31	0.31

differences at 6 weeks between the specimens harvested from TRC- and GBR-treated sites with the presence of more bone in the TRC sites (Fig. 2E). Upon 6- and 12-week analyses, no statistically significant differences were found in measures of % bone area/tissue area (BA/TA). At 6 weeks, regenerated tissue from the GBR group had a BA/TA of $19.6 \pm 4.2\%$, while tissue from the TRC-treated group had a BA/TA of $28.8 \pm 9.1\%$ ($p=0.10$ between groups) (Table 2). At the 12-week time point, the percentage of regenerated bone tissue appeared to be

similar between the GBR- and TRC-treated groups, with BA/TA measures for these groups being $35.1 \pm 3.2\%$ and $35.2 \pm 8.9\%$, respectively (Table 2).

As an ad hoc analysis, in vitro osteogenic potential (AP activity) and mineralization (Von Kossa) ability of TRCs were correlated with the clinical outcome measures of BMD and BVF for each respective TRC population. These data demonstrated that there was a positive correlation between AP and BVF ($r=0.56$, $p=0.058$) and a statistically significant positive correlation between AP and

Osteogenic TRC Characteristics and Clinical Bone Regeneration Outcomes

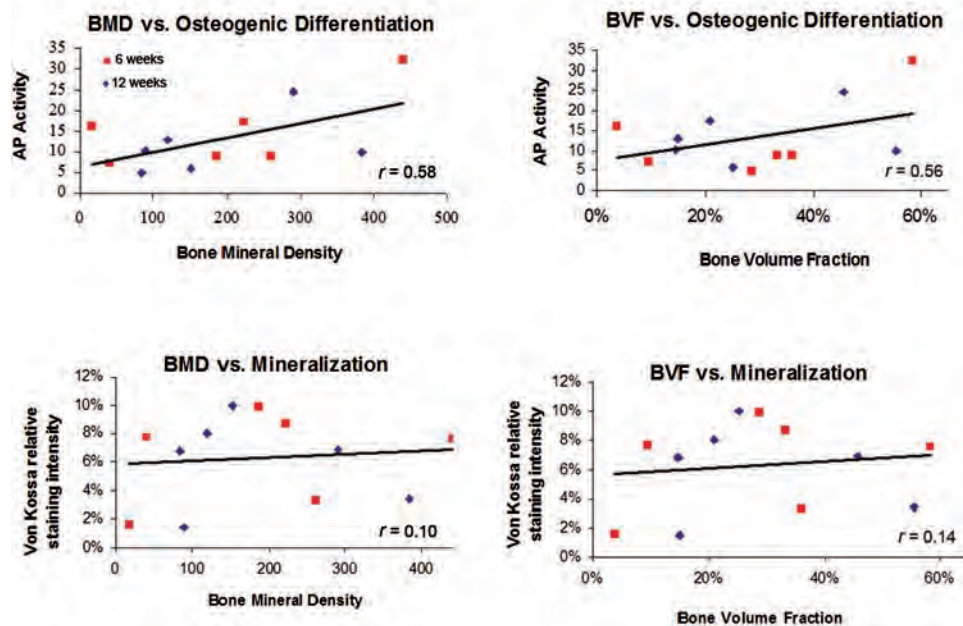


Figure 3. In vitro TRC characteristics and clinical regeneration outcomes. The in vitro osteogenic potential [alkaline phosphatase (AP)-fold induction, top] and extracellular matrix mineralization (von Kossa staining, bottom) of each TRC population was correlated with its clinical capacity to form bone in vivo [as measured by BMD (mg/cc) and BVF]. Statistically significant differences ($p<0.05$) were noted between BMD and osteogenic differentiation, while nonsignificant differences were found between mineralization and BMD/BVF.

BMD ($r=0.58$; $p=0.049$). Positive correlations with *in vitro* mineralization ability and BMD and BVF measures were not statistically significant (Fig. 3).

DISCUSSION

Regenerative medicine aims to use tissue engineering to restore damaged and lost tissue (16). In this report, we describe the first randomized, controlled, human trial employing stem cell therapy for the regeneration of craniofacial bone. TRCs were grafted into osseous defects of the jaw and biopsies harvested for analyses at 6 and 12 weeks. Reconstruction of these sites was completed with oral implant therapy and treatment sites were followed for 12 months postoperatively. Clinical and laboratory analyses of treatment sites demonstrated that the cell therapy accelerated the regenerative response as determined clinically, radiographically, and histologically. Further, there was a significantly reduced need for secondary bone grafting procedures in the group that originally received the cell therapy.

The extraction socket created following tooth removal serves as a reasonable model of bone repair being that the resulting defect is reproducible and has a limited capacity to heal completely without intervention. Pelegrine and colleagues used this model recently to investigate the potential of a bone marrow graft in preserving alveolar bone following tooth removal (26). Upon evaluation of the grafted sites at 6 months, the graft provided better results in maintaining the alveolar bone relative to when no graft was used. Though the results suggested that bone marrow constituents provided benefit, the cellular component of the graft was not characterized, and thus, homogeneity of the graft from patient to patient could not be ascertained. Other promising preliminary reports of successful craniofacial regenerative procedures using bone marrow-derived grafts are similarly confounded by the lack of characterization of the grafted biological cell type or construct (8,20,31). Meijer and colleagues spoke to this limitation in a study evaluating the use of bone marrow grafts for craniofacial reconstructions (21). These treatments resulted in clinical bone formation in only three of the six patients treated and because the constituents of the grafts were not characterized, the authors indicated that the cause for the 50% failure rate could not be definitively determined.

Another general critique of cell therapy approaches has been the lack of reproducible cell isolation and expansion protocols that can predictably yield consistent cell populations. Two defining elements of our study relative to other case reports employing bone marrow grafts for craniofacial reconstructions are (1) characterization of the cell population prior to grafting and (2) early 6-week regenerative healing time evaluated. Through the cell processing protocol used to generate TRCs, within a given

range, cell surface marker characterization has demonstrated a relative degree of homogeneity in the TRCs produced between patients (1,10,13), namely enrichment of CD90⁺ cells. Preclinical studies of TRCs have demonstrated that high concentrations of CD90⁺ cells within TRC populations are positively correlated with ectopic bone formation (7). Even further, in correlating the *in vitro* osteogenic capacity of TRCs (AP) with the clinical regenerative BMD and BVF measures, we observed positive correlations (Fig. 3). These data provide important preliminary evidence underscoring the potential for targeted, individualized stem cell therapy approaches based upon initial cell characterization. Though the initial evidence appears promising, it is realized that *in vitro* analyses and clinical correlation studies need to be performed on larger subsets of TRC populations to more fully elucidate these correlations.

Another defining element of our study is the early 6-week time point in which we chose to reenter the regenerated sites. Most clinical protocols that employ grafting procedures for reconstruction of alveolar bone allow healing periods minimally of 3–6 months (5). In the natural healing environment of an extraction socket wound, the rate limiting step in the healing process is the recruitment and proliferation of progenitor cells from the local microenvironment (4,32). The rationale for our choosing the 6-week time point was to determine if wound repair could be accelerated by delivering cells to the defect at the time of tooth extraction. It was thus rather striking to see that TRC regenerated bone at 6 weeks similar to that observed at 12 weeks in both TRC and GBR groups. Furthermore, data shown in Table 3 and Figure 2 clearly demonstrate the ability of TRCs to augment bone regeneration of the healing socket by greatly reducing the need and extent of secondary grafting often performed at the time of oral implant installation. Additional studies would need to be performed to determine the mechanism of this accelerated regenerative response, yet two possible mechanisms for these observations exist: (1) the regenerated tissue is derived from the transplanted cells (12) and (2) the transplanted cells act in a trophic fashion and provide signals to the host cells thereby “jump-starting” the regenerative process (3).

The alveolar ridge defect model following tooth extraction is best viewed as a proof-of-concept approach using autologous cell therapy for the regeneration of craniofacial bone. Though our study was originally designed as a phase I/II first-in-humans trial to investigate safety, we included a control group (GBR) to which we could draw preliminary conclusions regarding efficacy. As such, the study is considered to be small, and though the early findings are promising, they are also considered with caution in the context of this proof-of-concept investigation. A next step would be to evaluate this approach in a

larger patient population, which could lead to a strong foundation for utilization of this approach for treatment of larger, more debilitating craniofacial conditions.

ACKNOWLEDGMENTS: *This study was funded by a Career Award for Medical Scientists from the Burroughs Wellcome Fund (D.K.), the National Institutes of Health NIH/NCRR UL1RR024986 (W.V.G.), and National Institutes of Health NIH/NIDCR DE13397 (W.V.G.). The authors would like to thank Dr. Andrew Eisenberg for performing the bone marrow aspirations. The authors would also like to thank Judy Douville, Lea Franco, Anna Galloro, Emily Hall, Christina Huffman, and Emily Thorpe for administrative and clinical support. D.K. and W.V.G. were responsible for the concept and design of the study and obtained funding. D.K., G.P., C.H.P., and S.A.T. were responsible for acquisition of data. T.B. and D.K. did the statistical analysis. D.K. and W.V.G. supervised the study. R.L.B. provided administrative, material and technical support. D.K., W.V.G., G.P., and T.B. participated in the interpretation of data and critical revision of the report for intellectual content. All authors provided final approval of the submitted version. Ronnda L. Bartel is an employee of Aastrom Biosciences.*

REFERENCES

- Boiret, N.; Rapatel, C.; Boisgard, S.; Charrier, S.; Tchirkov, A.; Bresson, C.; Camilleri, L.; Berger, J.; Guillouard, L.; Guerin, J. J. CD34⁺ CDw90 (Thy-1)⁺ subset colocalized with mesenchymal progenitors in human normal bone marrow hematoma units is enriched in colony-forming unit megakaryocytes and long-term culture-initiating cells. *Exp. Hematol.* 31(12):1275–1283; 2003.
- Caldwell, J.; Palsson, B. O.; Locey, B.; Emerson, S. G. Culture perfusion schedules influence the metabolic activity and granulocyte-macrophage colony-stimulating factor production rates of human bone marrow stromal cells. *J. Cell. Physiol.* 147(2):344–353; 1991.
- Caplan, A. I. Adult mesenchymal stem cells for tissue engineering versus regenerative medicine. *J. Cell. Physiol.* 213(2):341–347; 2007.
- Cardaropoli, G.; Araujo, M.; Hayacibara, R.; Sukekava, F.; Lindhe, J. Healing of extraction sockets and surgically produced—augmented and non-augmented—defects in the alveolar ridge. An experimental study in the dog. *J. Clin. Periodontol.* 32(5):435–440; 2005.
- Coulthard, P.; Esposito, M.; Jokstad, A.; Worthington, H. V. Interventions for replacing missing teeth: Bone augmentation techniques for dental implant treatment. *Cochrane Database Syst. Rev.* 2003(3):CD003607; 2003.
- Delaere, P.; Vranckx, J.; Verleden, G.; De Leyn, P.; Van Raemdonck, D. Tracheal allotransplantation after withdrawal of immunosuppressive therapy. *N. Engl. J. Med.* 362(2):138–145; 2010.
- Dennis, J. E.; Esterly, K.; Awadallah, A.; Parrish, C. R.; Poynter, G. M.; Goltry, K. L. Clinical-scale expansion of a mixed population of bone-marrow-derived stem and progenitor cells for potential use in bone-tissue regeneration. *Stem Cells* 25(10):2575–2582; 2007.
- Filho Cerruti, H.; Kerkis, I.; Kerkis, A.; Tatsui, N. H.; da Costa Neves, A.; Bueno, D. F.; da Silva, M. C. Allogeneous bone grafts improved by bone marrow stem cells and platelet growth factors: Clinical case reports. *Artif. Organs* 31(4):268–273; 2007.
- Gao, J.; Dennis, J. E.; Solchaga, L. A.; Awadallah, A. S.; Goldberg, V. M.; Caplan, A. I. Tissue-engineered fabrication of an osteochondral composite graft using rat bone marrow-derived mesenchymal stem cells. *Tissue Eng.* 7(4):363–371; 2001.
- Gastens, M. H.; Goltry, K.; Prohaska, W.; Tschöpe, D.; Stratmann, B.; Lammers, D.; Kirana, S.; Gotting, C.; Kleesiek, K. Good manufacturing practice-compliant expansion of marrow-derived stem and progenitor cells for cell therapy. *Cell Transplant.* 16(7):685–696; 2007.
- Holtorf, H. L.; Jansen, J. A.; Mikos, A. G. Ectopic bone formation in rat marrow stromal cell/titanium fiber mesh scaffold constructs: Effect of initial cell phenotype. *Biomaterials* 26(31):6208–6216; 2005.
- Jensen, S. S.; Terheyden, H. Bone augmentation procedures in localized defects in the alveolar ridge: Clinical results with different bone grafts and bone-substitute materials. *Int. J. Oral Maxillofac. Implants* 24 Suppl:218–236; 2009.
- Kaigler, D.; Avila, G.; Wisner-Lynch, L.; Nevins, M. L.; Nevins, M.; Rasperini, G.; Lynch, S. E.; Giannobile, W. V. Platelet-derived growth factor applications in periodontal and peri-implant bone regeneration. *Expert Opin. Biol. Ther.* 11(3):375–385; 2011.
- Kaigler, D.; Krebsbach, P. H.; Wang, Z.; West, E. R.; Horger, K.; Mooney, D. J. Transplanted endothelial cells enhance orthotopic bone regeneration. *J. Dent. Res.* 85(7):633–637; 2006.
- Krebsbach, P. H.; Kuznetsov, S. A.; Satomura, K.; Emmons, R. V.; Rowe, D. W.; Robey, P. G. Bone formation in vivo: Comparison of osteogenesis by transplanted mouse and human marrow stromal fibroblasts. *Transplantation* 63(8):1059–1069; 1997.
- Langer, R.; Vacanti, J. P. Tissue engineering. *Science* 260(5110):920–926; 1993.
- Lee, C. H.; Shah, B.; Muioli, E. K.; Mao, J. J. CTGF directs fibroblast differentiation from human mesenchymal stem/stromal cells and defines connective tissue healing in a rodent injury model. *J. Clin. Invest.* 120(9):3340–3349; 2010.
- Macchiarini, P.; Jungebluth, P.; Go, T.; Asnaghi, M. A.; Rees, L. E.; Cogan, T. A.; Dodson, A.; Martorell, J.; Bellini, S.; Parnigotto, P. P.; Dickinson, S. C.; Hollander, A. P.; Mantero, S.; Conconi, M. T.; Birchall, M. A. Clinical transplantation of a tissue-engineered airway. *Lancet* 372(9655):2023–2030; 2008.
- Manolagas, S. C.; Burton, D. W.; Deftos, L. J. 1,25-Dihydroxyvitamin D₃ stimulates the alkaline phosphatase activity of osteoblast-like cells. *J. Biol. Chem.* 256(14):7115–7117; 1981.
- Marcacci, M.; Kon, E.; Moukhachev, V.; Lavroukov, A.; Kutepov, S.; Quarto, R.; Mastrogiacomo, M.; Cancedda, R. Stem cells associated with macroporous bioceramics for long bone repair: 6- to 7-year outcome of a pilot clinical study. *Tissue Eng.* 13(5):947–955; 2007.
- Meijer, G. J.; de Bruijn, J. D.; Koole, R.; van Blitterswijk, C. A. Cell based bone tissue engineering in jaw defects. *Biomaterials* 29(21):3053–3061; 2008.
- Melcher, A. H. On the repair potential of periodontal tissues. *J. Periodontol.* 47(5):256–260; 1976.
- Misch, C. E. Bone classification, training keys to implant success. *Dent. Today* 8(4):39–44; 1989.
- Mossey, P. A.; Little, J.; Munger, R. G.; Dixon, M. J.; Shaw, W. C. Cleft lip and palate. *Lancet* 374(9703):1773–1785; 2009.
- Park, C. H.; Abramson, Z. R.; Taba, Jr., M.; Jin, Q.; Chang, J.; Kreider, J. M.; Goldstein, S. A.; Giannobile, W. V. Three-dimensional micro-computed tomographic imaging

- of alveolar bone in experimental bone loss or repair. *J. Periodontol.* 78(2):273–281; 2007.
26. Pelegri, A. A.; da Costa, C. E.; Correa, M. E.; Marques, Jr., J. F. Clinical and histomorphometric evaluation of extraction sockets treated with an autologous bone marrow graft. *Clin. Oral Implants Res.* 21(5):535–542; 2010.
 27. Pihlstrom, B. L.; Michalowicz, B. S.; Johnson, N. W. Periodontal diseases. *Lancet* 366(9499):1809–1820; 2005.
 28. Quarto, R.; Mastrogiacomo, M.; Cancedda, R.; Kutepov, S. M.; Mukhachev, V.; Lavroukov, A.; Kon, E.; Marcacci, M. Repair of large bone defects with the use of autologous bone marrow stromal cells. *N. Engl. J. Med.* 344(5):385–386; 2001.
 29. Rayment, E. A.; Williams, D. J. Concise review: Mind the gap: Challenges in characterizing and quantifying cell- and tissue-based therapies for clinical translation. *Stem Cells* 28(5):996–1004; 2010.
 30. Schwartz, R. M.; Palsson, B. O.; Emerson, S. G. Rapid medium perfusion rate significantly increases the productivity and longevity of human bone marrow cultures. *Proc. Natl. Acad. Sci. USA* 88(15):6760–6764; 1991.
 31. Soltan, M.; Smiler, D.; Soltan, C.; Prasad, H. S.; Rohrer, M. D. Bone grafting by means of a tunnel dissection: Predictable results using stem cells and matrix. *Implant Dent.* 19(4):280–287; 2010.
 32. Trombelli, L.; Farina, R.; Marzola, A.; Bozzi, L.; Liljenberg, B.; Lindhe, J. Modeling and remodeling of human extraction sockets. *J. Clin. Periodontol.* 35(7):630–639; 2008.